Electromagnetic Coupling in Chiral and Nonlinear Metamaterials

Kirsty Hannam

A thesis submitted for the degree of
Doctor of Philosophy
The Australian National University

October, 2014

Declaration

This thesis is an account of research undertaken between March 2010 and April 2014 at The Nonlinear Physics Centre, Research School of Physical Sciences and Engineering at the Australian National University, Australia.

The research presented in this thesis was conducted under the supervision of Dr. David Powell, Dr. Ilya Shadrivov and Prof. Yuri Kivshar, but unless otherwise stated, is my own work. Except where acknowledged in the customary manner, the material presented in this thesis is, to the best of my knowledge, original and has not been submitted in whole or part for a degree in any university.

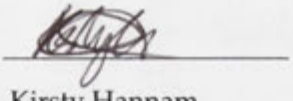

Kirsty Hannam

October, 2014

Publications

Journal papers

[1] D.A. Powell, **K. Hannam**, I.V. Shadrivov and Y.S. Kivshar. Near-field interaction of twisted split-ring resonators. *Phys. Rev. B.*, 83(23):235420, 2011.

[2] **K. Hannam**, D.A. Powell, I.V. Shadrivov and Y.S. Kivshar. Tuning the nonlinear response of coupled split-ring resonators. *Appl. Phys. Lett.*, 100(8):081111, 2012.

[3] **K. Hannam**, D.A. Powell, I.V. Shadrivov and Y.S. Kivshar. Dispersionless optical activity in metamaterials. *Appl. Phys. Lett.*, 102(20):201121, 2013.

[4] **K. Hannam**, D.A. Powell, I.V. Shadrivov and Y.S. Kivshar. Broadband chiral metamaterials with large optical activity. *Phys. Rev. B.*, 89(12):125105, 2014.

Conference presentations

[1] **K. Hannam**, D.A. Powell, I.V. Shadrivov and Y.S. Kivshar. (Contributed) Rotational tuning in metamaterials. *19th Congress of the Australian Institute of Physics*, Melbourne, Australia, 2010.

[2] **K. Hannam**, D.A. Powell, I.V. Shadrivov and Y.S. Kivshar. (Invited - upgraded) Tuning linear and nonlinear properties of split ring resonators. *The 8th Conference on Lasers and Electro-Optics Pacific Rim*, Sydney, Australia, 2011.

[3] **K. Hannam**, D.A. Powell, I.V. Shadrivov and Y.S. Kivshar. (Contributed) Tunable nonlinear response of coupled resonators. *Metamaterials 2011: The fifth International Congress on Advanced Electromagnetic Materials in Microwaves and Optics*, Barcelona, Spain, 2011.

[4] **K. Hannam**, D.A. Powell, I.V. Shadrivov and Y.S. Kivshar. (Contributed) Wideband optical activity in meta-atoms coupled to their complement. *Electrical, Transport and Optical Properties of Inhomogenous Media 9*, Marseille, France, 2012.

[5] **K. Hannam**, D.A. Powell, I.V. Shadrivov and Y.S. Kivshar. (Contributed) Near-dispersionless optical activity in meta-atoms. *20th Congress of the Australian Institute of Physics*, Sydney, Australia, 2012.

[6] **K. Hannam**, D.A. Powell, I.V. Shadrivov and Y.S. Kivshar. (Contributed) Dispersionless optical activity in chiral meta-atoms. *Australia and New Zealand Congress on Optics and Photonics*, Freemantle, Australia, 2013.

Acknowledgments

This thesis would not have been possible without the aid of numerous people. In particular, I would like to thank my supervisory panel, consisting of Dr. David Powell, Dr. Ilya Shadrivov and Prof. Yuri Kivshar, for overseeing my candidature and putting up with me over the last four years. Also for all the time spent helping me develop my ideas and giving feedback on my results and drafts for everything. David also spent a lot of time proof reading this thesis though grants were due. Ilya was very helpful by making figures and helping me with other figures.

Dr. David Powell also provided the calculations in Chapter 2, which complemented the experiments I had done. I would also like to thank the other members who were helpful in discussions, such as Dr. Mikhail Lapine and Dr. Andrey Miroshnichenko, along with everyone in the Nonlinear Physics Department for attending my practice presentations and giving feedback.

Thank you to the technical staff in the workshops for helping with fabrication and resources. I also acknowledge the Australian National University for funding me via scholarships during this degree, and the Australian Research Council, for providing the grant money which supported my research, along with the opportunity to travel for conferences and workshops.

I would like to thank the other students in the Nonlinear Physics Centre, who often provided much needed friendship, laughter and distraction, along with helpful, thought provoking discussions. In particular my office mate Yue for the friendship, encouragement and laughs over the years.

I would like to thank my friends and family for putting up with my times of stress and being antisocial over the last few years, and continuing to encourage me. I thank my parents, who have always encouraged me to follow my own path, been willing to support me financially when needed over the years, and for being understanding of me not being able to visit often. I am also thankful for my boyfriend Sam who has been very

supportive and calms me down when the stress starts getting the better of me. He has also put in a lot of time and effort helping me with making diagrams and proofreading for this thesis.

To everyone who contributed in some way to my progress over the last four years, thank you.

Abstract

This thesis is a study of the mechanisms and applications of the near-field interaction in metamaterial systems, investigated using pairs of resonators. Metamaterials are arrays of sub-wavelength resonant elements, and can be engineered to create exotic properties such as artificial magnetism and negative refraction. The response of a bulk metamaterial is strongly dependent on the lattice parameters, and the relative orientation of neighboring resonators has a particularly strong influence, due to the near-field interaction.

To start with I study the coupling between two split ring resonators rotated through their common axis, in order to further understand the near-field interaction. The interplay between the electric and magnetic interactions in the system is analyzed, along with the resulting crossing of the resonant modes. A Lagrangian model is applied to the twisted rings to determine the mechanisms behind the crossing of the modes, which is dependent on the symmetry and losses in the system.

The ability to use the near-field interaction to control the nonlinear tuning is then investigated. By introducing nonlinear inclusions in resonant elements, meta-atoms with a dynamic nonlinear response can be created. By modifying the spacing between such resonators, I can control this response via the near-field interaction. The resulting nonlinear response can be explained using the linear properties of the system such as the absorption in the resonators, and the voltage induced across the nonlinear inclusions.

The possibility of manipulating chiral properties of twisted meta-atoms is also studied, in order to address the issue of resonant optical activity over the transmission band, along with the accompanying ellipticity in the output polarization. In particular, I propose a "mixed pair" - a structure consisting of a meta-atom and its complement. Combining these elements together couples equivalent parallel electric and magnetic dipoles. This structure has a lower order symmetry than a pair of twisted identical resonators. The optical activity in the structure is optimized through manipulating the coupling in the structure. I also develop a method for retrieving the effective param-

eters, and present the results retrieved from a periodic array. The resulting retrieved parameters are verified by recalculating the scattering parameters theoretically.

Contents

List of Figures

Chapter 1

Introduction

1.1 Metamaterials

When developing new technologies for applications such as sensing, medical imaging and antennas, it is important to have structures which are highly tunable and flexible in their response. There are limits to what can be achieved using materials found in nature, so to meet more demanding applications artificial materials are engineered to have specific properties. This idea has been explored using plasmas [1], photonic crystals [2], liquid crystals [3], along with many other approaches.

Utilizing metamaterials provides freedom in creating structures with unique properties. A metamaterial is an engineered array of artificial structures, distinguishable from photonic crystals in that they have periodicity significantly smaller than the wavelength. This is demonstrated in Fig. 1.1, where the density of the unit cells is compared for photonic crystals and metamaterials. The high relative density in metamaterials

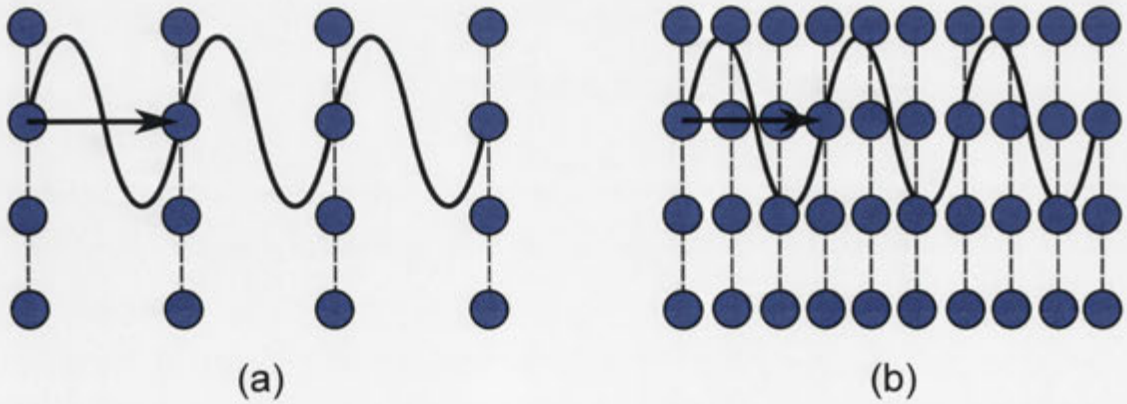

Figure 1.1: Conceptual schematic showing the wavelength with respect to the material density for (a) photonic crystals, where the wavelength is comparable to the period of the structure, and (b) metamaterials, where the wavelength is much larger than the period of the structure.

means that the incoming wave cannot resolve the details of the structure. This enables the metamaterial to be assigned effective parameters, such as the magnetic permeability μ, the electric permittivity ϵ, and the refractive index n. Metamaterials can then be engineered with exotic properties such as artificial magnetism [4], negative refractive index [5], strong nonlinearity [6] and chirality [7], as well as being used for applications such as electromagnetic cloaking [8]. Many applications do not need bulk materials, and a single element or layer may suffice.The individual elements making up these arrays can be referred to as "meta-atoms" and the single layers as "meta-surfaces" or "meta-films". In the case of isotropic media, the material parameters relate the external fields of a homogeneous structure with the constitutive equations

$$\begin{pmatrix} \mathbf{D} \\ \mathbf{B} \end{pmatrix} = \begin{pmatrix} \epsilon_0\epsilon & 0 \\ 0 & \mu_0\mu \end{pmatrix} \cdot \begin{pmatrix} \mathbf{E} \\ \mathbf{H} \end{pmatrix}. \tag{1.1}$$

1.1.1 Artificial magnetism

Natural magnetism requires magnetic materials, and most magnetic materials can only respond at low frequencies (below the gigahertz range). Exceptions to this, such as ferrites, remain moderately active at gigahertz frequencies but are often heavy [4].

By building a material based on resonators a metamaterial can be created having an artificial magnetic response. The material can be designed to have strong magnetic properties, as well as being quite light, if so desired. Such materials can also be created using non-magnetic materials as the building blocks. As the effect will be resonant, it will only act within a narrow band of frequencies. These materials can also be made to operate at much higher frequencies, even up to optical frequencies.

A limited magnetic response can be achieved by exciting an array of metallic spheres or cylinders. To achieve a stronger magnetic resonance capacitive elements can be introduced into the design, balancing the inductive effect. This can be done by adding gaps to the internal structure of the cylinder resulting in a low frequency resonance [4].

Split-ring resonators

By using a structure with finite thickness, a more isotropic effect is produced. Such a structure is shown in Fig. 1.2 (a), and is known as a split-ring resonator (SRR). The

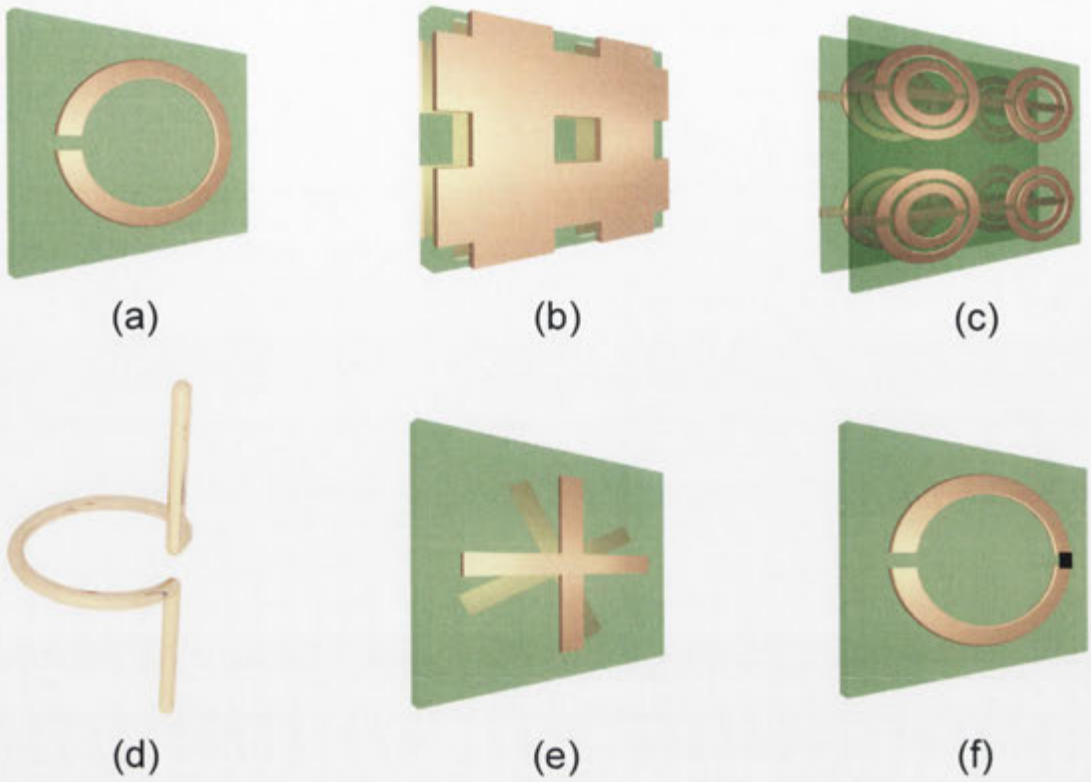

Figure 1.2: Examples of common resonators used to build metamaterials. (a) Split-ring resonator, (b) fishnet structure, (c) negative-index material, made from an array of combined SRRs and wires, (d) canonical spiral, (e) twisted crosses and (f) a nonlinear SRR with an attached diode.

use of the SRR for obtaining a magnetic response was originally proposed by Pendry et al. [4] in 1999 for use in the microwave regime. The external field incident on the SRR excites currents in the metal ring, leading to a current build up over the gap which results in a magnetic resonance. In order to drive the response further sub-wavelength, SRRs are often combined in pairs with a smaller ring encircled by a larger ring, shown in Fig. 1.2(c). The effective permeability for an array of such pairs is modeled geometrically using

$$\mu = 1 - \frac{\frac{\pi r^2}{a^2}}{1 + i\frac{2l\sigma_1}{\omega r \mu_0} - \frac{3lc_0^2}{\pi\omega^2 ln\left(\frac{2c}{d}\right)r^3}}. \tag{1.2}$$

The resistance per unit length of the wires measured around the circumference is represented as σ_1, c_0 is the speed of light in free space, a and l are the lattice parameters, and c, d and r the geometric parameters of the rings (the width of the rings, inner radius of the smaller ring, and gap between the rings respectively). The resulting effective permeability can become negative around the resonance.

SRRs have since been scaled down for use at terahertz and mid-infrared frequencies [9–11]. However at higher frequencies there is an increased scattering of electrons at the surface of the metal, along with kinetic inductance due to the finite inertia of the electrons, which breaks the linear scaling of frequency with radius and dampens the resonance [12, 13]. This results in the SRR being unable to exhibit a strong magnetic response for use at optical frequencies.

Structures for higher frequencies

Alternative structures are required to generate a magnetic response at higher frequencies. An array of gold staple-like structures was used to experimentally achieve negative permeability at mid-infrared frequencies [14]. Magnetic responses were later achieved at near-infrared frequencies using a composite structure consisting of two gold layers separated by a dielectric layer, all of which have an array of holes drilled through, on top of a glass substrate [15]. This structure came to be known as the fishnet structure and is shown in Fig. 1.2 (b). The design was later improved to support a magnetic response at optical frequencies [16]. This fishnet structure can also be used at terahertz and microwave frequencies [17].

There has also been a lot of interest in the use of nanoparticle resonators to achieve a magnetic response at optical frequencies. A metallic semi-sphere can be seen as a three dimensional analogue of a split-ring resonator, and can be used at optical frequencies to achieve a strong magnetic response [18]. Dielectric spherical nanoparticles also have a magnetic response at infrared [19] and optical [20] frequencies. It is also found at higher frequencies that use of dielectric materials instead of metals is often preferred due to reduced losses in the system [19]. Through a combination of a metallic split-ring with a silicon sphere at near-infrared frequencies, the ferrimagnetism of the response can be controlled, where changing the distance between the resonators can switch the system from being ferrimagnetic to antiferrimagnetic [21]. Cubic nanoparticles can also be used to create an isotropic magnetic response in three dimensions [22].

1.1.2 Negative refraction

The effects of a wave propagating through a medium with both negative permeability and negative permittivity were theoretically investigated by Veselago in 1968 [23]. He

found that if the structure has both negative ϵ and μ the resulting refractive index of the structure, defined as

$$n = \pm\sqrt{\mu\epsilon}, \tag{1.3}$$

will take the negative sign. This means that the wave is traveling backwards, where the direction of the wave vector is now directed opposite to the Poynting vector, shown in Fig. 1.3 (b). This also results in a reversal of the Doppler effect. Such materials were originally known as Left-handed materials (LHM), however this is similar to another common term in the metamaterials field, so instead the term Negative-index materials (NIMs) is used. NIMs can be used in applications such as super-lensing and super-resolution [23,24]

However, materials with desirable negative properties are not easy to come by. Initially Veselago was thinking of using plasma to achieve a negative permittivity, but it is now known that an array of thin wires will have the same property [25,26]. It was not until the proposal of the SRR [4] however, that a negative permeability could be easily achieved. By combining SRR and wires in an array, as in Fig. 1.2 (c), and designing the resonators so that their resonances overlap, a band with simultaneously negative μ and ϵ was achieved experimentally [5,27]. This was confirmed to result in a negative refractive index [28,29]. This effect can also be achieved by exciting SRRs in a metallic waveguide operating below the first cut-off mode, as this is equivalent to a medium with $\epsilon < 0$ [30]. Efforts have also been made towards creating such materials in two and three dimensions [31,32]. A lot of research has since gone into expanding the possibilities of achieving negative refraction, especially at higher frequencies [16,33]. A negative refractive index has also been achieved using photonic crystals [34], however as this structure is not sub-wavelength the response cannot be homogenized.

1.1.3 Material symmetries

In the most general case, the effective medium description of a metamaterial has not only electric and magnetic terms, but also terms representing the coupling between them. The material parameters in a general material combine the electric and magnetic

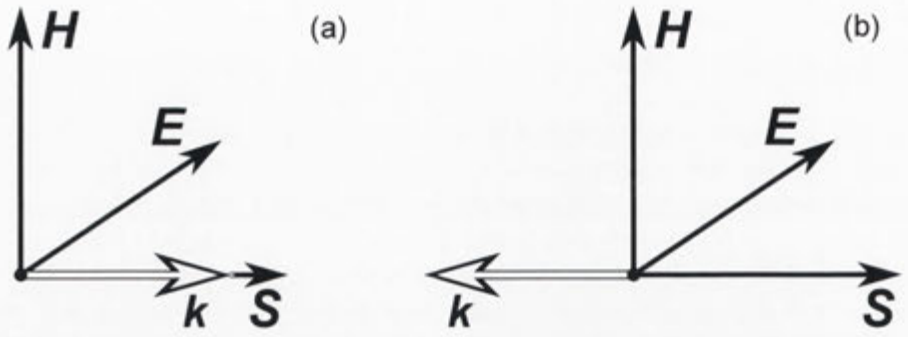

Figure 1.3: Wave vectors in (a) positive-index and (b) negative-index materials, showing the change in direction of the wave vector k. E is directed into the page.

fields. This is expressed in the general form [35]

$$\begin{pmatrix} \mathbf{D} \\ \mathbf{B} \end{pmatrix} = \begin{pmatrix} \epsilon_0 \bar{\bar{\epsilon}} & \left(\bar{\bar{\chi}} - i\bar{\bar{\kappa}}\right)/c \\ \left(\bar{\bar{\chi}} + i\bar{\bar{\kappa}}\right)^T/c & \mu_0 \bar{\bar{\mu}} \end{pmatrix} \cdot \begin{pmatrix} \mathbf{E} \\ \mathbf{H} \end{pmatrix}, \tag{1.4}$$

where $\bar{\bar{\epsilon}}$ and $\bar{\bar{\mu}}$ are the material tensors describing the dielectric and magnetic responses, $\bar{\bar{\kappa}}$ is the bi-anisotropy tensor, which describes the cross-coupling between the incident fields, and $\bar{\bar{\chi}}$ is known as the non-reciprocity tensor. These two separate tensors ($\bar{\bar{\kappa}}$ and $\bar{\bar{\chi}}$) are used as they represent two distinct effects - reciprocal and non-reciprocal.

The most general medium is non-reciprocal, which results in the transmission being different in the forward and backward directions along the same axis. Reciprocity is only violated for special classes of media, such as nonlinear materials or biased ferrites. This response can be simplified depending on the symmetry properties of the material, with the most simplified case being the homogeneous, isotropic case, with no coupling between the electric and magnetic fields. This case is described by Eq. (1.1), using only two effective parameters, μ and ϵ, which are scalar. Only structures excited at normal incidence, parallel to an axis of symmetry, will be considered in this thesis.

Reciprocal bi-anisotropic media

A bi-anisotropic medium is inhomogeneous and asymmetric. Specifically, it will be physically different when viewed from opposite directions, resulting in the reflection being dependent on the propagation direction. The constitutive equations for the recip-

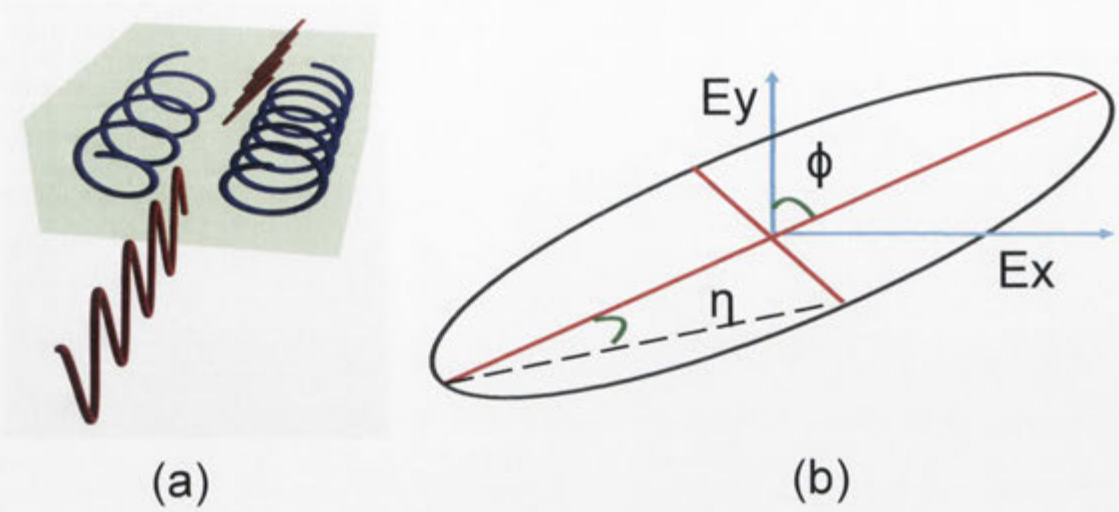

Figure 1.4: (a) A diagram of the effect of the electromagnetic waves passing through a chiral medium, where the linearly polarized wave is rotated through an angle as it passes through the material, which is the optical activity. (b) A diagram showing the output polarization of the wave. ϕ is the resulting optical activity, and η the ellipticity.

rocal case are

$$\begin{pmatrix} \mathbf{D} \\ \mathbf{B} \end{pmatrix} = \begin{pmatrix} \epsilon_0 \bar{\bar{\epsilon}} & -i\bar{\bar{\kappa}}/c \\ i\bar{\bar{\kappa}}^T/c & \mu_0 \bar{\bar{\mu}} \end{pmatrix} \cdot \begin{pmatrix} \mathbf{E} \\ \mathbf{H} \end{pmatrix}. \tag{1.5}$$

In the reciprocal case there is still coupling between the electric and magnetic fields, however the transmission is no longer dependent on the direction of the incoming wave. The bi-anisotropy can be caused by effects such as the magnetic resonance of a SRR coupling to the incident electric field, dependent upon the correct alignment of the fields relative to the SRR [36].

Chirality

Chirality leads to a special case of bi-anisotropy, where the trace of the bi-anisotropic tensor is non-zero. A chiral structure is distinct from its mirror image, an example of which is shown in Fig. 1.2 (c). Such a structure cannot be mapped onto its mirror image through any combination of translation and rotation operations.

A linearly polarized wave can be represented as a superposition of two identical but opposite circularly polarized waves. In an isotropic chiral medium, the two circular polarizations (right- and left- handed) are the propagating eigenmodes, and the chiral symmetry breaks the degeneracy causing the two polarizations to propagate at differ-

ent velocities. This results in the output polarization being rotated through an angle, which is the optical activity, shown in Fig. 1.4 (a). The output polarization can also have some ellipticity, which means it is no longer linearly polarized, and this is shown in Fig. 1.4 (b). Chiral metamaterials can have optical activity that is up to one million times stronger than that in natural materials, and may be useful for applications such as chemical sensing [37] and polarization manipulation.

A chiral medium can be either left- or right-handed, depending on the circular polarization with which it most strongly interacts [38]. In Section 1.1.2 it was mentioned that negative index media are sometimes called left-handed materials. It is important to distinguish between left-handed chiral media and negative index media, as they are referring to different properties of the material.

In the case of an isotropic chiral medium, the cross-coupling between the magnetic and electric polarizations of the media becomes scalar [7], resulting in the simplification of Eq. (1.5) to

$$\begin{pmatrix} \mathbf{D} \\ \mathbf{B} \end{pmatrix} = \begin{pmatrix} \epsilon_0\epsilon & -i\kappa/c \\ i\kappa/c & \mu_0\mu \end{pmatrix} \cdot \begin{pmatrix} \mathbf{E} \\ \mathbf{H} \end{pmatrix}, \tag{1.6}$$

where κ is the chirality parameter, which couples the parallel components of the electric and magnetic fields together. This added parameter results in negative refraction being easier to engineer, as now

$$n_{\pm} = \sqrt{\mu\epsilon} \pm \kappa \tag{1.7}$$

which are the refractive indices corresponding to the two propagating circular polarizations [39, 40]. The positive sign corresponds to the left-handed circularly polarized wave, and the negative sign to the right-handed circular polarization. Providing that μ and ϵ are small enough compared to κ, at least one of the polarizations will experience negative refraction [39]. This has resulted in large efforts to achieve negative refraction through chirality [41–43].

The chirality parameter can be calculated from the transmission of the circularly polarized waves [40]:

$$\kappa = \frac{-i}{2k_0 d} \ln\left(\frac{|T^+|e^{i\psi_+}}{|T^-|e^{i\psi_-}}\right), \tag{1.8}$$

where $T^{\pm}$ are the transmission coefficients for the two polarizations, and $\psi_{\pm}$ are the corresponding phases. Eq. 1.8 can also be expressed as

$$\mathrm{Re}\,(\kappa) = \frac{\psi_+ - \psi_- + 2m\pi}{2k_0 d}; \qquad \mathrm{Im}\,(\kappa) = \frac{\ln|T^-| - \ln|T^+|}{2k_0 d}, \tag{1.9}$$

with m being an integer determined by the condition $-\pi < \psi_+ - \psi_- + 2m\pi < \pi$ for one unit cell. The optical activity can be found using

$$\phi = \frac{\psi_+ - \psi_- + 2m\pi}{2}, \tag{1.10}$$

and the ellipticity using

$$\eta = \frac{1}{2}\tan^{-1}\frac{|T^+|^2 - |T^-|^2}{|T^+|^2 + |T^-|^2}. \tag{1.11}$$

It can be seen that the ellipticity (Eq. 1.11) and optical activity (Eq. 1.10) relate to the real and imaginary components of the chirality (Eq. 1.9).

This cross-coupling can be best seen in three-dimensional structures, such as the helix, or the canonical spiral shown in Fig. 1.2 (d), which can result in coupled magnetic and electric dipole type responses [44]. This is due to the magnetic field exciting both electric and magnetic dipoles, as well as the electric field exciting both electric and magnetic dipoles. Such structures are used extensively for applications requiring chirality, such as broadband polarizers [38, 45]. However, full three-dimensional structures can be quite complex to fabricate, especially at higher frequencies.

Alternatively, by combining two or more achiral, planar elements rotated about their common axis, such as crosses [46] or split ring resonators [47], a chiral meta-atom can be created. Such configurations have been shown to exhibit strong optical activity, and broadband polarization conversion [46–49]. An example is shown in Fig. 1.2 (e).

Depending on the resonant mode, the response of these structures is dominated by their electric or magnetic dipole moment. In either case, this results in strong reflection at the resonant frequency due to impedance mismatch of the sample with the surrounding medium. In addition, the resonant optical activity in such structures is accompanied by strong circular dichroism, causing ellipticity in the output polarization state, which is often undesirable [46]. This is due to the Kramers-Kronig relationship for κ [50]. In conducting a thorough search of the relevant literature [46–49, 51–56], it is found that

for all cases involving layered structures this dispersive optical activity occurs. It is possible to achieve reasonably flat optical activity off-resonance [46], however this was accompanied by a decrease in the magnitude of the optical activity. This requires the development of a planar metamaterial which produces strong, non-resonant optical activity over the transmission band.

1.1.4 Nonlinearity

So far the responses of metamaterials determined by the geometries of the individual meta-atoms have been discussed. However, introducing nonlinearity adds a whole realm of possibilities for engineering unique effects. The response of linear metamaterials is independent from the strength of the external field, whereas nonlinear materials can have responses which are power dependent. This has applications in tuning the frequency of negative refraction, as this is a narrow-band effect [57]. There is also the possibility of reproducing at microwave frequencies nonlinear effects commonly occurring at optical frequencies [6] such as second and third harmonic generation [58–61], and the nonlinear Kerr effect [62].

A nonlinear meta-atom can be created by including some form of nonlinear element, such as a semiconductor diode, in a resonator. By attaching a semiconductor component across a split-ring resonator and changing the doping level, the resulting resonance can be modulated [63]. More commonly, by adding a varactor to a slit on a SRR, as shown in Fig. 1.2 (f), and applying a bias voltage, the resonance can be tuned through the resulting change in capacitance [57]. Such a response can be used for the design of tunable notch filters [64].

Many tunable inclusions also respond to the high frequency incident wave, which results in meta-atoms with varactors attached potentially having a dynamic nonlinear response [6]. These systems will typically have power-dependent resonant frequencies [57, 65–67]. The nonlinear response of metamaterials can be much stronger than that of natural materials, due to their resonant nature and the local field enhancement which occurs at certain "hot spots". This has been utilized to create metamaterials at microwave frequencies to achieve wave mixing [68], three-wave coupling [69] and control of the second harmonic generation [61], among other effects [70].

1.2 Coupling and hybridization of meta-atoms

1.2.1 Effective medium theory

The response of a bulk metamaterial is dependent on the properties of the individual elements, and can be modeled using effective medium theory, which averages the electric and magnetic responses over the unit cells of the metamaterial. This is used to calculate the effective parameters from the transmission and reflection [71]. The resulting response is dependent on the properties of the resonator - size, shape and dielectric function, as well as on the properties of the surrounding medium [72]. Changing the physical structure of SRRs, including the introduction of asymmetries, can modify the response substantially [11].

The overall response of the lattice is determined not just by the geometrical properties of the individual resonators, but also on the interactions of the resonators [73]. The following equation was developed by Gorkunov et al. to calculate the overall response of a bulk metamaterial made of resonant circular conducting elements:

$$\mu = \frac{\frac{iZ}{\omega\mu_0 r_0} + \Sigma - \frac{2}{3}\pi^2 r_0^3 n_0}{\frac{iZ}{\omega\mu_0 r_0} + \Sigma - \frac{1}{3}\pi^2 r_0^3 n_0}, \tag{1.12}$$

where r_0 is the radius of the loop, n_0 is the volume concentration of the loop, Z is the self-impedance and $\Sigma = \sum_{n' \neq n} J(\mathbf{r}_n - \mathbf{r}_{n'})$ is a dimensionless parameter which depends only on the lattice type and the lattice constant values. Here $J(\mathbf{r})$ is a dimensionless function describing the mutual inductance around the loops, and $\mathbf{r}_n$ is the radius vector. It can be seen from this equation that the overall response of the metamaterial is dependent on both the individual parameters and on the lattice parameters.

A lot of research has been done to determine the ideal spacing of resonators to ensure homogeneity of the response [74]. The parameters of a metamaterial should not be dependent on the thickness of the metamaterial, however if the resonators are too close, the coupling is too strong, and the resulting properties change with every layer added, including the chiral properties [53].

This coupling provides a whole new range of tunable metamaterials with unique properties [77]. These can also be created using MEMS devices, and have a range of ap-

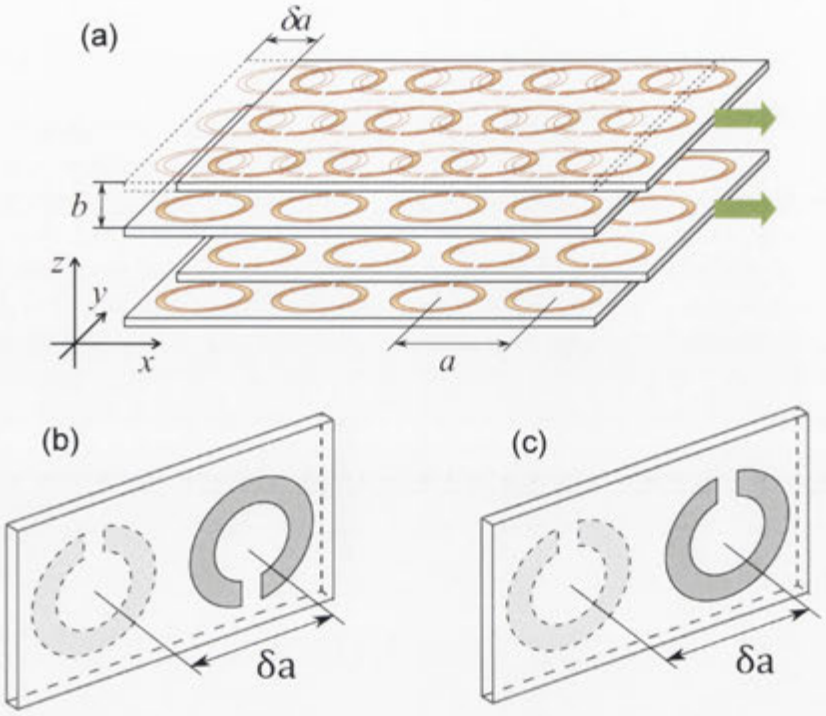

Figure 1.5: (a) Example of a metamaterial array of split ring resonators tuned by shifting alternating layers [75]. Two split-rings in a (b) broadside- and (c) gap-to-gap-coupled configuration [76]. δa is the lateral shift between layers, defined for (b) and (c) as the lateral distance between the centers of the two rings.

plications, such as making tunable filters. Many methods and applications are explored further in Ref. [78]. In particular, in Ref. [75], Lapine et al. showed experimentally that by shifting alternate layers of a bulk structure, as shown in Fig. 1.5 (a), they could effectively tune the overall response in a way that minimized altering the geometry.

As meta-atoms are not strongly sub-wavelength, coupling between them results in a highly non-local response which is not well described by effective medium theory. A new model for describing the materials is needed. The work by Gorkunov et al. [73] takes into account the mutual interaction of all the elements in the lattice. A modified effective medium approach based on circuit theory was also used in [75]. However these models only use very approximate expressions to describe the interaction. They are also only relevant to bulk systems but many systems of interest have a small number of elements, such as meta-surfaces or pairs of resonators.

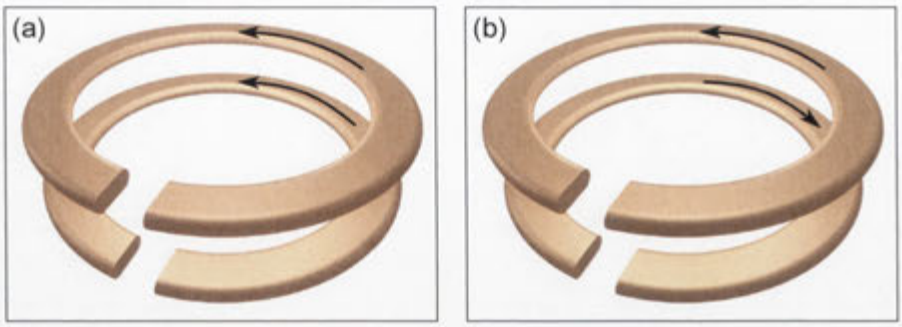

Figure 1.6: Relative current flow directions for the (a) symmetric and (b) antisymmetric modes.

1.2.2 Exact microscopic description of near-field interaction

When two resonators are close enough together, they will couple, resulting in a change in the resonant behavior [79]. When the coupling is weak, the response can be described using coupled mode theory [80]. Some commonly used resonator pairs are edge-coupled and broadside-coupled SRRs, the latter of which can be seen in Fig. 1.5 (b) [76,81]. This coupling results in a hybridization and splitting of the resonant modes. In the case of identical resonators, there will be a symmetric and an antisymmetric mode [82]. The modes are named according to the relative direction of the currents - the currents flow in the same direction for the symmetric mode, shown in Fig. 1.6 (a), and in opposite directions for the antisymmetric mode, shown in Fig. 1.6 (b).

The effect of the relative orientation of neighboring resonators was studied in Ref. [76] by comparing a pair of SRRs broadside-coupled, shown in Fig. 1.5 (b), to a pair of SRRs coupled gap-to-gap, shown in Fig. 1.5 (c). It was found that the orientation of meta-atoms within the lattice has a strong influence on the resulting lattice response, and this contradicts earlier simplified models describing the interaction of the rings using mutual inductance. The dependence on the orientation within the lattice is due to near-field coupling between elements, which is strongest between nearest neighbors. Understanding this interaction is vital to being able to correctly understand and model the tuning and coupling mechanisms in the overall structure, and this will be the main topic of this thesis.

To this end H. Liu et al. developed a Lagrangian model to numerically analyze an array consisting of pairs of split ring resonators on the same axis, with a relative rotation of 90° in Ref. [79]. The hybridized modes of this system showed strong polarization rotation, and had suppressed radiation losses [83]. Subsequently, N. Liu et al. [84] inves-

tigated a similar system, but with the rotation changing from 0° through to 90°. They used numerical analysis to extract the eigenmodes of a pair of SRRs operating in the near infrared, and fitted a dipole model to the generalized dispersion curve. In particular, it was assumed that the magnetic interaction constant is invariant with twist angle, however this is inconsistent with the strong variation of current density around the circumference of the ring. This model has since been extended to include the polarization rotation of the scattered radiation [85].

In Ref. [76], Powell et al. developed an approach for determining the exact electric and magnetic interaction coefficients for the system. These coefficients were calculated based on the current and charge distributions calculated for the individual rings. The response for the pairs was then compared to the response of a bulk metamaterial with alternate layers shifted laterally. It was found that while the resonant frequencies were quantitatively different between a pair and an array, the effects of tuning were qualitatively similar. This suggests that the near-field interaction between neighboring elements is the dominant source of coupling in the array for a realistic arrangement of resonators, and so studying pairs of resonators to further understand this interaction is important. Calculating the interaction directly from the charges and currents gives a physical understanding of the system, and is valid in regimes where simpler models based on dipole-dipole interactions break down.

The near-field interaction is also essential for determining the overall response of chiral structures formed from achiral constituents, where the spacing between the resonators affects the chiral properties [49,51]. The coupling effects between multiple such chiral pairs combined as a longitudinal array have also been studied [53,54]. The near-field interaction provides a tool to address the issues discussed in Section 1.1.3, by allowing the engineering of a material with large, non-resonant optical activity.

So far most near-field interaction work has been focused on engineering the linear properties of metamaterials. As discussed in Section 1.1.4, nonlinear materials can have a response which is power dependent. Being able to engineer the nonlinear properties of a metamaterial would be a powerful tool in the design of metamaterials, and provide further degrees of freedom. The effect that the relative orientation of unaltered L-shaped resonators in an array has on the second-order nonlinear properties at optical frequen-

cies was studied in Ref. [86]. It was found that the response could be affected by up to a factor of fifty. However, the impact of near-field coupling effects on the nonlinear response of metamaterials has not been studied.

1.3 Thesis overview

In this Chapter I have given an overview of the development and theory of metamaterials, and the motivation behind my study of pairs of coupled resonators. This overview focused on the near-field interaction between resonators, and the effects this has on the overall properties of a bulk metamaterial. It also focused on the unique properties that metamaterials can have.

In Chapter 2, the coupling between two split ring resonators rotated through a twist angle θ is studied, in order to further understand the *near-field interaction*. In particular, I look at the interplay between the electric and magnetic interactions in the system, and the resulting crossing of the resonant modes. I use a Lagrangian model applied to the twisted rings to understand the crossing of the modes.

I then investigate the *control of nonlinear tuning* via the near-field interaction in Chapter 3. This is done by attaching varactors to the gaps in a pair of SRRs, and modifying the distance between them in the same way as in Ref. [76]. The nonlinear response is explained by looking at the linear properties of the system such as the voltage induced across the diodes.

In Chapter 4 the *chiral properties* of twisted meta-atoms are explored. In particular, I propose a "mixed pair", which is a structure consisting of a meta-atom and its complement. Combining these elements together couples equivalent parallel electric and magnetic dipoles, which should overcome the current issues with twisted chiral structures highlighted in Section 1.1.3. This structure has C_4 symmetry, which is a lower order than the symmetry in a pair of twisted crosses. I then optimize the optical activity in the structure through manipulating the coupling in the structure.

In Chapter 5 I continue to investigate the properties of the "mixed pair" proposed in the previous chapter, and study the effects of the symmetry of the structure on the properties. I develop a method for retrieving the effective parameters, as this has not been

previously done for metamaterials belonging to this symmetry group, and present the results retrieved from a periodic array. I verify the retrieved parameters by recalculating the scattering parameters theoretically.

Finally, I summarize my research in Chapter 6, and present an outlook of possible future directions for further studies.

Chapter 2

Near-field Interaction of Twisted Split Ring Resonators

The near-field interaction between resonators plays an important role in the response of metamaterials. As discussed in Section 1.2.2, this response causes the relative orientation of elements inside a lattice to significantly affect the results, as shown by Powell et al. in Ref. [70], where a pair of split-ring resonators shifted laterally was studied. It was found that the relative angle in between the two rings greatly influenced the resulting effect of shifting the rings. This interaction is strongest between neighboring resonators, and so is best studied using pairs.

The purpose of this Chapter is twofold. First, I give a rigorous analysis of the interaction between a pair of co-axial SRRs with one ring rotated, and determine the conditions under which the dispersion curves will undergo a crossing or avoided crossing. I introduce a physically-based model for describing the interplay between the magnetic and electric near-field interactions, and show how this model explains the experimentally and numerically observed dispersion behavior.

In 2007 H. Liu et al. [79] analyzed numerically an array consisting of pairs of split ring resonators on the same axis, with the second ring rotated by 90°. The hybridized modes of this system show strong polarization rotation, and have suppressed radiation losses [83]. Subsequently, N. Liu et al. [84] investigated a similar system, but considered an arbitrary angle between the two rings. Using numerical analysis, they extracted the eigenmodes of a pair of SRRs operating in the near infrared. They concluded that as the twist angle increases, the resonances converge, undergo an avoided crossing, then di-

verge again. The reason for this avoided crossing is not clear, since the previous study by Powell et al. of a different systems of coupled SRRs showed that the hybridized modes can cross [76]. In Ref. [84] the dispersion curve with an avoided crossing was fitted by a multipole interaction model, however no physical justification for this fitting was given. In particular, it was assumed that the magnetic interaction constant is invariant with twist angle, however this is inconsistent with the strong variation of current density around the circumference of the ring. This model was subsequently extended to include the polarization-rotation of the scattered radiation [85].

In Section 2.1, I present the experimental and numerical analysis of the dispersion curves. I also investigate the effect of losses and the waveguide on the dispersion curves. In Section 2.2.1 I show how the dispersion curves can cross, based on an idealized model of a pair of SRRs. Finally, in Section 2.2.2 the influence of losses and non-identical rings on the dispersion curves is considered. Using the theory of Morse critical points, it will be shown that competition between losses and differences in the resonant frequencies of the rings will determine whether or not the modes cross.

The work presented in this chapter is a collaboration predominantly between myself and David Powell. The experimental and numerical results were completed by myself, and the calculations in Section 2.2 by David Powell.

2.1 Experimental results

I consider a pair of SRRs with varying twist angle θ between them shown schematically in Fig. 2.1 (a). First, microwave experiments are performed using pairs of rings, with one ring held fixed, and a separate sample created for each rotated ring. The rings have an inner radius of 3.5 mm, an outer radius of 4 mm, and a gap of 1 mm. They are copper, printed at fixed angles onto 1.6 mm thick FR4 circuit board, and the rings 3.6 mm apart, with the dielectric boards located between the rings. The incoming microwaves are polarized so that the electric field is across the gap of the fixed ring, as shown in Fig. 2.1 (a).

The experiments are conducted inside a WR-229 rectangular waveguide, which has a recommended band of operation from 3.3 - 4.9 GHz, over which the waveguide only

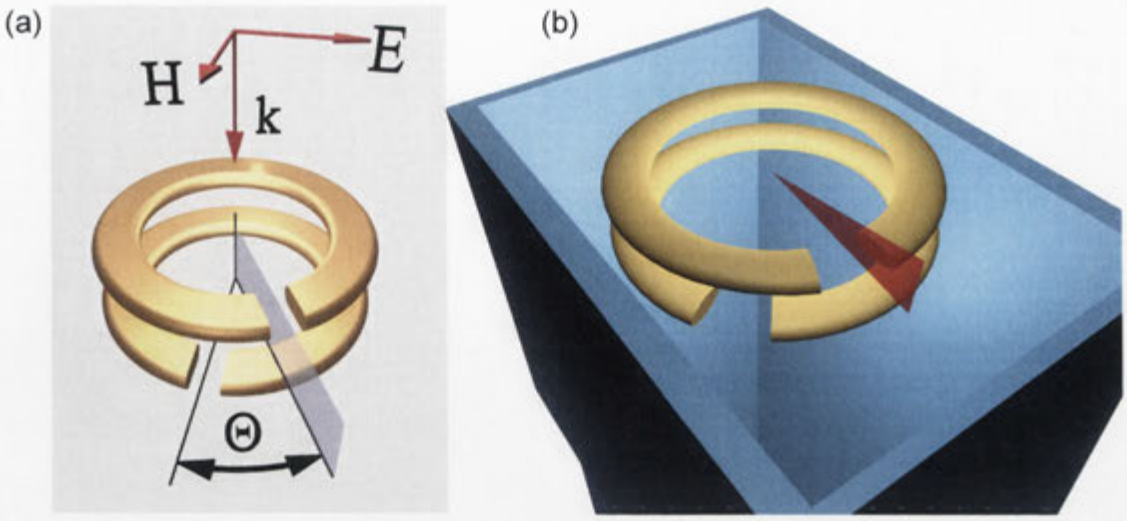

Figure 2.1: (a) A schematic showing the rings rotated with respect to each other through angle θ, and the polarization of the incoming waves. (b) Schematic diagram of the rings inside the waveguide. The size of the rings in relation to the waveguide is greatly exaggerated.

has one propagating mode, TE_{10}. At 5 GHz, the decay rate for the TE_{20} mode is 5.3 mm, much smaller than the length of the waveguide. The experiments are designed to operate within this frequency range. A Rohde and Schwarz ZVB network analyzer is used to measure the resulting transmission and reflection coefficients. A depiction of the twisted rings inside the waveguide is shown in Fig. 2.1 (b). The relative size of the rings to the waveguide is greatly exaggerated in this figure. The excitation of the rings is measured using the absorption of the system, which describes the maximum currents on the rings. The absorption is given by $1 - |S_{21}|^2 - |S_{11}|^2$, where S_{21} is the transmission coefficient, and S_{11} is the reflection coefficient. An example of the absorption is compared to the corresponding transmission and reflection in Fig. 2.3 (a).

To match the experimental data, I perform numerical calculations using CST Microwave Studio, a numerical simulator designed for three dimensional simulation of high frequency components. The rings are simulated as copper, and the boards as FR4 with a dielectric constant of 4.6, and a loss tangent ($\tan(\delta)$) of 0.025. At microwave frequencies, the dielectric constant of FR4 is ill-defined, so the value is chosen based on what best agrees with the experimental results. The losses in the copper rings are negligible compared to the losses in the substrate.

To characterize the dispersion behavior, experiments are performed with θ varied from 0° to 180° in 10° increments, while numerical results are calculated in 5° incre-

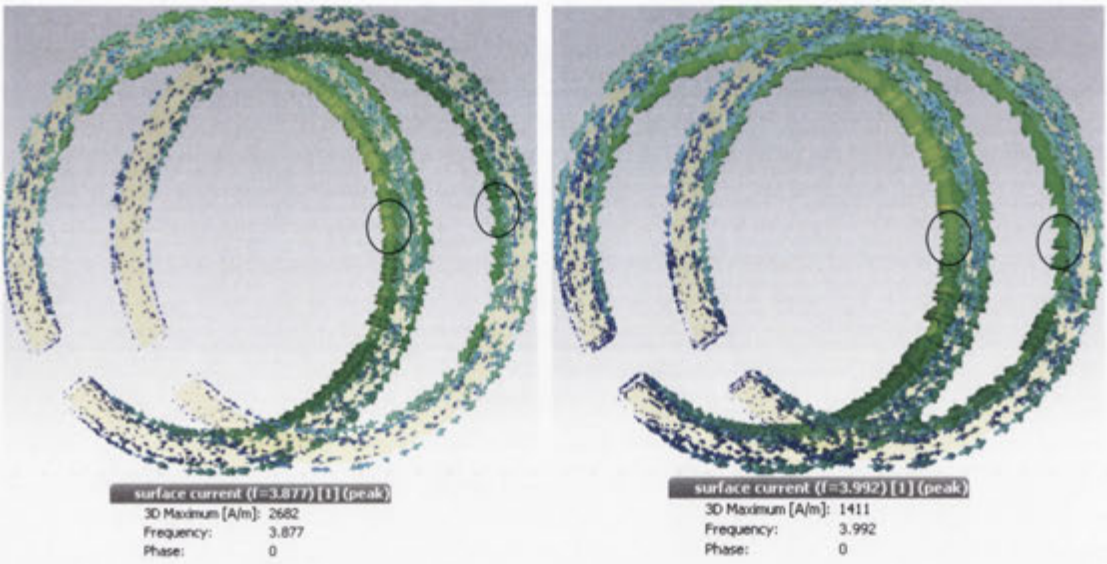

Figure 2.2: Numerically calculated current distributions for the (a) antisymmetric (b) and symmetric resonant frequencies, for $\theta = 0°$. The circled areas shows the current directions to compare, and the relevant frequencies are in the boxes in GHz.

ments. The current distribution on the rings is monitored at the resonant frequencies, an example of which is shown in Fig. 2.2, for $\theta = 0°$. The resonant frequencies at this angle are 3.877 GHz and 3.992 GHz, and by inspection of the simulated currents in the rings at these frequencies, I verify that these correspond respectively to the expected antisymmetric (Fig. 2.2 (a)) and symmetric (Fig. 2.2 (b)) resonances. These resonances are dominated by these modes, but may have errors due to contribution from the other mode, the finite mesh or the selection of plotting points by CST. Comparisons of the absorption curves for $\theta = 0°$, $\theta = 90°$ and $\theta = 180°$ are shown in Figs. 2.3 (b, c and d) respectively. For θ =0°, there are two resonances ω_S and ω_{AS}. As θ increases, ω_{AS} increases and ω_S decreases, reaching their maximum and minimum values respectively at θ =180°.

As can be seen in Figs. 2.3 (b-d) and Fig. 2.4 (b), the two resonant peaks have different widths, which are primarily due to differing radiation losses. The symmetric mode has relatively stronger radiation losses for low angles, since each ring approximates an electric dipole, and a pair of parallel dipoles radiate strongly. As the angle approaches 180°, the dipoles become oppositely directed, thus there is the low radiation efficiency of an electric quadrupole/magnetic dipole like distribution [87]. The antisymmetric mode has the charges on one ring of the opposite sign to the other, therefore it changes from

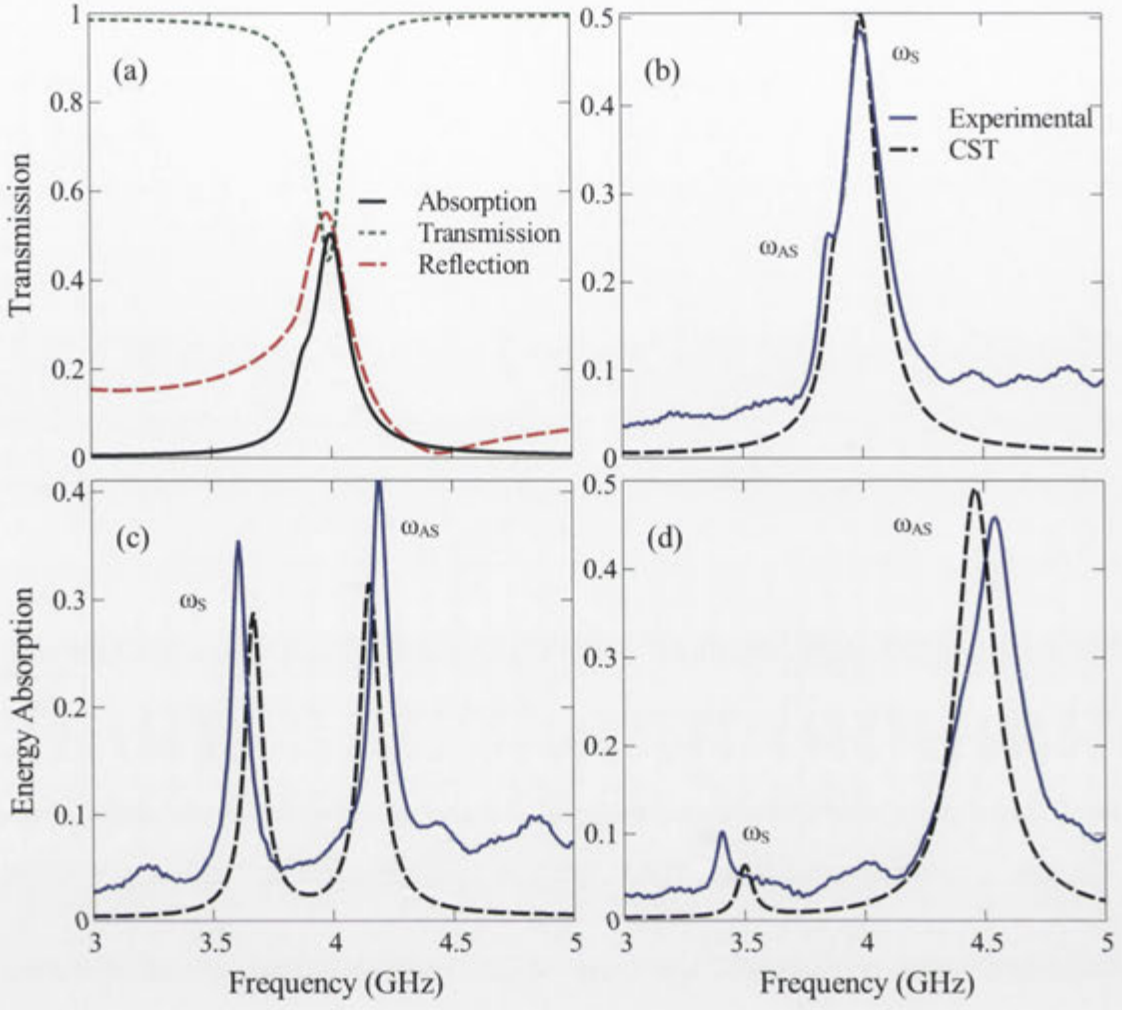

Figure 2.3: (a) A comparison of the numerically calculated transmission, reflection and absorption curves for $\theta = 0°$. (b-d) Numerical (dashed) and experimental (solid) absorption curves for (b) $\theta = 0°$, (c) $\theta = 90°$ and (d) $\theta = 180°$.

an electric quadrupole to an electric dipole type distribution with increasing angle, and the radiation efficiency increases.

For each angle a Fano function [88] is fitted to the experimentally and numerically obtained absorption curves, in order to minimize errors in the peak due to background noise fluctuations. Due to the strong coupling of the resonance to the radiating waves, the data has an asymmetric lineform, which cannot be reproduced using fitting procedures such as the Lorentz function. The Fano function is chosen as it has the degrees of freedom to reproduce the observed spectral features. This function is typically expressed in the normalized form [88]

$$F = \frac{(\Omega + q)^2}{\Omega^2 + 1}, \tag{2.1}$$

where q is a phenomenological shape parameter and $\Omega = 2(\omega - \omega_r)/\gamma$, with $\omega_r/2\pi$ being the resonant frequency, and γ the damping coefficient. The value of q determines the amplitude and asymmetry of the curve, and can range from $-\infty$ to ∞. However, the large values that q can take on cause numerical problems for the fitting procedure, so additional parameters a and n are introduced, which account for the amplitude of the peak and the non-resonant contribution to the absorption, and q is replaced with ξ, which is an asymmetry parameter. Now the following equation will be used:

$$F = n + \frac{a\,(\xi\Omega + 1)^2}{\Omega^2 + 1}. \tag{2.2}$$

This modified equation allows for accurate fitting of the curve to the data.

The fitting procedure uses a least squares optimization to find the values of the variable parameters (a, n, ω_r, γ and ξ). The resulting resonant frequencies and damping coefficients are shown in Figs. 2.4 (a) and (b) respectively. In all cases the data are well-described by a pair of Fano resonances with a correction for background absorption, and the fitting to the numerical results has a residual error below 5×10^{-3}. The fitting error, for both the frequency and the damping rate, is estimated to be around 10^{-4} GHz. The disagreement between the experimental and numerical results, particularly for the antisymmetric mode, is predominantly due to fabrication imperfections.

2.1.1 Crossing of resonant modes

Inspection of Fig. 2.4 (a) shows that the resonances appear to cross at $\theta \approx 34°$. Considering only the resonant frequencies, the possibility of a narrowly avoided crossing too small to resolve cannot be eliminated. However the numerically determined loss coefficients γ shown in Fig. 2.4 (b) can be directly identified with the corresponding resonant frequencies since they are derived from the same fitted peaks. The absorption coefficients remain clearly distinct in the region of the crossing (confirmed by additional numerical simulations in 0.02° steps), thus the resonant frequencies are not exchanged and there is *a clear indication of a crossing of modes*.

While there could be multiple local minima of fitted parameters, it is known from [89] that the dispersion curve must be a continuous function. The real part must either continue or exchange. The fact that the dispersion curves in Fig. 2.4 are continuous give

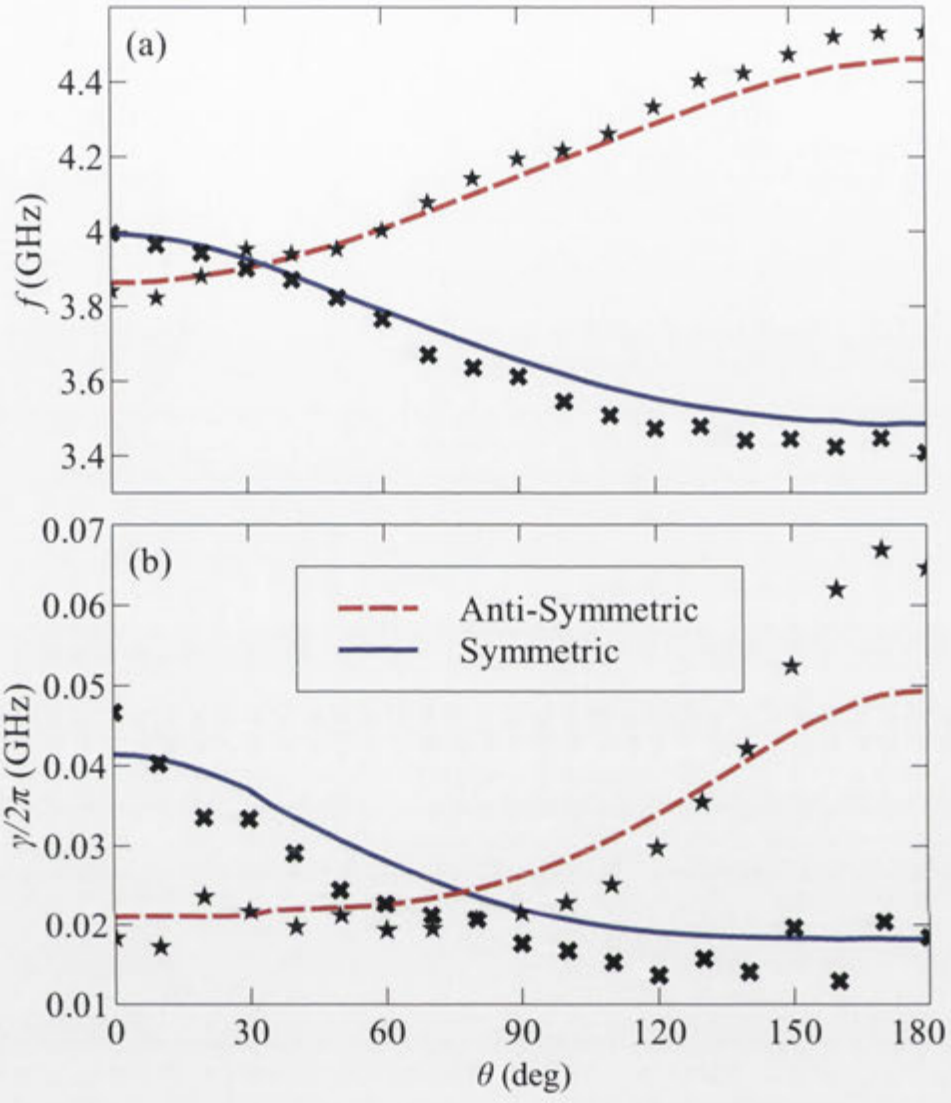

Figure 2.4: (a) A comparison of the experimental (markers) and numerical (lines) resonant frequencies. (b) Corresponding damping coefficients, calculated from the resonance line-widths.

confidence in the fitting procedure. If a different minima were obtained, there would be non-physical jumps in the dispersion.

In Fig. 2.5 I have plotted the numerical absorption spectrum in the vicinity of the crossing. It has the appearance of only a single peak, however the fitting procedure still identifies two separate resonances, which are also plotted for comparison purposes. It can be seen that the symmetric peak is much stronger than the antisymmetric peak, but they are both still clearly present.

In general the experimental data show good agreement with the numerical data, but

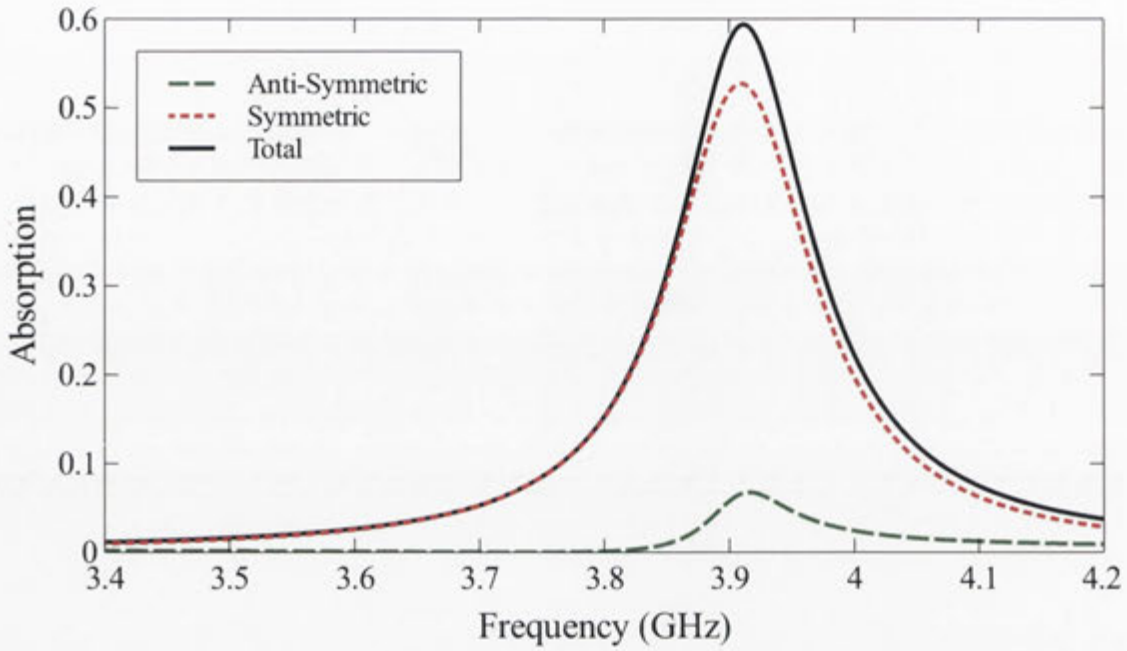

Figure 2.5: Numerical absorption curve (solid) for θ =34° at the crossing, showing the two fitted resonances (dashed).

with some uncertainties due to fabrication tolerances.

2.1.2 Factors influencing the dispersion

The crossing of modes is influenced by a number of factors in the system, and some of these factors will now be studied numerically, including the losses in the system and the symmetry breaking caused by the presence of the waveguide.

One of the main factors in the strength of the coupling of the system is the separation between the resonators. Fig. 2.6 (a) shows the frequency dispersion for a separation between the boards of 3.2 mm, which is a slight change from the original separation of 3.6 mm. By comparing the curves with Fig. 2.4 (a), it can been seen that the dispersion relation is similar, though both modes are shifted to a higher frequency. The apparent crossing of modes also occurs around the same angle.

The losses in the substrate have a significant influence on the width of the resonances, so removing them should enhance the resonances, and separate them further, especially closer to resonance. Figure 2.6 (b) shows the dispersion curves for the original system of separation 3.6 mm, with the losses in the substrate removed. It can be seen that the crossing angle increases to around 40°, and the resonances are slightly fur-

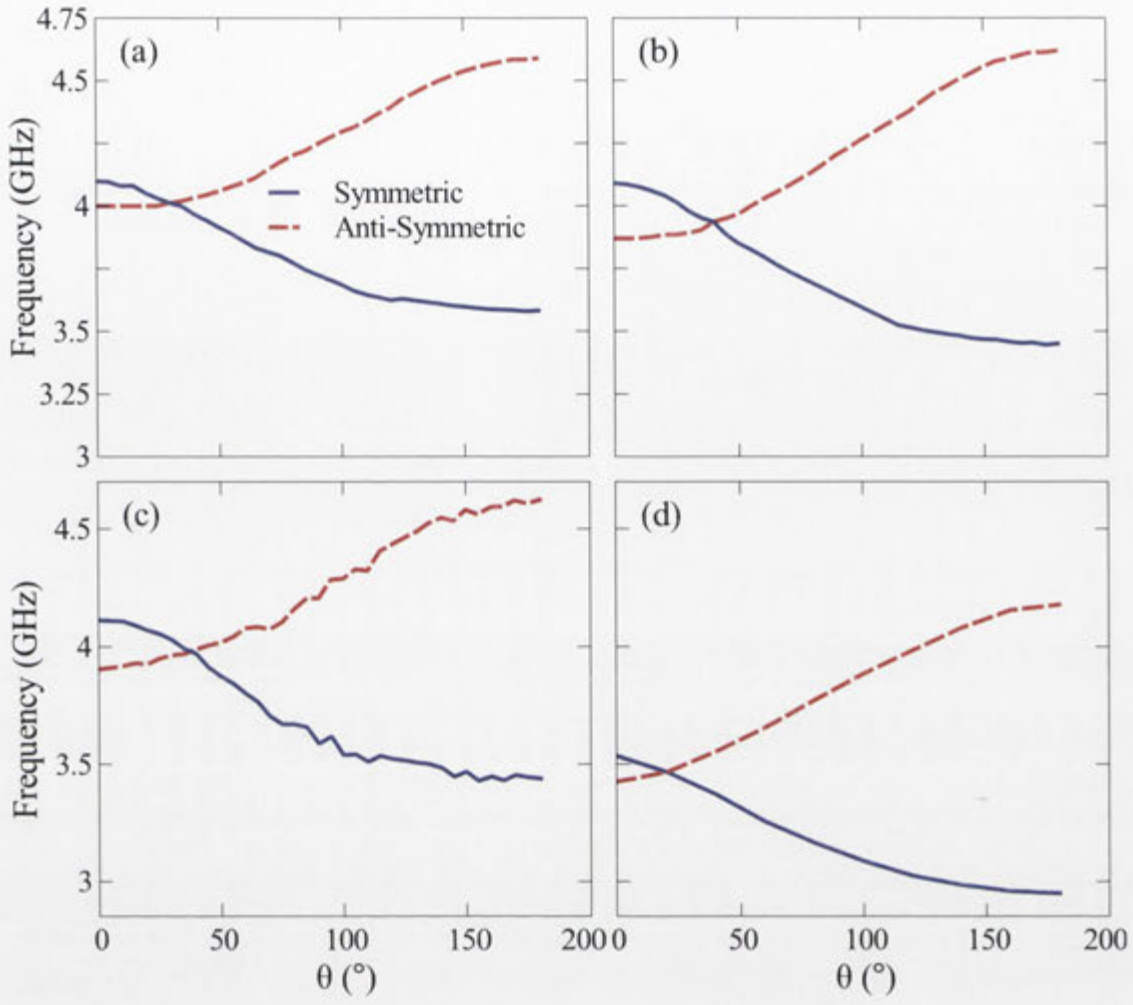

Figure 2.6: Numerical dispersion relations, for both symmetric (solid) and antisymmetric (dashed) modes, for (a) a separation of 3.2 mm, (b) the losses removed from the substrate, (c) the waveguide removed, and (d) a separation of 1.6 mm without the waveguide.

ther apart, especially closer to the crossing point where removing the losses cause the resonances to be better distinguished from each other, as expected.

In my system, the experiment was conducted inside a rectangular waveguide, which causes a breaking of the symmetry, due to each ring having a different relative orientation to the waveguide, dependent on the angle between the rings. Figures 2.6 (c, d) explore the effect of the waveguide on the frequency dispersion. Figure 2.6 (c) shows the frequency dispersion for the case where the waveguide is removed, and the rings are separated by a distance of 3.6 mm. The boards are modeled in this simulation as being loss free. It can be seen that there is again a crossing, and that the dispersion relation is actually very similar to that in Fig. 2.4 (a). The apparent noise in the numerical frequency dispersion is due to imperfect meshing in the CST simulation. Figure 2.6 (d)

then considers the case where the spacing is reduced to 1.6 mm. It can be seen that this change in coupling lowers the resonant frequency significantly, as well as lowering the crossing angle. However, the splitting between the modes is very similar, which is surprising.

In the systems considered here which appear to have a crossing of modes, it cannot be said for certain that this is the case, only that if an avoided crossing exists then it must be small. Therefore it is necessary to have a theoretical basis for understanding the dispersion curves, which will be developed in Section 2.2.1. Subsequently in Section 2.2.2 the effects of experimental error will be included in the model, thus the theory can be used to evaluate the reliability of my conclusion from the experimental results.

2.2 Theory of crossing

2.2.1 Identical and lossless Rings

The tuning of the system by rotation can be explained by looking at the interaction between the rings. As the rings are twisted, the magnetic and electric near-fields between the two rings change, changing the coupling between them. This problem is first approached using the Lagrangian for a pair of identical and lossless resonators [76,84]

$$\mathcal{L} = \frac{L}{2}(\dot{Q}_1^2 + \dot{Q}_2^2 + 2\kappa_M \dot{Q}_1 \dot{Q}_2) - \frac{1}{2C}(Q_1^2 + Q_2^2 + 2\kappa_E Q_1 Q_2), \tag{2.3}$$

where $Q_{1,2}(t)$ are the time-dependent amplitudes of the modes' charge distributions, the rings have resonant frequency $\omega_0 = (LC)^{-\frac{1}{2}}$, and κ_M and κ_E are the dimensionless magnetic and electric interaction constants. κ_M is defined by the interaction of the magnetic field with the currents on the rings, and κ_E by the interaction of the electric field with the charges on the rings. These interaction coefficients are calculated from the electro-static ($W_{H,mn}$) and magneto-static ($W_{E,mn}$) stored energies in the system:

$$\kappa_E = \frac{W_{E,12}}{W_{E,11}}, \qquad \kappa_M = \frac{W_{H,12}}{W_{H,11}}. \tag{2.4}$$

These energies are derived from the numerically retrieved charge $q(\mathbf{x})$ and current $\mathbf{j}(\mathbf{x}')$ distributions:

$$W_{E,mn} = \int_{V_m} \mathrm{d}^3x \int_{V_n} \mathrm{d}^3x' \frac{q(\mathbf{x})\, q(\mathbf{x}')}{4\pi\epsilon_0 \|\mathbf{x}-\mathbf{x}'\|}, \tag{2.5}$$

$$W_{H,mn} = \int_{V_m} \mathrm{d}^3x \int_{V_n} \mathrm{d}^3x' \frac{\mu_0 \mathbf{j}(\mathbf{x}) \cdot \mathbf{j}(\mathbf{x}')}{4\pi \|\mathbf{x}-\mathbf{x}'\|}. \tag{2.6}$$

By substituting Eq. (2.3) into the Euler-Lagrange equation the dynamic equations are found to be

$$\begin{aligned} \ddot{Q}_1 + \omega_0^2 Q_1 &= -\kappa_M \ddot{Q}_2 - \kappa_E \omega_0^2 Q_2, \\ \ddot{Q}_2 + \omega_0^2 Q_2 &= -\kappa_M \ddot{Q}_1 - \kappa_E \omega_0^2 Q_1. \end{aligned} \tag{2.7}$$

Solving the characteristic equation for this system gives two resonances: symmetric ($Q_1 = Q_2$), and antisymmetric ($Q_1 = -Q_2$):

$$\omega_S = \omega_0 \sqrt{\frac{1+\kappa_E}{1+\kappa_M}}, \qquad \omega_{AS} = \omega_0 \sqrt{\frac{1-\kappa_E}{1-\kappa_M}}. \tag{2.8}$$

For a pair of rings in *a homogeneous dielectric background*, the electric and magnetic interaction constants can be determined from the interaction energy between resonators, using the method described in Ref. [76]. The rings studied have the same dimensions as the rings used to obtain Fig. 2.4. The resulting interaction constants are shown by the markers in Fig. 2.7 (a), along with the following functions which fit the data very well:

$$\kappa_E = \kappa_{E1} \cos(\theta) \qquad \kappa_M = \kappa_{M0} + \kappa_{M1} \cos(\theta) \tag{2.9}$$

with $\kappa_{E1} = 0.085$, $\kappa_{M0} = 0.098$ and $\kappa_{M1} = 0.05$. These constants relate to the charge separation across the gap of the ring, the current circulating around the ring, and the inhomogeneity of the current distribution around the ring, respectively. They are found by fitting to the angle dependency of κ_E and κ_M.

For rings aligned on the same axis, it is expected that the magnetic interaction κ_M should always be positive, as the intersecting magnetic field from one loop should always be normal to the other loop. In addition the electric interaction κ_E should be positive at $\theta = 0°$ as the charge distribution has the nature of parallel dipoles. All arrangement of rings on the same axis which were considered behaved in this manner.

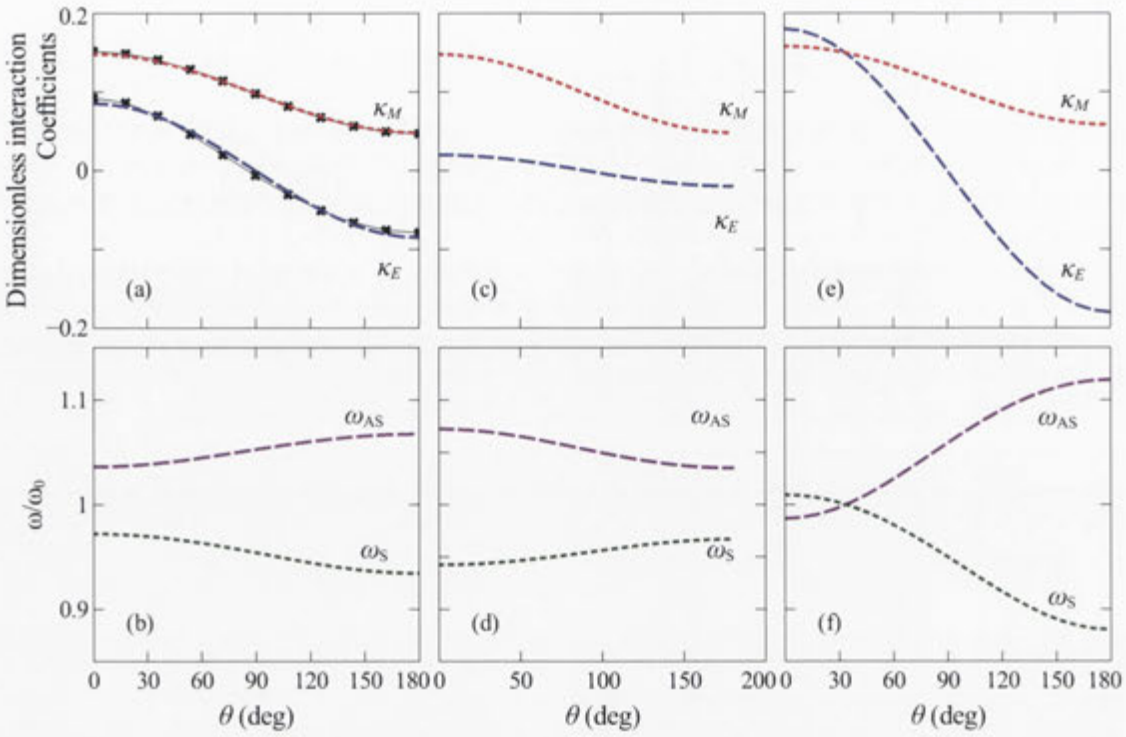

Figure 2.7: (a) Magnetic (κ_M) and electric (κ_E) interaction constants calculated for a pair of rings in free space. Dots show exact calculations, lines give the fitted function, and (b) shows the corresponding resonant frequencies. (c) Interaction where the variation in magnetic coupling dominates, and (d) corresponding resonant frequencies. (e) Interaction constants which become equal, and (f) corresponding resonant frequencies which cross.

In Fig. 2.7 (b) the corresponding frequencies of the symmetric and antisymmetric modes are plotted, normalized to ω_0. As this approach models the response of the resonators in a homogeneous dielectric background, the results are significantly different from those observed experimentally, where the dielectric is inhomogeneous and the effect of waveguide boundaries is also significant. In particular, for this system of perfectly conducting rings, the crossing of resonances cannot be reproduced in a homogeneous background. Therefore, the possible regimes of interaction which may occur are considered, under the assumption that the interaction constants will be of the form described in Eq. (2.9).

The case considered in Figs. 2.7 (a, b) corresponds to the magnetic interaction always being larger than the electric interaction. This results in increasing splitting of ω_S and ω_{AS} with increasing twist angle, however in principle there is no reason why the splitting cannot decrease. Such a case is shown in Figs. 2.7(c, d), where κ_{E1} is set to $0.02 < \kappa_{M1}$, such that the inhomogeneity in the current has a stronger influence than the

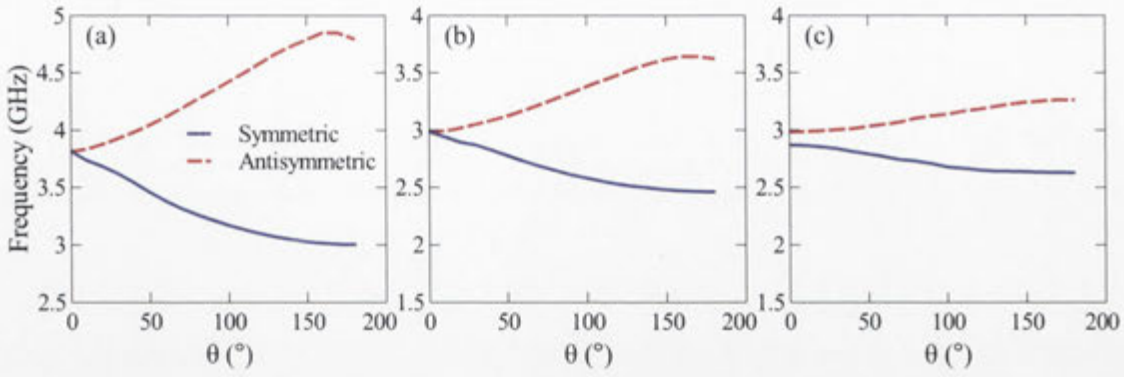

Figure 2.8: Numerical dispersion relations for a pair of rings simulated in a homogeneous dielectric, in a periodic array. (a) The background dielectric is 1, with the rings separated by 1.6 mm; (b) the background dielectric is 4.6, with the rings separated by 1.6 mm; and (c) the background dielectric is 4.6, with the rings separated by 3.2 mm. The symmetric mode is represented by the solid blue line, and the antisymmetric the dashed red.

dipole-like charge distribution. Despite the different behavior of the frequency splitting curves, there is little qualitative difference between the interaction constants shown in Figs. 2.7 (a) and (c).

The only other case allowed in this model of interaction under the afore-mentioned physical constraints on κ_M and κ_E is that $\kappa_M < \kappa_E$ for $\theta = 0°$. An example of this is given in Fig. 2.7 (e), where κ_{M0}, κ_{M1} and κ_{E1} are set to 0.108, 0.05 and 0.18 respectively, such that $\kappa_E = \kappa_M$ at $\theta \approx 34°$. The corresponding resonant frequencies normalized to ω_0 are plotted in Fig. 2.7 (f). The parameters have been chosen to closely match the dispersion shown in Fig. 2.4 (a). From this match between the model and the experimental data, it can be concluded that the inhomogeneous dielectric enhances the electric interaction between the rings but has almost no influence on the magnetic interaction, as expected.

As the changing of the dispersion relations is dependent on the electric interaction κ_E, I can attempt to investigate these dispersion numerically by studying the effect of the dielectric on the response. In order to do this, pairs of rings are simulated in a homogeneous dielectric background, with both the background dielectric and spacing between the rings being altered. These simulations are performed in a periodic array, to remove the effects of the waveguide. The unit cell has the same height and width as the waveguide, and the system is excited using Floquet modes. Simulations are designed to stay in approximately the same frequency range as the previous simulations. Figure 2.8 (a) shows the frequency dispersion for a background dielectric of 1, and a

separation of 1.6 mm. The rings have an inner radius of 6 mm, to prevent the resonant frequencies becoming too large. The width of the rings and gap size remain the same (0.5 and 1 mm respectively). It can be seen that there is significantly larger splitting between the modes here than for previous systems studied in this chapter, which will be due to the reduced separation between the rings, as well as the increased surface area on the rings, both factors which will lead to increased coupling between the rings. It can also be seen that there is no crossing of the modes, but they appear to both start at the same frequency. This frequency dispersion bears resemblance to that shown in Fig. 2.7 (b), where the frequency dispersion was calculated from the interaction coefficients.

The frequency dispersion for the same arrangement but with a background dielectric of 4.6 is shown in Fig. 2.8 (b). The rings in this simulation are significantly smaller than those in Fig. 2.8 (a), to account for the increased dielectric. These rings are of inner radius 2.5 mm. The frequency dispersions between the two systems are very similar qualitatively but the second system has much smaller splitting. This is probably due to the decrease in surface area on the rings. The resonances are lower than the previous measurements, to prevent the need for even smaller rings, however the scales on the graphs are the same. The qualitative similarity between the dispersions shown in Figs. 2.8 (a, b) show that increasing the background dielectric does not appear to affect the shape of the interaction coefficients. This is because the background dielectric constant cancels from the normalized interaction coefficients.

Figure 2.8 (c) then shows the dispersion for the previous system with the separation between rings increased to 3.2 mm. As expected, the coupling between the rings is greatly reduced, as seen by the significantly reduced splitting between the modes. This decrease in the coupling has also resulted in the appearance of two clear, separate resonances at $0°$, resulting in a frequency dispersion very similar to that in Fig. 2.7 (b). As the larger coupling in Fig. 2.8 (b) resulted in the modes being equal at $0°$, it would be of interest to see whether increasing the coupling further could cause the modes to be equal at a larger angle, resulting in a frequency dispersion to resembling that in Fig. 2.7 (f). However, due to higher order Floquet modes becoming propagating, there is a limit to how large a frequency range can be easily simulated over using CST, which limits the splitting which can be simulated.

Equations (2.8) show that the tuning curves arise from competition between electric and magnetic interaction constants. If the magnetic and electric interaction constants have the same sign, then they will counteract each other. Thus the frequency splitting can be weak even if the near-field interaction is strong. In particular, the model shows that there is no splitting when $\kappa_M = \kappa_E$. This crossing of the real parts of the dispersion is in agreement with the numerical results presented in Fig. 2.4.

2.2.2 Non-identical and lossy Rings

Up to this point, a theoretical account of interaction which predicts a crossing of modes, and which is consistent with experimental results and numerical calculations has been given. However, a single ring within the waveguide will have some variation of its resonant frequency as it is rotated, due to interactions with the image currents in the waveguide walls. Similar effects should occur for rings which form part of a larger planar lattice. In addition, there will be further contribution due to fabrication uncertainties. Therefore the pair of twisted rings should be modeled as non-identical resonators. In addition, the theory developed in Section 2.2.1 has not included the influence of losses, neglecting the strong radiation from the rings into the waveguide modes, as well as ohmic dissipation.

One would expect that differences between the two rings would result in an avoided crossing, following well-known results from coupled-mode theory [80]. However such results rely on the Hermitian nature of the system, and are not valid once losses are considered. Therefore this question will be investigated using the theory of Morse critical points, which has previously been applied to resonators and waveguides [90–92]. In Ref. [89] an approach was demonstrated which showed the conditions for a crossing or anti-crossing of modes, and in particular demonstrated that losses can counteract an avoided crossing. This approach is now applied to this system of rotating rings, and the key results are presented. For a complete derivation and theoretical background, the reader is referred to Ref. [89].

First the system of equations given by Eqs. (2.7) is modified by introducing dissipation coefficients $\Gamma_{1,2}$ and a detuning parameter $\delta\omega$, where $2\delta\omega$ is the difference between the individual resonant frequencies of the two rings, and $\Gamma_{1,2}$ are the damping coeffi-

cients retrieved using the Fano fitting. The resulting equations are:

$$\begin{aligned} \ddot{Q}_1 + 2\Gamma_1\dot{Q}_1 + (\omega_0 + \delta\omega)^2 Q_1 &= -\kappa_M \ddot{Q}_2 - \kappa_E \omega_0^2 Q_2. \\ \ddot{Q}_2 + 2\Gamma_2\dot{Q}_2 + (\omega_0 - \delta\omega)^2 Q_2 &= -\kappa_M \ddot{Q}_1 - \kappa_E \omega_0^2 Q_1. \end{aligned} \tag{2.10}$$

By taking the time dependence of $Q_{1,2}$ as $\exp(j\omega t)$, the following dispersion equation is arrived at:

$$\begin{aligned} D(\omega,\theta) = \left[(\omega_0 + \delta\omega)^2 + j2\Gamma_1\omega - \omega^2\right] \times \left[(\omega_0 - \delta\omega)^2 + j2\Gamma_2\omega - \omega^2\right] \\ - \left[\kappa_E(\theta)\omega_0^2 - \kappa_M(\theta)\omega^2\right]^2 = 0 \end{aligned} \tag{2.11}$$

The solutions of this system are not strictly symmetric and antisymmetric, although for small $\delta\omega$ and for angles away from the avoided-crossing they are only slightly perturbed from the original modes. This model neglects the differences in radiation losses of the symmetric and antisymmetric modes, which also vary with twist angle. For this example κ_M and κ_E are given by Eq. (2.9), with the same coefficients used to derive Figs. 2.7 (e, f).

The dispersion curves of the system correspond to the condition $D(\omega,\theta) = 0$. In applying the theory of Morse critical points, the behavior of the function $D(\omega,\theta)$ in the neighborhood of the crossing/anti-crossing is studied, and the values of (ω,θ) which satisfy the dispersion equation are not limiting. This model is for the individual elements, and does not include a full analysis of the effect of the waveguide walls. The effects of the waveguide are that ω_0 is shifted, and the resonant frequency becomes angle dependent. This second effect is the main effect for this analysis, and is accounted for in $\delta\omega$

The first step is to find the Morse critical point (ω_m,θ_m) which satisfies $D'_\omega(\omega_m,\theta_m) = D'_\theta(\omega_m,\theta_m) = 0$. In the case of a crossing of modes, this will be approximately the point where the dispersion curves cross, in the case of an avoided crossing this will be a saddle-point of $D(\omega,\theta)$. In general this point must be found numerically, however if it is assumed that $\Gamma_1 = \Gamma_2 = \Gamma$, a sufficiently accurate solution is found by using

perturbation theory to first order in Γ:

$$\omega_m = \omega_{m0} + j\Gamma \tag{2.12}$$

$$\omega_{m0} = \left(\omega_0^2 + \delta\omega^2\right)^{\frac{1}{2}} \tag{2.13}$$

$$\cos(\theta_m) = \frac{\kappa_{M0}\omega_{m0}^2}{\kappa_{M1}\omega_{m0}^2 - \kappa_{E1}\omega_0^2} + j\Gamma\frac{2\kappa_{M0}\kappa_{E1}\omega_{m0}\omega_0^2}{\left(\kappa_{M1}\omega_{m0}^2 - \kappa_{E1}\omega_0^2\right)^2}. \tag{2.14}$$

In the vicinity of the Morse point a second-order Taylor expansion of $D(\omega, \theta)$ is performed

$$D(\omega,\theta) = D(\omega_m,\theta_m) + D''_{\omega\omega}(\omega-\omega_m)^2/2 + D''_{\omega\theta}(\omega-\omega_m)(\theta-\theta_m) + D''_{\theta\theta}(\theta-\theta_m)^2/2. \tag{2.15}$$

For this system the relevant partial derivatives can be calculated analytically, but the expressions are long and not particularly illuminating. From this local form of the dispersion equation, the solutions are given by:

$$\omega(\theta) = \omega_m - \frac{D''_{\omega\theta}}{D''_{\omega\omega}}(\theta-\theta_m) \pm \left(D''_{\omega\omega}\right)^{-1} \times \left[\left({D''_{\omega\theta}}^2 - D''_{\omega\omega}D''_{\theta\theta}\right)(\theta-\theta_m)^2 - 2D''_{\theta\theta}D(\omega_m,\theta_m)\right]^{\frac{1}{2}}. \tag{2.16}$$

This function has a pair of branch points, where the argument of the square root becomes zero. Upon substitution of the parameters of the system, it is found that the branch points occur at the following values[1] of θ:

$$\theta_{b1,2} = \theta_m \pm 2j\delta\omega\omega_0\frac{\sqrt{\left(\kappa_{M0}\kappa_{E1}\omega_0^2\right)^2 - \left(\kappa_{M1}^2\omega_{m0}^2 - \kappa_{E1}\omega_0^2\right)^2}}{\left(\kappa_{M1}\omega_{m0}^2 - \kappa_{E1}\omega_0^2\right)^2}. \tag{2.17}$$

As shown in Ref. [89], the position of branch points $\theta_{b1,2}$ on the complex plane determines the behavior of the resonant frequencies of the modes. In brief, if the imaginary parts of the two branch points have different signs, then the modes undergo an anti-crossing. However, the modes cross if the imaginary parts of the $\theta_{b1,2}$ have the same sign. This allows the effect of detuning $\delta\omega$ and losses Γ on the crossing–anti-crossing

[1] Strictly speaking the term inside the square root has some dependence on Γ, which in turn will cause it to become complex for $\Gamma \neq 0$. However both effects are negligible in this system.

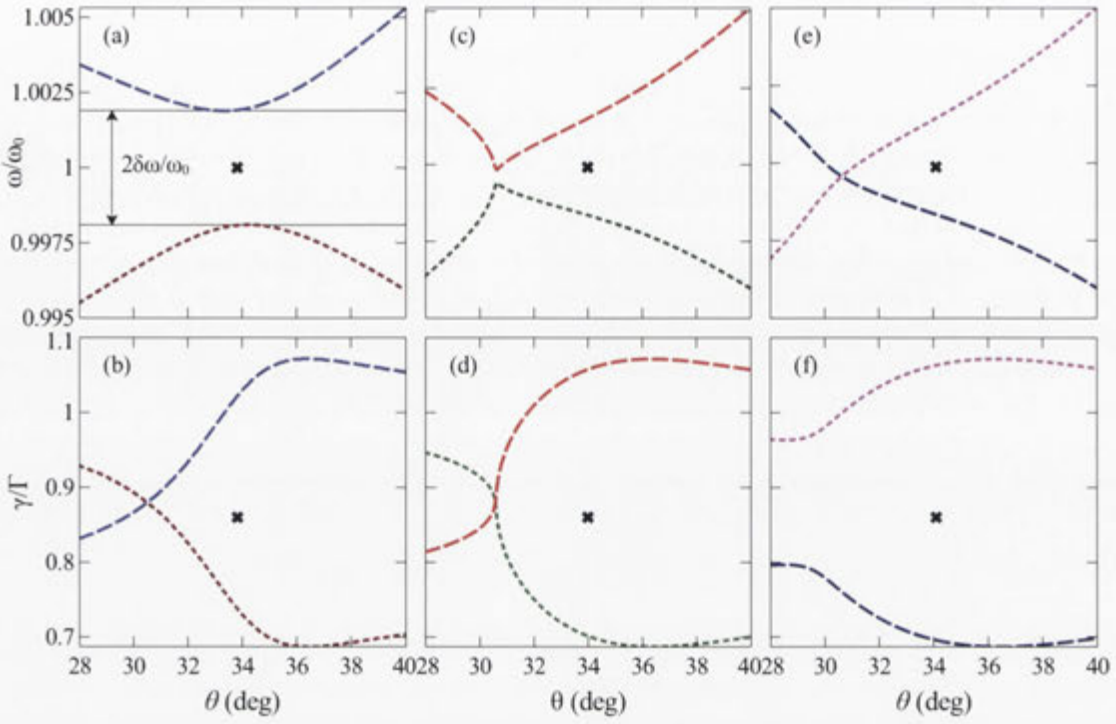

Figure 2.9: (a) Resonant frequencies and (b) absorption coefficients when $\Gamma = 1\times10^{-3}\omega_0$; (c) resonant frequencies and (d) absorption coefficients when $\Gamma = 7\times10^{-3}\omega_0$, showing that losses restore the crossing. (e) Resonant frequencies and (f) absorption coefficients when losses are increased to $\Gamma = 2\times10^{-2}\omega_0$. The projections of the Morse point are shown by crosses. In all cases $\kappa_{M0} = 0.108$, $\kappa_{M1} = 0.05$ and $\kappa_{E1} = 0.18$.

behavior of the system to be analyzed. To do this, a single ring is analyzed as it is rotated within the waveguide. By calculating the absorption spectra at $\theta = 0°$ and $\theta = 34°$, it is found that $2\delta\omega = 3.8\times10^{-3}\omega_0$, and that $\Gamma_1 = 1.8\times10^{-2}\omega_0$, $\Gamma_2 = 1.5\times10^{-2}\omega_0$. Therefore Γ_1 and Γ_2 are set to = Γ and 0.83Γ respectively, and the dispersion behavior as a function of Γ is analyzed. While both Γ and $\delta\omega$ are dependent on θ, in order to analyze the crossing of the modes, only the local behavior of the dispersion curve is studied, and so using Γ and $\delta\omega$ calculated at $\theta = 34°$ is justified.

To start with, weak losses are considered, when $\Gamma = 1\times10^{-3}\omega_0$. This case is very close to the lossless regime, and the real parts of frequencies are plotted in Fig. 2.9(a), where an avoided crossing can be seen, and in Fig. 2.9 (b) the imaginary parts, which are exchanged, are seen. As the losses are increased such that $\Gamma = 1.42\times10^{-2}\omega_0$, it can be seen from Fig. 2.9 (c) that the resonant frequencies approach close to each other, but do not cross. The corresponding loss coefficients in Fig. 2.9 (d) still cross over each other. As the losses are increased further to $\Gamma = 1.8\times10^{-2}\omega_0$ (as obtained from simulations), the

dispersion curve changes from an avoided crossing to a crossing, as shown in Fig. 2.9 (e) and (f). It is interesting to note that the losses also shift the angle of crossing away from the projection of the Morse point, which is exactly at the crossing in the lossless case.

Further simulations revealed that for $\Gamma = 1.8\times10^{-2}\omega_0$, the maximum permissible frequency detuning to maintain a crossing is $2\delta\omega = 4.8\times10^{-3}\omega_0$. This gives a bound on the total difference between the rings, including additional difference due to fabrication error. It was found from simulations that a change of 0.1 mm in either the radius or the ring gap would change $\delta\omega$ by $2.2\times10^{-3}\omega_0$, which gives $\delta\omega = 6\times10^{-3}\omega_0$, resulting in an anti-crossing. Experimentally fabricating samples with smaller error thresh-holds than this should be achievable, however verifying the experimental resonant frequencies of the individual rings is much more difficult. In this system there is a different sample for each angle, thus $\delta\omega$ will vary with angle due to varying fabrication errors. So while it cannot be guaranteed that our experimental system has a crossing of modes, there can be confidence that any anti-crossing would be small, and would be eliminated by improved fabrication tolerances.

In the simulations considered in the previous section, the effect of both the losses and the presence of the waveguide (representing the detuning in the system) were studied. As removing the losses from the substrate does not affect the appearance of the crossing of modes discussed in Section 2.1.1, as shown by Figs. 2.5 and 2.6 (b), the likelihood of the losses in the initial system being too low for a crossing to occur is minimal. The effect of the waveguide's presence is harder to qualify further from the considerations above.

From the numerical results in Fig. 2.4 (c) and Fig. 2.9 (d), it can be seen that the decay constants of the hybridized modes are quite different, due to different radiation losses. It should be noted that if complete degeneracy of both the frequency and decay constants of the eigenmodes could be achieved, then the coupling between the rings would be completely suppressed, as the electric and magnetic coupling would cancel each other out. The case shown in Fig. 2.9 (c - d) is very close to this at the point of the avoided crossing, which can be seen where γ becomes equal for both modes, and the frequencies are very close. Indeed, there exists a critical value of Γ at the transition between the crossing and avoided crossing regimes. In practice it would be quite diffi-

cult to achieve this experimentally, however if such compensation could be realized this would have important implications for mitigating spatial-dispersion, as the coupling between neighboring rings is one of the contributors.

2.3 Conclusion

In this chapter I have studied the effect of twisting rings relative to each other, in order to further understand the near-field response. This involved using numerical and analytical means to investigate the crossing of the resonant modes in the system.

I have shown in a series of experiments how changing the relative rotation between two rings modifies the electric and magnetic interaction between them, thus tuning the hybridized resonances. Both the resonant frequencies, and the Q factors were tuned, which resulted in an apparent crossing of the symmetric and antisymmetric modes. This crossing was studied further using numerical simulations, with both symmetric and antisymmetric resonances found to coexist at this point.

The effect on the frequency dispersion, of the losses in the system and of breaking the symmetry were then studied. They were both found to have some effect on the angle of crossing.

Using both numerical simulations and an analytical model that takes into account both electric and magnetic interactions between the rings, this crossing of modes was further investigated. It was found that there are different regimes of dispersion curves, determined by the relative interaction coefficients. The effect of the dielectric in the system was studied numerically.

It was also found that there is a crossing where the two resonances coexist, at an angle where the electric and magnetic coupling are equal. It was also shown that the waveguide walls and experimental errors can cause the crossing of the dispersion curve to be avoided, however using the theory of Morse critical points, it has been demonstrated that increasing the losses can cause the crossing to be restored.

This study of the crossing of modes has shown how the near-field interaction can be used to understand the tuning of resonances. The near-field response could be used as

a tool in manipulating the properties of metamaterials to address current weaknesses. In particular, this could be used as a further degree of freedom in designing nonlinear and chiral metamaterials.

Chapter 3

Tuning the Nonlinear Response of Coupled Split Ring Resonators

As discussed in Section 1.1.4, nonlinear materials can have a response which is power dependent. Nonlinear meta-atoms can be created by adding a nonlinear inclusion to a resonant element, which will react to the high power incident field. In particular, metamaterials can exhibit a response much stronger than natural materials, due to their resonant nature and the local field enhancement which occurs at certain "hot spots". This effect has been investigated for SRRs with varactor diodes attached across gaps in the ring [77]. Systems with one and two attached varactors were studied experimentally and analytically in Ref. [67], and it was found that the nonlinear effect could be described using the second and third order susceptibilities.

The strength of the local field depends on the design of the resonator, and the choice of an optimal location to place the nonlinear element. However it also depends strongly on the coupling of the wave to the external field, which along with losses determines the quality factor of the resonator. Since modifications of the lattice parameters also influence the quality factor of the resonances [76], they should affect the local-field enhancement. The effect of the arrangement of meta-atoms on nonlinear properties has previously been studied at optical frequencies. It was found that the relative orientation of L-shaped resonators in an array could affect the second-order nonlinear properties by up to a factor of fifty [86].

In this Chapter I introduce the concept of controlling the nonlinear response of the metamaterial by altering its internal structure. Previously it was shown that the lin-

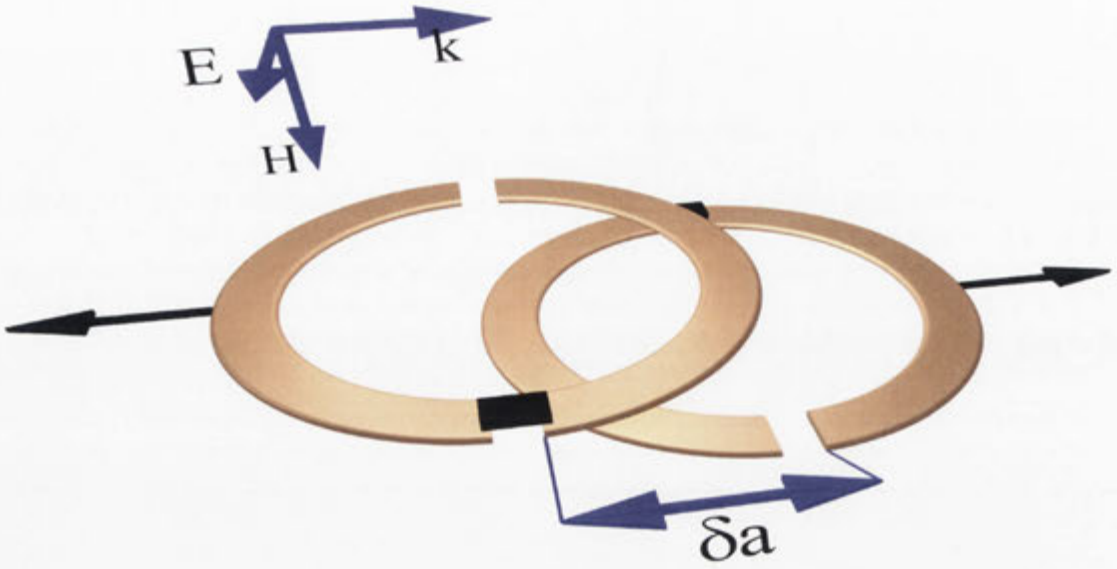

Figure 3.1: Schematic of the lateral shifting of SRRs with inserted varactor diodes showing the directions of the incident fields; δa is the shift between two rings.

ear properties of a system could be controlled via laterally offsetting the resonant elements [70]. By offsetting the resonators I now control the maximum currents through the nonlinear driving elements, which affects the nonlinear response of the system. In Section 3.1 I experimentally demonstrate *control of the nonlinear response* of two coupled split-ring resonators by changing their mutual position. This effect is achieved through modification of the structure of the coupled resonant modes, and their interaction with the incident field. The effect of breaking the symmetry is also investigated. In Section 3.2 I then investigate how this response occurs, by studying the linear properties of the system. These properties include the absorption on the rings, and the voltage across the varactor diodes.

3.1 Experimental results

I start by performing microwave experiments with a pair of SRRs, having an offset δa between their centers, as shown schematically in Fig. 3.1. The copper rings are 3.75 mm in outer radius, 3.25 mm in inner radius, and have a gap width of 1 mm. These rings are printed on opposite sides of 1.6 mm thick FR4 circuit board. Each ring has a second gap of 0.4 mm opposite the initial gap, across which a Skyworks SMV1405-079 series varactor diode is soldered. A photo of one of the fabricated samples is shown in Fig. 3.2 (b). It can be seen that there is a second ring on the back of the board, shifted laterally. These

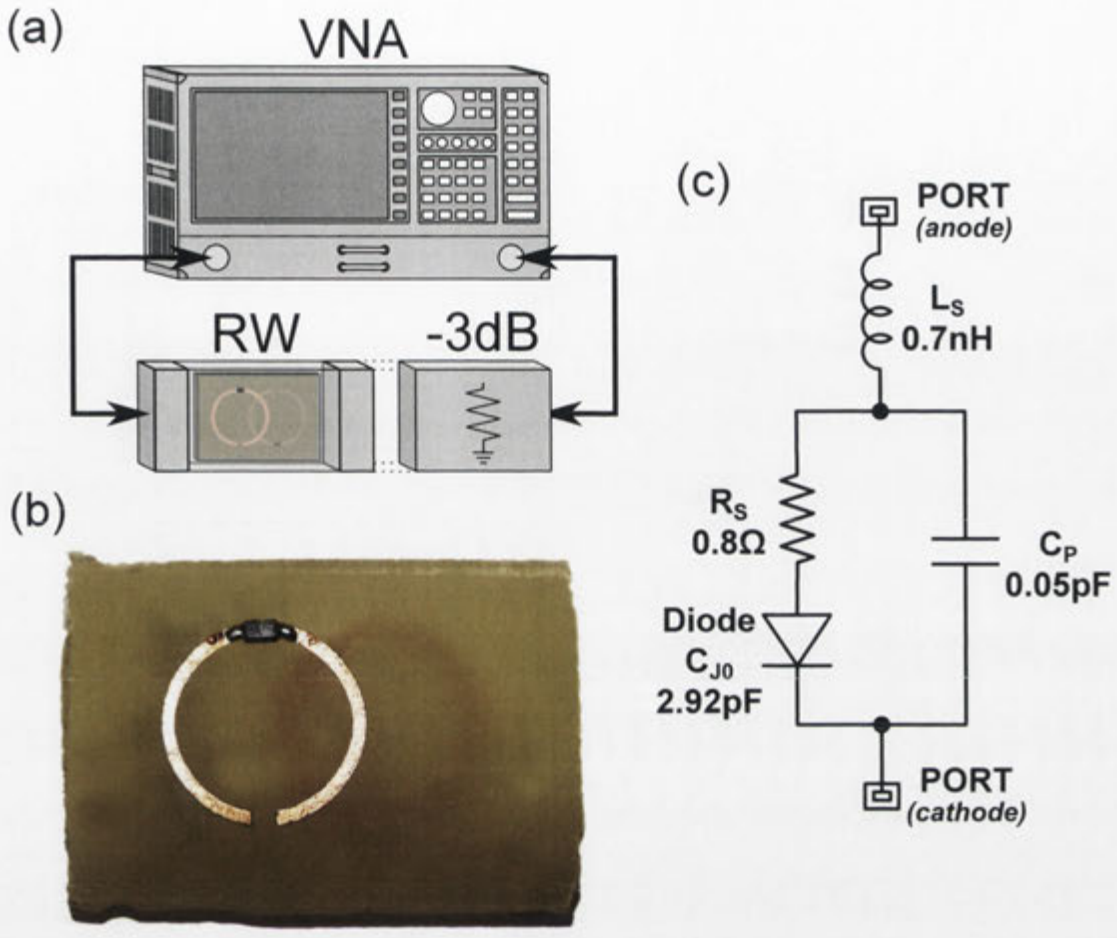

Figure 3.2: (a) Diagram of the experimental set-up. VNA is the vector network analyzer and RW is the rectangular waveguide. (b) A photo of one of the experimental samples. (c) A diagram of the RLC representation of the varactor diode, based on the SPICE model from the relevant data sheet [93].

samples are placed inside a WR-229 rectangular waveguide (RW), held up using a styrofoam holder, oriented such that the incoming magnetic field is perpendicular to the loops, as seen in Fig. 3.1.

3.1.1 Linear response

The transmission and reflection from the sample are measured using a Rohde and Schwarz ZVB-20 vector network analyzer (VNA) connected in series with the waveguide, shown in Fig. 3.2 (a). A 3 dB attenuator is added to the circuit to ensure that the VNA is operating in its linear regime. I measure the transmission and reflection coefficients, and use them to calculate the absorption spectrum, which describes the frequency of the maximum current distribution in the rings. This is given by $1 - |S_{21}|^2 - |S_{11}|^2$, where S_{21} and S_{11} are the transmission and reflection coefficients

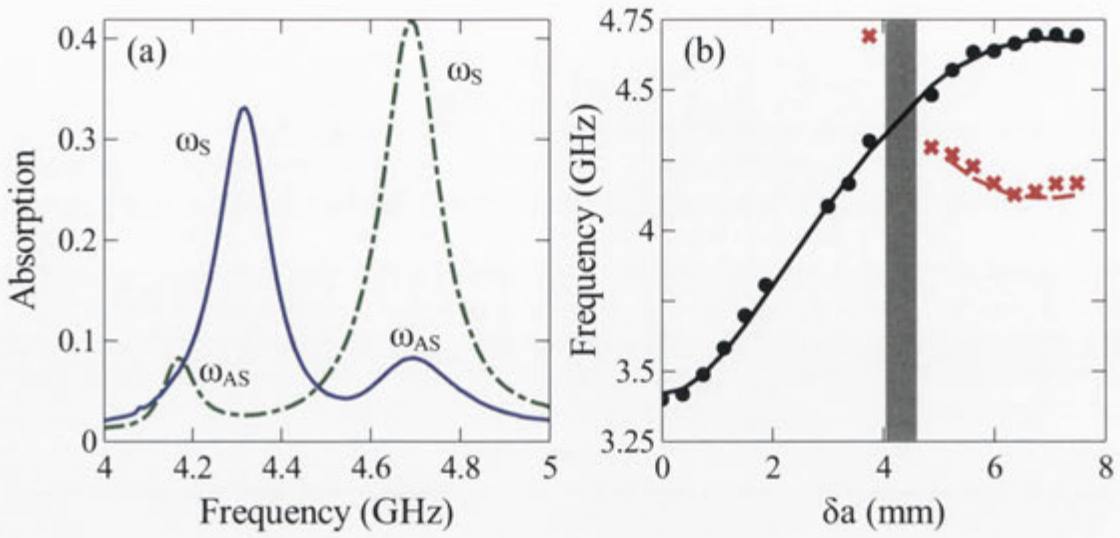

Figure 3.3: (a) The measured absorption curves for δa = 3.75 mm (blue solid) and 7.5 mm (green dashed), in the linear regime. Symmetric (ω_S) and antisymmetric (ω_{AS}) modes are highlighted. (b) ω_S (black circle/solid) and ω_{AS} (red cross/dashed), as determined both experimentally (markers) and numerically (lines) for the linear case.

respectively. The absorption curves are measured experimentally for the values of δa between 0 and 7.5 mm, in 0.375 mm increments, at -20 dBm power. This power is chosen as lowering the power further has no effect on the resulting measurements, and therefore is low enough to be considered the linear regime.

Numerical results are calculated for the linear regime using CST Microwave Studio. The rings are modeled as copper, and the FR4 board has a dielectric constant of 3.65, and a loss tangent of 0.025. Each varactor is represented by a series RLC circuit, shown in Fig. 3.2 (c), where C_{J0} is the zero bias junction capacitance, C_P is the package capacitance and R_S and L_S are the series resistance and inductance. For the SMV1405-079 varactor diode series used here, C_{J0} = 2.92 pF, C_P = 0.05 pF, R_S = 0.8 Ω and L_S = 0.7 nH [93]. For the purposes of modeling this varactor, the value of C_T = 2.67 pF is used, which is the measured total capacitance of the varactor, obtained from the data sheet [93]. This circuit describes the varactor diode in the linear regime so V_R =0 V.

The curves for δa equal to 3.75 mm, and 7.5 mm in the linear regime are plotted in Fig. 3.3 (a). There are clearly two resonant modes, symmetric (ω_S) and antisymmetric (ω_{AS}), which are defined by the relative directions of the currents on the rings. These modes are both tunable through a change of δa [75,76], which is evident, as when δa =3.75 mm ω_S (ω_{AS}) is the lower (higher) frequency, while when δa = 7.5 mm ω_S

(ω_{AS}) has increased (decreased) to become the higher (lower) frequency. Both ω_S and ω_{AS} are found and plotted as a function of δa in Fig. 3.3 (b) (markers), along with the numerical equivalents (lines). When they overlap, it is difficult to accurately distinguish them in the data. Therefore the experimental values for δa in the shaded regions have been excluded in all figures. Outside of this region there is excellent agreement between the experiment and numerical simulations, with negligible errors. Consistent with the findings in Ref. [76], there are strong responses in both the modes, with ω_S increasing with an increase in δa, and ω_{AS} decreasing.

As seen in Fig. 3.3 (a), the symmetric mode is much more strongly excited than the antisymmetric mode. In fact, the antisymmetric mode is not excited at all for low values of δa, as seen in Fig. 3.3 (b), due to weak coupling to the incident wave. However, there are enough points to see that this mode is still tunable via the lateral shifting. It is also important to note that the first two measurements for this mode are only experimental, as it was still unobservable in the numerics.

3.1.2 Nonlinear response

In a single SRR, the resonant frequency is determined by $\omega = 1/\sqrt{LC}$, where L is inductance, and C is capacitance. Introducing the varactor diode adds a nonlinear capacitance C_V in series with the capacitance of the SRR. By adding the second SRR, I introduce coupling between the rings, which causes a split in the resonant frequency, resulting in the two previously discussed modes, ω_S and ω_{AS}. Changing the intensity of the incoming microwaves causes a nonlinear change in the voltage incident on the varactors, which shifts the resonant frequencies by changing the effective capacitance of the system. This results in there being an added degree of freedom for manipulating the system.

In this structure the nonlinear response is quantified by a shift of the resonant frequency with increasing input power from the linear regime to 15 dBm, which is the maximum power available from the VNA. These powers represent the linear and high power regimes of the VNA. The inset in Fig. 3.4 shows the absorption for both powers when $\delta a = 3.75$ mm. It can be seen that both resonant modes are shifted by the change in power, the symmetric mode much more so. The arrow indicates the quantitative shift in resonance for increasing power.

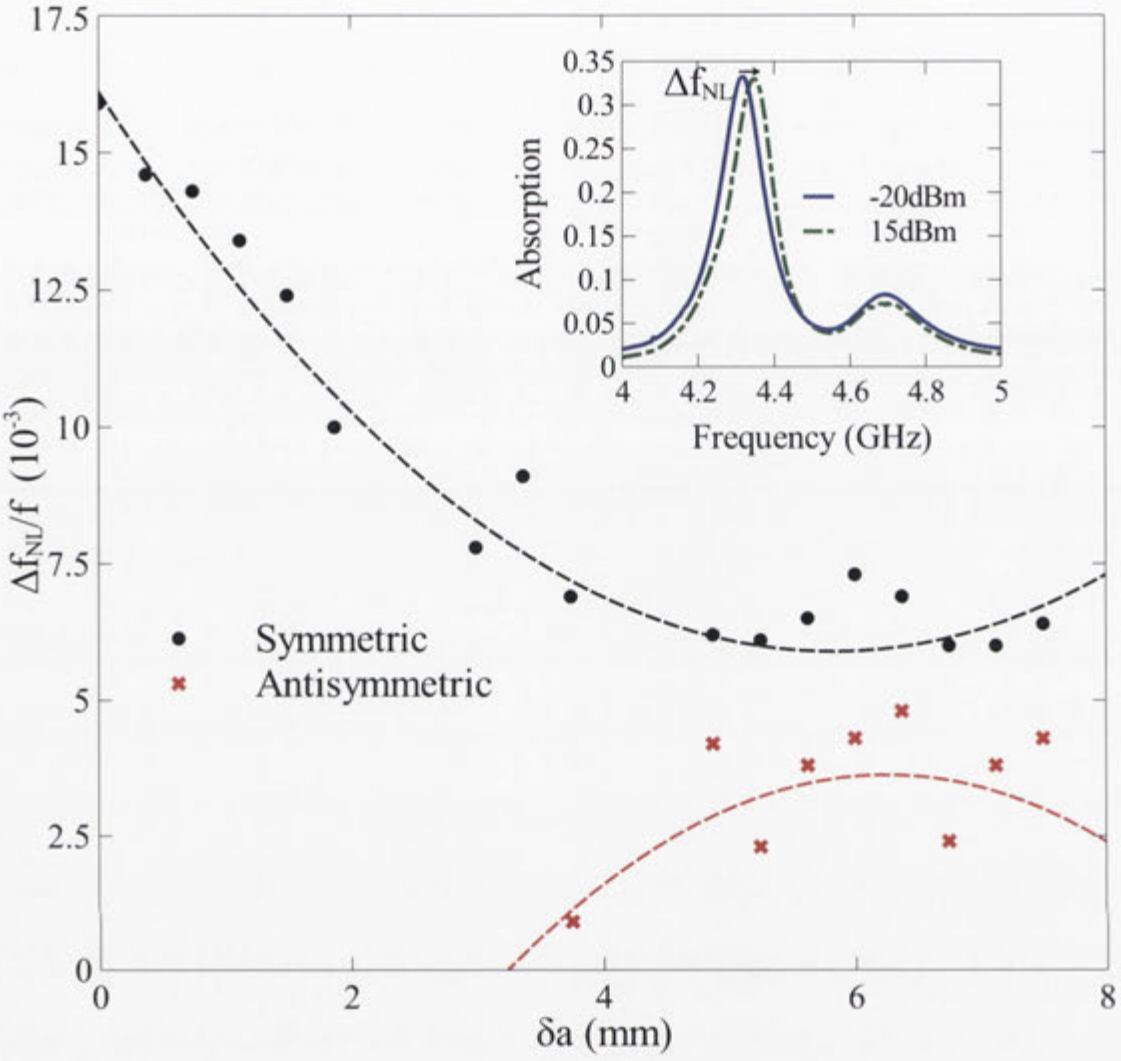

Figure 3.4: Relative nonlinear response for ω_S (black circles) and ω_{AS} (red crosses) for shifts (δa). The dashed lines are second order polynomial fits to the data. The inset shows the nonlinear shift of the absorption when $\delta a = 3.75\,\text{mm}$.

The relative difference between the low- and high-power resonant frequencies for each value of δa is shown in the main graph in Fig. 3.4. A significant change in the nonlinear frequency shift for both modes as a function of δa is observed. It is clear that the nonlinear shift for ω_S is much stronger when the rings are closer together. A trend for ω_{AS} cannot be meaningfully described due to the mode not being excited at lower offsets.

3.1.3 Breaking the symmetry

While the symmetric mode is the dominant excitation, being able to understand the antisymmetric resonance further would be an advantage. In order to do this, a stand made

Figure 3.5: Schematic of the SRRs inside the plexiglass stand.

of plexiglass is introduced to break the symmetry, which should enable the antisymmetric resonance to be excited. The symmetry is broken as the stand is physically closer to the gap of one of the resonators than the other, as shown in Fig. 3.5. The resulting absorption curves for shifts of 0.375 mm and 7.5 mm are then shown in Fig. 3.6 (a). It can be seen that the antisymmetric resonance is quite strongly excited, even for a shift close to 0 mm. This is due to a Fabry-Pérot resonance from the stand at around 5.2 GHz, as well as the breaking of the symmetry. The resulting dispersion relations for both modes are plotted in Fig. 3.6 (b). It can be seen that they are similar to those plotted in Fig. 3.3 (b), except that the antisymmetric mode is now excited for all values of δa.

While the plexiglass stand does break the symmetry, it does so only weakly, which can be seen from the similarity between the dispersion relations in Figs. 3.3 (b) and 3.6 (b). This means that while the symmetric and antisymmetric modes are not strictly symmetric and antisymmetric, they are close enough, meaning that the nonlinear properties of the antisymmetric mode at low offsets can now be measured.

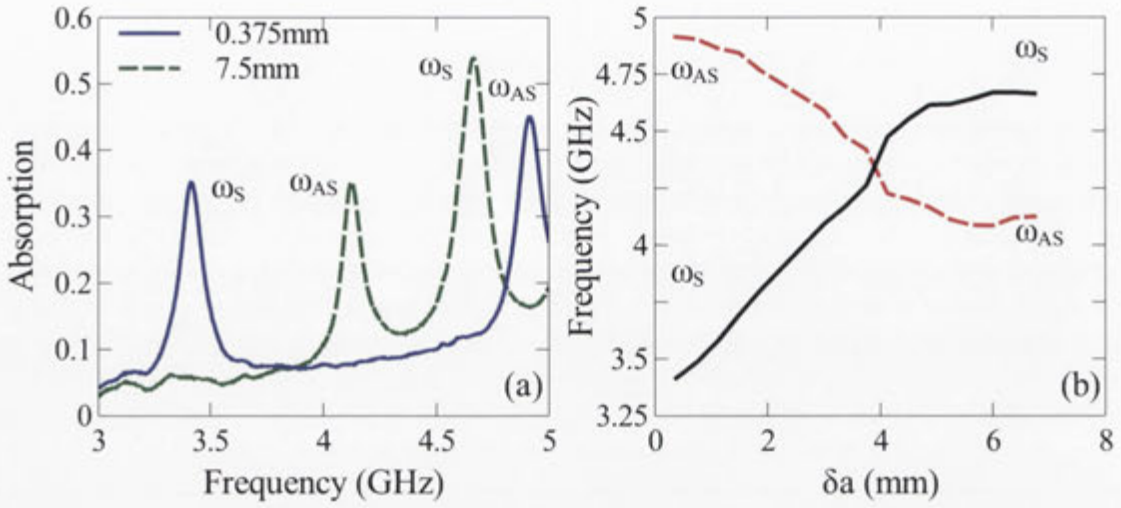

Figure 3.6: (a) Experimental absorption curves δa =0.375 mm and 7.5 mm. (b) Dispersion relation for both symmetric and antisymmetric modes.

Fig. 3.7 (a) shows the experimental absorption curves for a shift of 7.5 mm in both high and low power regimes. The nonlinear shifts for both modes are plotted as a function of δa in Fig. 3.7 (b). Again, this plot is similar to Fig. 3.4, however there are now values measured for the nonlinear response in the antisymmetric mode. While the nonlinear response for the symmetric mode remains quantitatively similar, the values measured for the antisymmetric mode in both cases are now much larger. It is also now possible to define a trend for the antisymmetric mode, where the nonlinear response is clearly increasing with offset.

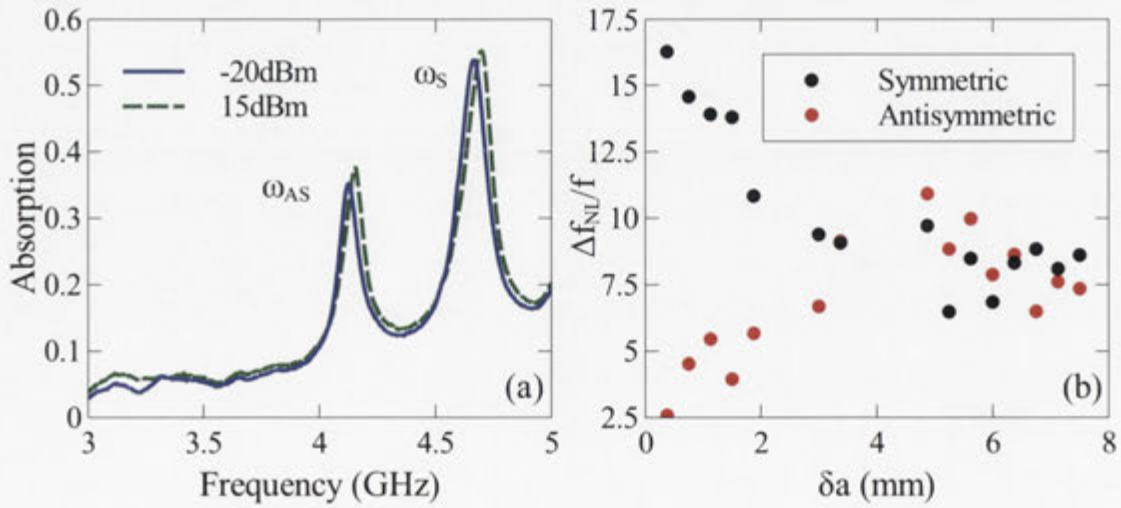

Figure 3.7: (a) Experimental absorption curves for an offset of δa = 7.5 mm at both low and high power. (b) Nonlinear shift as a function of δa for both resonant modes.

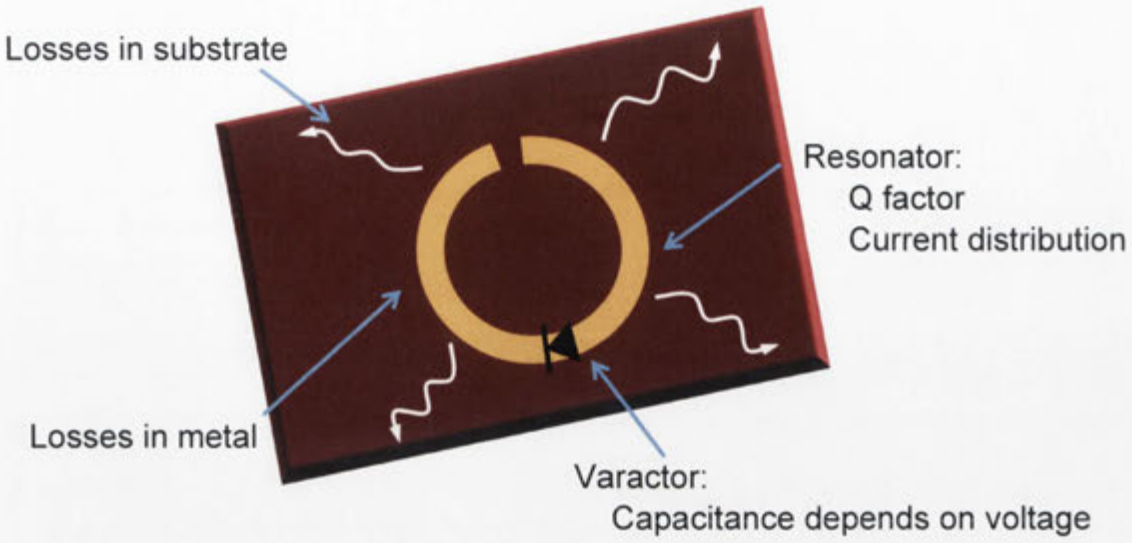

Figure 3.8: The main linear properties affecting the nonlinear response of the system. The white waves propagating away from the SRR represent the radiation.

As the symmetry breaking of the stand is increasing the excitation of the antisymmetric resonance, it is also possible that this is what is driving the increase in the nonlinear response for the antisymmetric mode.

While the use of the plexiglass stand has been useful in studying the antisymmetric mode further, the results using the foam are more useful as there is no interference from the Fabry-Pérot resonances.

3.2 Factors contributing to the nonlinear response

The nonlinear tuning can be explained by looking both experimentally and numerically at some of the linear aspects of the system, which are shown in Fig. 3.8. In particular, the losses in the system, along with the properties of the varactor diode, and the current distributions on the rings should be significant in determining the response. In this section, I specifically look at the effect of the currents on the rings via the absorption peaks, as well as the quality (Q) factor. I study both of these for the lossy and lossless cases to also examine the effect of the substrate losses. I then look at the properties of the varactors by calculating the voltage and capacitance across them.

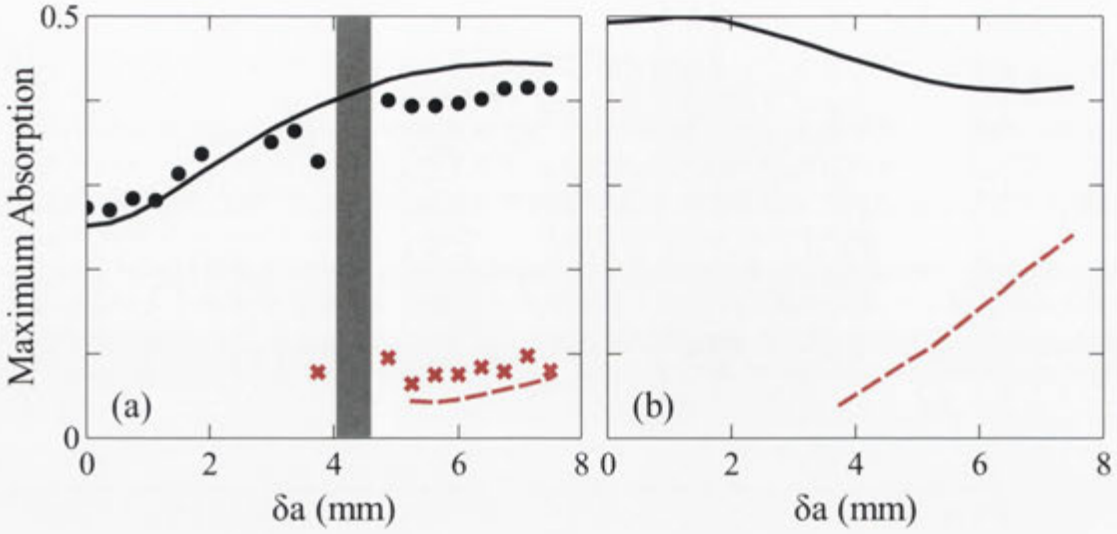

Figure 3.9: (a) Experimental (markers) and numerical (lines) maximum absorptions for both symmetric (black circle/solid) and antisymmetric (red cross/dashed) modes. (b) Numerically calculated absorption coefficients at the resonant frequencies for the case of a lossless substrate.

3.2.1 Absorption

As the nonlinear shift is due to the currents excited in the rings (which also lead to absorption), it would be expected that the higher the absorption, the larger the nonlinear response. Therefore the maximum absorption for each value of δa is plotted in Fig. 3.9 (a) for both modes, showing good agreement between experimental and numerical results. However, by comparing this figure with Fig. 3.4, for the symmetric mode it can be seen that the *absorption increases* with *decreasing nonlinear shift*. This effect appears because by offsetting the rings not only are the current amplitudes in the rings modified, but the field distribution in the substrate is also changed. As a result, the total absorption presented in Fig. 3.9 (a) contains contribution from losses in both metal and dielectric. At the same time, the nonlinear response is caused by currents in the metal which flow through the varactor. The losses within the FR4 substrate increase with δa due to increased field confinement within the board, and changes in these losses dominate changes of the absorption in the metal. In Fig. 3.9 (b) the results of a simulation which neglects dielectric losses are shown. It can be seen that there is now agreement with the trend in the nonlinear response. The difference in trends between Figs. 3.9 (a) and (b) confirms the influence of the dielectric losses.

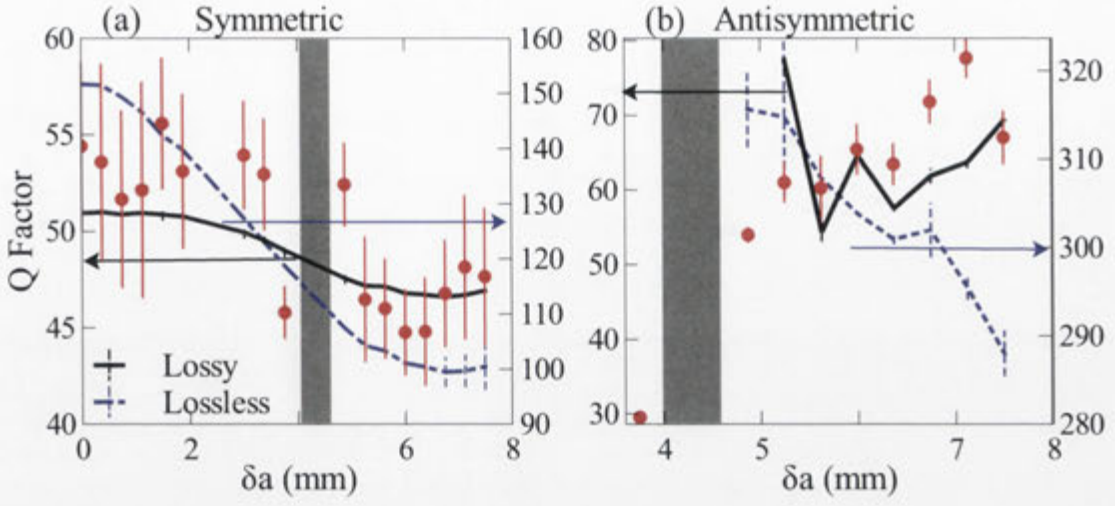

Figure 3.10: Experimental (markers) and numerical (lines) Q factors for the (a) symmetric mode, and (b) antisymmetric mode. The black (solid) lines correspond to the lossy case, while the blue (broken) lines correspond to the lossless case. The arrows indicate the relevant axis, and the error bars are plotted for all cases. The experimental results use the same axis as the lossy case.

3.2.2 Quality factor

The quality (or Q) factor describes the rate of energy loss relative to the energy stored in the system. The amplitude of the currents depends on the Q factor of the resonator, so it would be expected that there would be some correlation between the changing nonlinear shift, and the Q factor. The Q factor is calculated as $\pi f/2\gamma$, where f is the resonant frequency, and γ is found from fitting the peaks with a Fano function [88]. This approach was used as the antisymmetric resonances are too small to find an accurate width.

In Fig. 3.10, I have plotted the Q factor as a function of δa for both modes. The solid lines for the symmetric and antisymmetric modes are the Q factors for the numerical lossy case. This case corresponds to the experimental results shown by the red markers. The error bars are also shown for all cases. While the general trends agree between the experiment and numerics, there is less agreement between the values, even considering the error bars. This is not entirely surprising as the error bars only represent the fitting and analysis errors, and not any fabrication imperfections. These error bars are dominated by the residual errors from the fitting function. While the fabrication imperfections are not huge (they are the main source of disagreement in Fig. 3.3), they accumulate when calculating the Q factor. The jump in the numerical results for the antisymmetric resonance is probably due to the peak not being distinguishable enough

from the symmetric peak to define a width accurately.

By comparing Fig. 3.10 with Fig. 3.4 it can be seen that there is a direct correlation between the Q factor and the nonlinear shift, due to the change in dielectric losses. The additional finely dashed curves show the case when dielectric losses are neglected. This indicates that for both modes radiation losses increase with increasing offset, due to increased coupling to the waveguide modes. For the symmetric mode, radiation losses are dominant, thus increasing them decreases the current amplitude and hence the nonlinear shift. However for the anti-symmetric mode, the coupling is initially very low, and for low offsets very little energy can accumulate in the resonant mode. Therefore increasing the coupling increases the current amplitude and the nonlinear shift.

3.2.3 Voltage and capacitance

The physics of the nonlinear shift of the resonant frequency was studied in Ref. [65], where it was shown that the rectified AC voltage across the varactor provides a self-biasing mechanism. By increasing the amplitude of the electromagnetic wave, alternating voltages in the SRR are increased, generating a larger DC bias voltage, reducing the varactor capacitance. To study this effect I perform numerical simulations in the linear regime, and monitor the voltages on each RLC circuit representing a varactor. As a larger voltage leads to a stronger decrease in the varactor capacitance, a similar trend would be expected between the voltages recorded at the resonant frequency, and the nonlinear shift. It should be noted that the voltage across the capacitor, and not the whole RLC circuit, should be calculated, which is done by numerically monitoring the voltage over the varactor diode, then calculating the portion over the capacitor and resistor. This is done because the inductance represents the purely linear package inductance. As CST treats the RLC circuit as a lumped element, only the voltage across the entire circuit, and not one component, can be monitored.

By rectifying the monitored RF voltage V_{RF}, the DC voltage can be calculated [65]:

$$V_R = -V_T \ln \left[I_0 \left(V_{RF}/V_T \right) \right], \tag{3.1}$$

where $V_T = 25.85\,\mathrm{mV}$ is the thermal voltage and I_0 is a modified Bessel function of the first kind. The resulting DC voltage at the resonant frequency is plotted for both

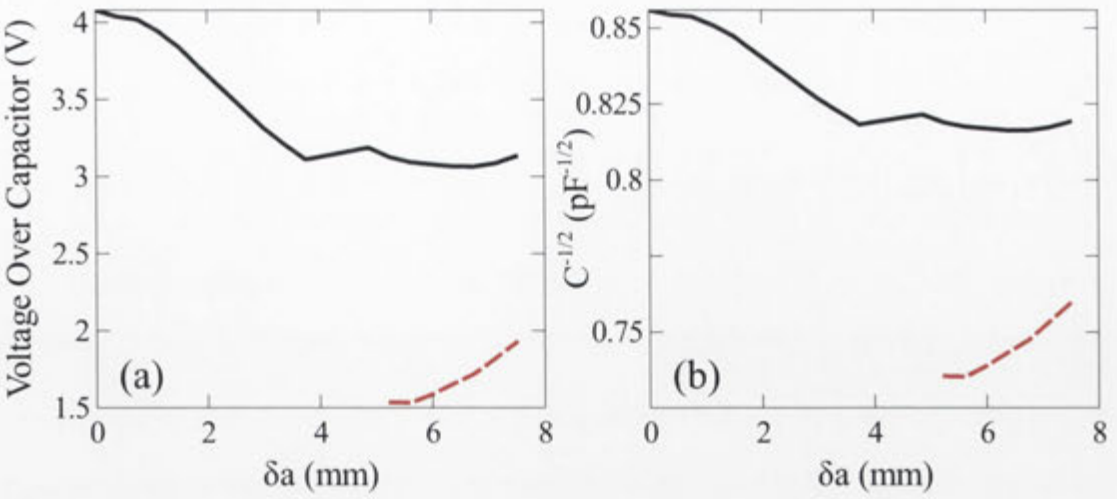

Figure 3.11: (a) Calculated voltage over the capacitive component of the varactor. (b) Resulting capacitance (presented as $1/\sqrt{C}$).

resonant modes in Fig. 3.11(a).

By comparing Figs. 3.4, 3.9 (b), and 3.11 (a), an overall correlation can be seen, where as δa increases there is a decreasing trend in the nonlinear response, the maximum absorption in the rings, and the calculated voltages, for the symmetric mode. This enables the nonlinear response of the system to be explained in a meaningful way.

As the nonlinear response should be directly proportional to the inverse of the square root of the capacitance, the change in capacitance to the system with increased power is then calculated using the known voltage across the varactor. From the data sheets for the varactor, the capacitance (C_V) can be obtained for a given applied voltage (V_R) using the equation [94]

$$C_V = \frac{C_{J0}}{(1 + V_R/V_J)^M} + C_P, \tag{3.2}$$

where V_J is the junction potential and M is the grading coefficient. For the SMV1405-079 varactor diode series I have used, these values are $C_{J0} = 2.92\,\text{pF}$, $V_J = 0.68\,\text{V}$, $M = 0.41$, and $C_P = 0.05\,\text{pF}$ [93].

The inverse of the square root of the resulting capacitance is shown in Fig. 3.11 (b), as a function of δa. As expected, this plot closely resembles the plots in Fig. 3.11 (a) and Fig. 3.4. The dependence of the varactor capacitance on δa also changes the response

of the system to linear tuning of the resonant frequencies, as the resonant frequency is dependent on the combined capacitance of the varactor and SRR.

3.3 Conclusion

In this chapter I have shown that the near-field interaction can be used to control the nonlinear properties. I then studied the effect of the linear properties on the nonlinear response.

I experimentally demonstrated that by shifting two coupled SRRs relative to each other, I can significantly control the nonlinear properties of both the symmetric and antisymmetric resonant modes in the system. The symmetric and antisymmetric modes were found to respond to both the incident wave and the change in coupling. While the antisymmetric resonance is not normally strongly excited, it can be boosted by breaking the symmetry, which causes the antisymmetric mode to be excited for all offsets. It also increased the nonlinear response of the antisymmetric resonance.

I also found that the tuning of the nonlinear response can be explained and predicted by studying the linear properties of the system. This includes the maximum absorption on the rings, and the voltages across the varactors. As a result, it was found that the losses in the system also play a strong part in the tuning of the nonlinear response. These results should stimulate further work in controlling and designing nonlinear properties of metamaterials.

Chapter 4

Dispersionless Optical Activity in Chiral Metamaterials

Being able to control the output polarization state from a chiral metamaterial is desirable in the engineering of materials, as doing so is important for many applications such as ultrafast modulation of electromagnetic waves [95]. In particular, the development of a planar chiral metamaterial with strong broadband optical activity over the transmission band would be advantageous. The strong coupling between neighboring resonators should be helpful in achieving this effect.

Coupling a resonator to its complement should provide a means of achieving unique chiral properties. Babinet's principle states that an infinitely thin, perfectly conducting complementary structure illuminated by an incident field rotated through 90° to the field exciting the structure, generates a magnetic field equivalent to the electric field excited in the original structure [52, 96–98]. Intuitively, by coupling an element together with its complement these electric and magnetic responses become coupled, matching the impedance over the transmission peak, which should overcome the highly dispersive optical activity, and ellipticity often seen in rotated chiral structures, as discussed in Section 1.1.3.

This approach has been used to achieve dual-band ultraslow modes, by alternating layers of SRRs and their complementary structures [99]. It has also been used to create a broad bandpass filter in the terahertz regime, combining a cross and a cross shaped hole of different size in a non-chiral arrangement, for which the current distributions for the resonant modes were also studied [100]. Chiral properties of such structures have not been studied.

Figure 4.1: Schematic of my proposed "mixed pair": a cross coupled to its complement, rotated through an angle θ.

In this chapter I propose a cross coupled to its complement, or a "mixed pair", and demonstrate that it achieves large, flat optical activity accompanied by very low ellipticity. In Section 4.1 I compare the mixed pair to a pair of crosses and a pair of complementary crosses, and find that this structure provides dispersionless optical activity over the transmission resonance, in contrast to the high dispersion normally seen. This results in very low ellipticity in the output polarization state. Section 4.2 then describes how I optimize the chirality through the twist angle, and study the effect of changing the spacing between elements. The case of multiple complementary pairs is also briefly studied. In Section 4.3 I investigate the effect of increasing the substrate losses. The large, flat optical activity and low ellipticity are then confirmed experimentally. Section 4.4 then looks at the case of a strip combined with a slot to determine the excitation mechanism of this structure. It is found that this structure is excited by means of the hole-modes in the complementary cross. Finally, in Section 4.5 I summarize this chapter, and provide some directions for future research.

4.1 "Mixed pair"

The cross and its complement are designed having arms of length 25 mm, and width 1.5 mm. They are rotated through 22.5°, and separated by FR4 substrate 1.6 mm thick, with 1.6 mm substrate on the outside of both the cross and complementary cross (so that the resonators have substrate on either side). They are modeled as perfect electrical

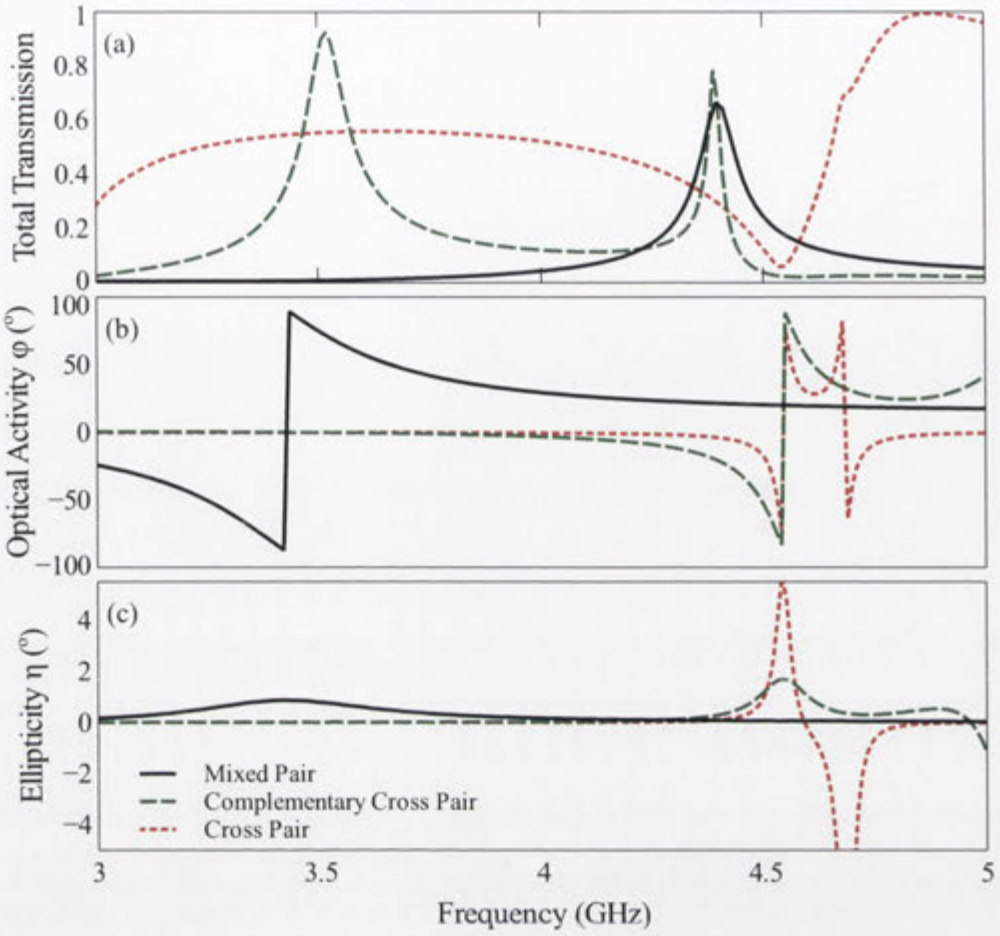

Figure 4.2: (a) Transmission, (b) optical activity and (c) ellipticity for a pair of crosses (red dotted line), a pair of complementary crosses (green dashed line) and the mixed pair (solid black line).

conductors (PEC), inside a circular waveguide with a diameter of 59.7 mm , so as to be experimentally realizable. The substrate has a dielectric constant 4.3 and loss tangent of 2.5×10^{-4}. A schematic of the two elements rotated through an angle θ is shown in Fig. 4.1.

Simulations are calculated using CST Microwave Studio. I excite the two lowest order modes using a linearly polarized input wave. The first mode is assigned to that with the electric field oriented in the x-direction, and the second for the y-direction. I simulate the co- and cross-polarized transmission coefficients for both linear polarizations (S_{xx}, S_{yy}, S_{xy} and S_{yx}). As this structure has four-fold rotational symmetry, $S_{xx} = S_{yy}$ and $S_{xy} = -S_{yx}$. The total transmission amplitude $(S_{xx}^2 + S_{xy}^2)^{1/2}$ is plotted in Fig. 4.2 (a) (solid black curve).

The transmission coefficients for the circular polarizations are found as

$$T^{\pm} = \frac{((S_{xx} + S_{yy}) \pm i(S_{xy} - S_{yx}))}{2}, \tag{4.1}$$

from which the optical activity is then calculated using Eq. (1.10). This is plotted in Fig. 4.2 (b) (solid black curve). The corresponding ellipticity of the output polarization state, defined in Fig. 1.4 (b), is shown in Fig. 4.2 (c) (solid black curve), which is calculated using Eq. (1.11).

To show the advantages of the "mixed pair" compared with known structures, I calculate the optical activity and ellipticity for a pair of crosses, and a pair of complementary crosses, both also with an internal rotation of $\theta = 22.5°$. The lengths of the elements in these structures were designed so that the transmission resonances line up with those of the mixed structure - (24 mm) 16 mm for the (complementary) crosses [Figs 4.2 (a, b)].

In Fig. 4.2 (a) there is a resonant pass band for the mixed structure at 4.4 GHz. There is also a transmission minimum at 3.4 GHz, which cannot be seen in this plot as the background transmission is already low. For the pair of crosses, there is a resonant stop band at 4.6 GHz. By reducing the distance between the two crosses, thus increasing the coupling, it is seen that there are actually two resonances very close together. The pair of complementary crosses also has two resonances - pass bands at 3.5 and 4.4 GHz. The mixed structure has at least one other resonance below the cut-off frequency of the waveguide, however the pass band at 4.4 GHz is the most useful resonance, as it is a pass band accompanied by large optical activity.

The optical activities for the three structures are compared in Fig. 4.2 (b), as calculated using Eq. (1.10). For both the pair of crosses and pair of complementary crosses there is highly dispersive optical activity at the resonant transmission band. For the mixed structure, there is a resonance in the optical activity at 3.4 GHz. This resonance corresponds to the transmission minimum, where the through transmission dips below the cross-polarized transmission. However, the optical activity at the pass band frequency has very low dispersion, but is still large (about 20°).

The corresponding ellipticities, calculated using Eq. (1.11), are shown in Fig. 4.2 (c). The ellipticity is related to the gradient of the optical activity shown in Fig. 4.2 (b), due to

the Kramers-Kronig relationship for the chirality κ, as mentioned in Section 1.1.3. This means that, unlike the other two structures, the mixed structure has very low ellipticity at resonance, which is very desirable. It also shows much lower ellipticity overall than the other structures.

4.2 Optimizing the response

4.2.1 Twist angle

As the system is achiral when $\theta = 0°$ and 45°, but chiral for all angles in between, I investigate the control of the chirality by varying the twist angle θ. I measure the transmission for θ ranging from 0° to 45°, in 2.5° increments. In Fig. 4.3 (a) the total transmission is plotted for some of these angles. It can be seen that as θ is increased from 0° to 45°, the resonant frequency increases from 4.056 GHz to 4.514 GHz, and the transmission amplitude changes slightly, with an overall moderate effect of θ on the transmission. Fig. 4.3 (b) shows the optical activity at the resonant frequency, as a function of twist angle θ. The near-field coupling within a twisted "mixed pair" leads to changing optical activity due to change in the coupling between the two elements. While this structure is furthest from symmetry when $\theta = 22.5°$, the maximum optical activity of $\phi = 22°$ is found at θ =17.5°. This is due to retardation, which is related to the spacing between the resonators, as found in Ref. [101]. This spacing can be seen as adding helicity to the system. The resonant behavior at 3.5 GHz, associated with the stop-band resonance in the transmission, is present for most values of θ, and is less tunable. The ellipticity at

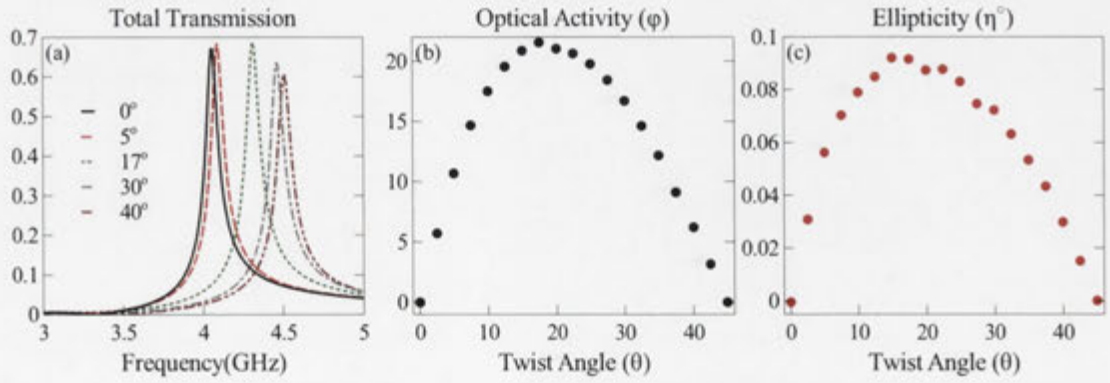

Figure 4.3: (a) Total transmission for various twist angles θ, ranging from 0°(solid black) to 40°(dashed brown); and (b) optical activity and (c) ellipticity as a function of twist angle, calculated at the frequency of maximum transmission for that angle.

resonance was also calculated, and is plotted in Fig. 4.3 (c), showing a similar trend to the optical activity. The ellipticity at resonance peaks at 0.1°, which is very low compared to other twisted chiral structures including that in Ref. [47], where the ellipticity angle η reached values of 45° over the transmission resonance.

4.2.2 Separation between elements

By changing the distance between the cross and its complement, I change the retardation in the structure, as well as the interaction between the resonators. This should also alter the twist angle at which the optical activity and ellipticity peak, as shown in Fig. 4.3 (b, c). From Fig. 4.4 (a) it is seen that increasing the spacing between the elements from 1 mm (solid black line) to 2.5 mm (dotted green line) significantly reduces the magnitude of the transmission. More importantly, the transmission resonance shifts closer to the optical activity resonance, increasing the ellipticity of the structure across the transmission band, shown in Fig. 4.4 (c). However, there is also a decrease in the magnitude of the optical activity as the spacing is decreased, seen in Fig. 4.4 (b). Therefore it can be concluded that there is a trade-off between the magnitudes of the transmission and optical activity in choosing the optimal spacing.

4.2.3 Multiple pairs

While the flat optical activity is a reasonably broadband effect, the transmission pass band is quite narrow. By combining multiple resonators in a longitudinal array, an increased number of resonances are excited. These resonances could potentially be engineered to merge and form a continuous broadband resonance [48, 100, 102]. Increas-

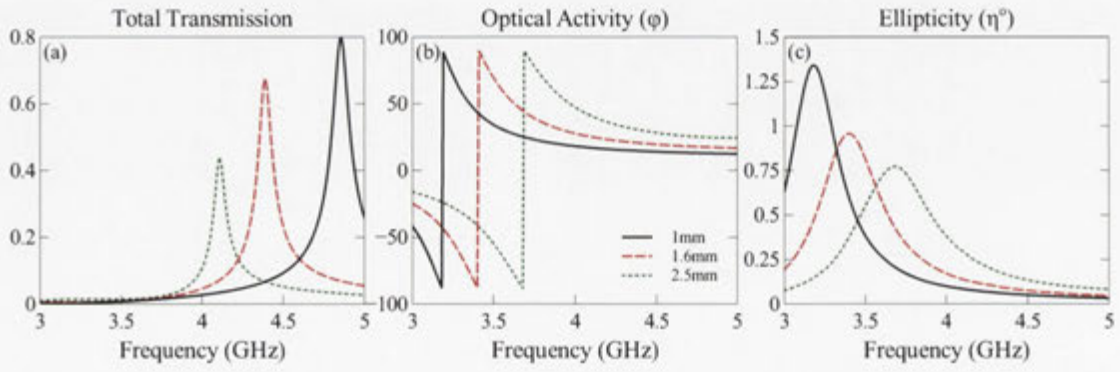

Figure 4.4: (a) Total transmission, (b) optical activity and (c) ellipticity for substrate thickness varying from 1 mm (solid black) to 2.5 mm (dotted green).

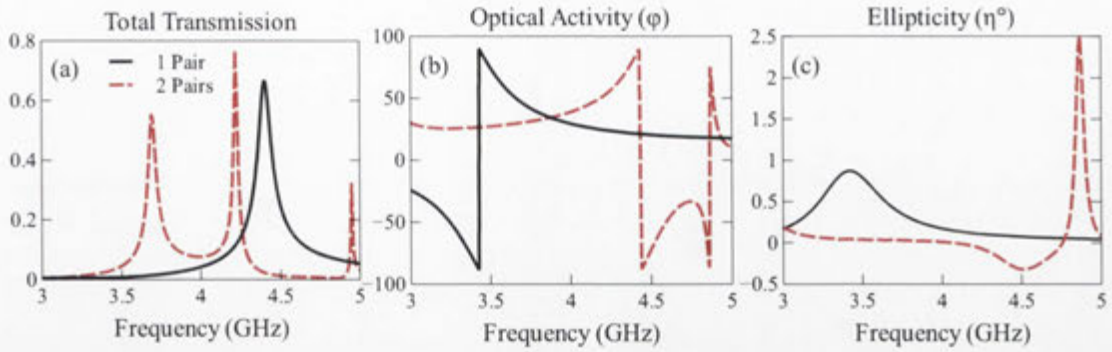

Figure 4.5: Comparison of the (a) total transmission, (b) optical activity and (c) ellipticity for one (solid black) and two (dashed red) pairs.

ing the number of pairs along the z-axis should allow the increase of the transmission bandwidth and increase the total optical activity. Such a system will also provide further degrees of freedom to control the size of the optical activity through the tuning of the rotation angles.

I simulate two mixed pairs, with alternating crosses and complementary crosses, where all resonators are equidistant with 1.5 mm spacing, and rotated 22.5° relative to the previous element. The parameters have been chosen to optimize the occurrence of flat optical activity over a transmission pass band, resulting in the cross arms now being 30 mm long. The resulting total transmission is plotted in Fig. 4.5 (a), compared to my previous results for one pair. There are three pass bands over this frequency range, at around 3.7 GHz, 4.2 GHz and 4.9 GHz, however there are further resonances outside this range. There is also a transmission minimum visible near 4.8 GHz. The resonances are also more narrowband when there are two pairs.

The optical activity is plotted in Fig. 4.5 (b), and by comparing it to Fig. 4.5 (a), it can be seen that the optical activity is large and flat over the first transmission resonance (3.7 GHz). The optical activity at this point is also larger than that for the single pair ($\sim 30°$). It is also seen that at the second resonance (4.2 GHz), the optical activity is still relatively flat, and much larger than at the first resonance ($\sim 50°$). There is a trade-off here between the magnitude of the optical activity and the slope. The optical activity is highly dispersive over the third resonance.

I have also plotted the ellipticity in Fig. 4.5 (c). While the total ellipticity is larger for two pairs, the ellipticity at resonance is still very low over the first two resonances.

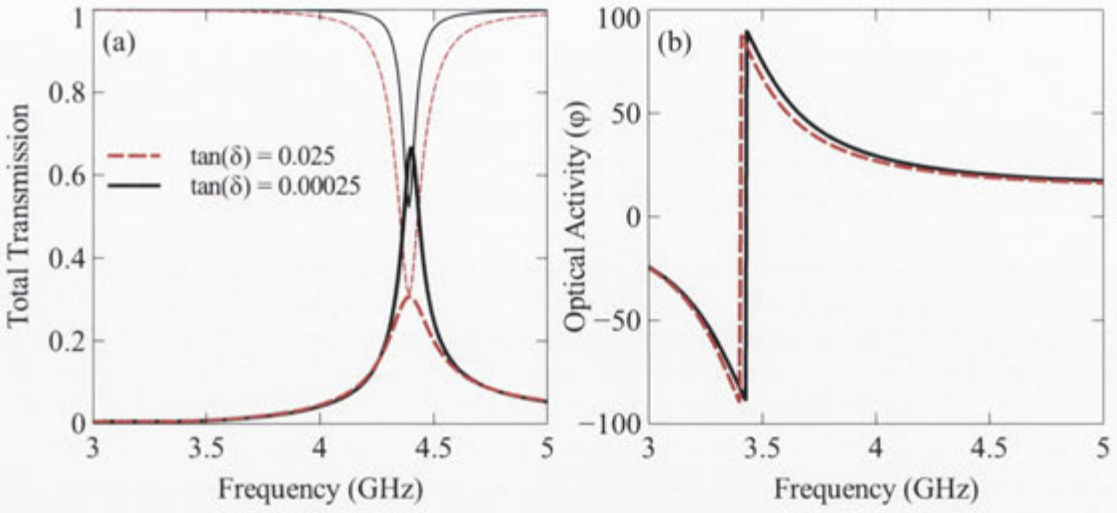

Figure 4.6: (a) Total transmission (thicker lines) and reflection (thinner lines); and (b) optical activity for a mixed pair, compared for increasing losses.

However, it can be seen that the bandwidth over which there is very low ellipticity is smaller for two pairs than for one.

While increasing the number of pairs has increased the magnitude of the optical activity over transmission resonance, the transmission is actually less broadband. However, the flat optical activity now spans two transmission resonances, and it may be possible to drive the resonances closer together through increasing the number of mixed pairs. However, the increase in the number of resonances makes the system very complicated to find an optimal regime, which could be improved by the introduction of a suitable model to predict the behavior of the system.

4.3 Experimental verification

4.3.1 Increasing losses

So far my simulations have assumed the best case losses in the system. However, it would be useful to be able to experimentally verify my findings, which will involve higher losses if the FR4 substrate is used. I investigate this by increasing the losses in the substrate by two orders of magnitude.

Fig. 4.6 (a) shows the magnitude of the total transmission (thicker lines) and reflection as the losses in the system are increased. It is not surprising that as the losses are increased the magnitude of the transmission decreases significantly. It is evident from

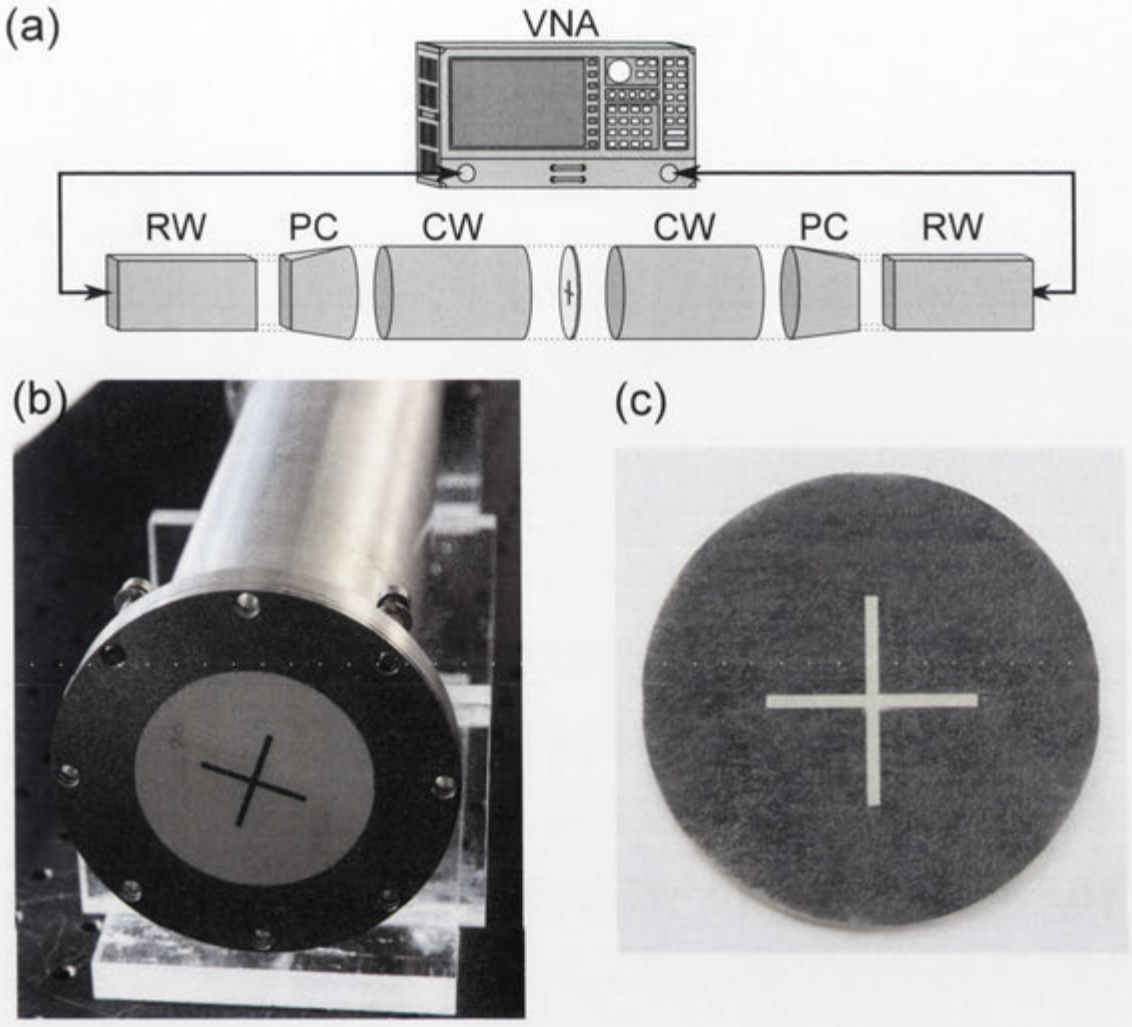

Figure 4.7: (a) Schematic of the experimental set-up. VNA stands for vector network analyzer, RW rectangular waveguide, CW circular waveguide and PC polarization converter. (b) Photo of the sample inside the circular waveguide rotated through 20° and (c) the other side of the sample, showing the complementary cross.

the accompanying drop in the reflection, that this due to an increase in the absorption. However, Fig. 4.6 (b) shows that the optical activity is barely affected by the increase in losses. The ellipticity was also studied (not shown) and it increases slightly at resonance with increased losses, but is still very low. This means that good experimental results should be able to be obtained, regardless of the losses. It also suggests that scaling this structure down for use at optical frequencies with much higher losses could be feasible.

4.3.2 Measurement of the sample

The experiment is conducted using a vector network analyzer (VNA) connected to a series of waveguides, shown in Fig. 4.7 (a). The rectangular waveguide (RW), the same

waveguide used in Chapters 2and 3, allows the propagation of one waveguide mode, which is linearly polarized. This mode is then converted into a right- or left-handed circularly polarized wave using the polarization converter (PC). The wave then propagates through the circular waveguide (CW), inside which the sample is placed. The second polarization converter converts the resulting wave back to a linear polarization, which is then measured by the VNA. Using this set-up I measure the transmission coefficients for both right- and left-handed polarizations.

While the losses may not affect the optical activity and ellipticity, for applications it is usually desirable to have larger transmission, so I use Rogers R4350 board as the substrate, which has a loss coefficient of 0.0031 at 2.5 GHz, and a dielectric constant of 3.48. To accommodate the change in substrate, the cross and its complement now have arms of length 27 mm, and width 1.5 mm. They are made of copper, and are 30 μm thick. They are separated by the 1.5 mm thick substrate, and rotated through 20°. The cross and complementary cross are printed on opposing sides of the same substrate, and a separate substrate is fabricated for each angle. Fig. 4.7 (b) shows the sample inside the circular waveguide. The color of the cross is due to a thin coating of solder to prevent oxidization. The reverse side of the substrate is shown in Fig. 4.7 (c).

The simulations are adjusted to best match the experimental parameters. The magnitudes of the right- and left-handed polarizations are compared with the experimental results in Fig. 4.8 (a). It is seen that there is little difference between the two polarizations, however the resonances are blue-shifted in the experiment, which is most likely due to increased effective series capacitance form an imperfect electrical connection between the metallic sample and the waveguide walls. This is the result of a thin gap between the complementary cross and the edge of the sample, and the samples not being perfectly round. The phase for both polarizations is also plotted in Fig. 4.8 (b), and there is good agreement apart from the shift in resonance. The cross-polarization was also measured, and found to be small, confirming the reliability of the measured circular polarizations.

The optical activity and ellipticity are again calculated using Eqs. (1.10) and (1.11). Figure 4.9 (a) shows the calculated optical activity, comparing the experiment with the numerical simulations. It can be seen that there is good agreement, with large, flat op-

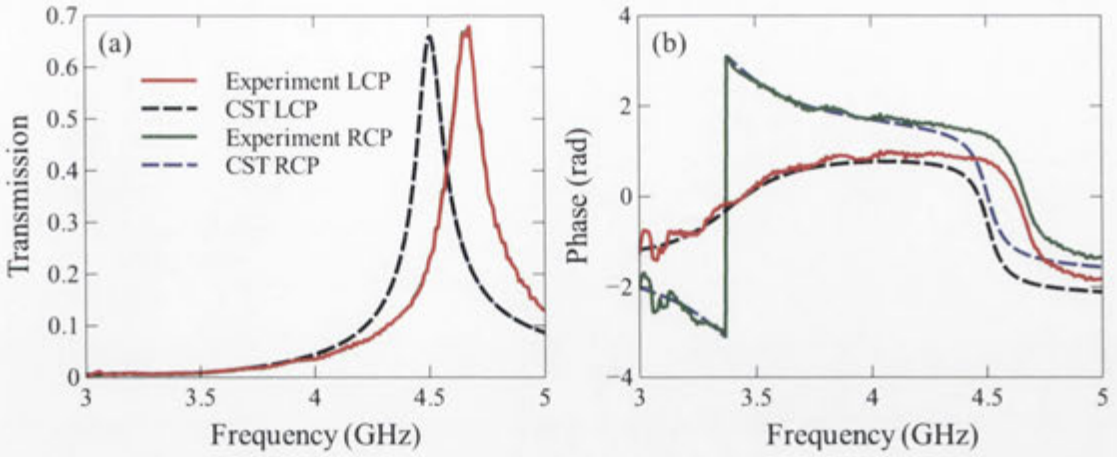

Figure 4.8: (a) Magnitude and (b) phase of the transmission for both LCP and RCP waves, experimental (solid) and numerical (dashed), for the structure rotated through 20°.

tical activity over the frequency of transmission. The ellipticity is plotted in Fig. 4.9 (b), noting that the magnitude of the ellipticity is very small, as intended with this design, so the measured values are comparable to the experimental uncertainties.

4.3.3 Twist angle

The effect of changing the twist angle θ is also experimentally verified. This is measured in 2.5° steps. The resulting optical activity at the transmission resonance is plotted as a function of θ in Fig. 4.9 (c), both numerically and experimentally. The numerical data is interpolated using a fourth-order polynomial. The small disagreements between the numerical and experimental data points can be explained by imperfections in the fabrication.

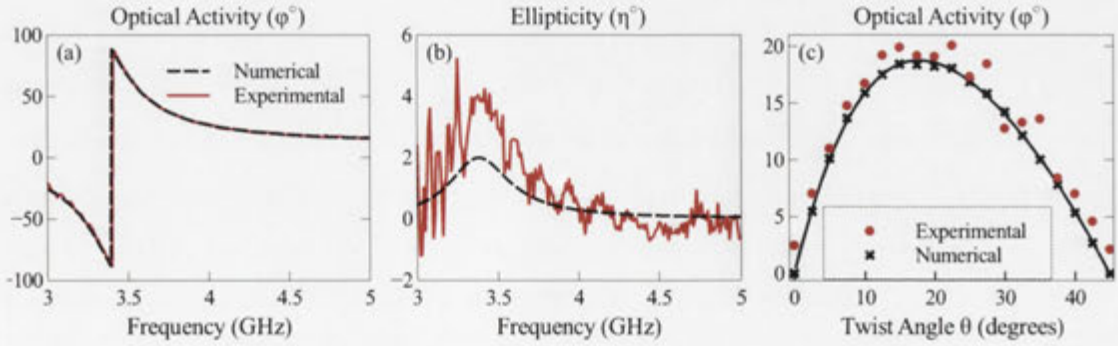

Figure 4.9: (a) Optical activity for both numerical simulations and experiment, when $\theta = 20°$. (b) Experimental and numerical ellipticity, for $\theta = 20°$. (c) Experimentally measured and numerically calculated optical activity at the transmission resonance, as a function of the twisting angle θ. The numerical values (black) are fitted using a fourth- order polynomial.

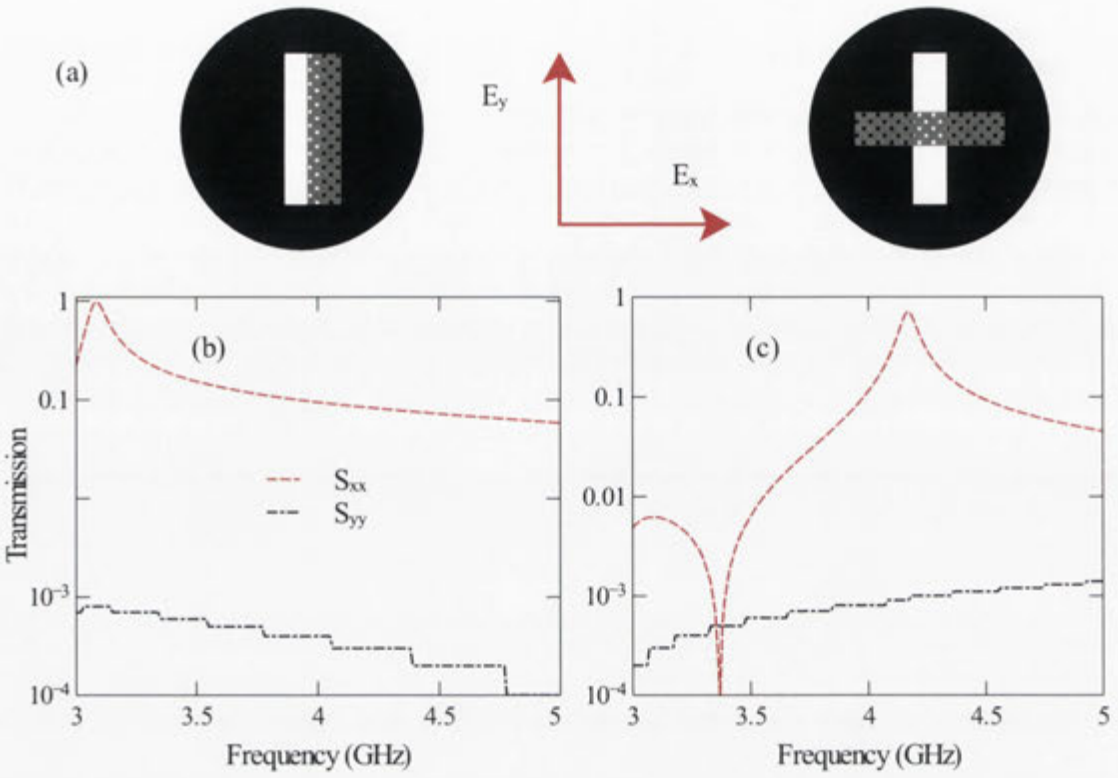

Figure 4.10: (a) Basic schematics of the strip, and slot, in parallel, and perpendicular arrangements. The slot is aligned with the y-axis, the strip is rotated. The gray, hatched rectangle is the strip and the black, solid outline is the slot. The simulated transmissions for both modes, S_{xx} (red dashed) and S_{yy} (black dotted), are shown in (b) (parallel) and (c) (perpendicular).

These experimental results verify my numerical findings presented in Section 4.1 of large, dispersionless optical activity at resonance, and very low ellipticity.

4.4 Excitation mechanism

In order to determine the nature of the transmission resonances of this structure, and how it is excited, I study the excitation of a single strip and slot. The slot-strip system is studied as it is a simpler structure than the "mixed pair", but exhibits qualitatively similar behavior. The slot-strip system is also anisotropic, which allows the polarizations exciting the different parts of the structure to be seen, enabling the coupling mechanisms contributing to the response in this system to be determined. The slot is aligned along the y-axis, then the strip added aligned either in a parallel or perpendicular configuration, as shown in Fig. 4.10 (a). The strips are 25 mm long and 1.5 mm wide, and the FR4 substrate is used, resulting in a transmission peak in the same frequency range as the previous numerical simulations in this Chapter. Fig. 4.10 (b) shows the co-polarized

transmission for both incoming polarizations, for the parallel configuration of this set-up. The same results, but for the perpendicular arrangement, are shown in Fig. 4.10 (c).

For both arrangements, in Figs 4.10 (b, c), significant transmission is only seen when the incoming polarization is across the slot (S_{xx}). In Fig. 4.10 (c) the stop band is also observed. However, the resonances are too far apart for the stop band to also be studied for both arrangements. It should be noted that these graphs are plotted using a logarithmic scale, so it can be seen that the transmission for the wave polarized along the slot (S_{yy}) is negligible. By looking at these results, it can be concluded that the predominant mechanism in exciting this structure is through the hole-mode in the slot. The strip is then excited by the electric field parallel to it and as the strip is rotated from parallel to perpendicular to the slot, the strength of its excitation changes. This couples to the excitation of the slot to determine the properties of the resonance. It can thus be concluded that the predominant excitation in our structure is through the hole-mode in the complementary structure aligned perpendicular to the magnetic field, which then couples primarily to the perpendicular corresponding arm of the cross.

4.5 Conclusion

In this chapter I have proposed a "mixed pair" structure, which is a combination of a meta-atom with its complement, and found large, flat optical activity at resonance, accompanied by very low ellipticity in the polarization of the transmitted wave. This is in contrast to the highly dispersive optical activity and ellipticity normally found in twisted chiral structures.

I have also shown how these effects can be optimized by changing the twist angle θ, and the spacing between the elements. I found that maximum optical activity at resonance, for a separation of 1.6 mm, occurs at a twist angle of about 17.5°. This angle will change depending on the separation. I also investigated the possibility of increasing the number of complementary pairs to enhance the effects, and found that the effect can still hold.

I then investigated how increasing the losses affected the system, and found little to no effect on the optical activity. I experimentally verified the results and found good

agreement. I also found experimental agreement with the effect of changing the internal rotation.

Finally, I investigated how the structure is excited, by studying numerically a strip combined with a slot. I found that the the excitation of the hole modes in the arms of the cross dominate the excitation of the structure. The rotation angle then changes the coupling between the hole modes and the cross arms.

This is the first time to my knowledge that such an effect has been found for a twisted chiral structure. This effect is very important for chiral applications that require linear polarization. There is also the possibility of investigating the properties of similar structures with lower orders of symmetry, such as a strip or split-ring resonator combined with its complement in order to determine if the mechanism is general, or specific to structures with a particular symmetry. It would also be beneficial to study the effective medium parameters of this system, which will require the development of a new retrieval approach. This will be considered in Chapter 5.

Chapter 5

Development of a Retrieval Procedure for an Asymmetric Chiral Medium

In Chapter 4 I proposed a "mixed pair", which is a combination of a cross and its complement, and demonstrated large, flat optical activity accompanied by very low ellipticity in the output polarized wave. This structure couples equivalent electric and magnetic dipoles, according to Babinet's principle. This structure also has C_4 symmetry, which is of lower-order symmetry than commonly studied metamaterial structures created by twisted identical resonators, which have D_4 symmetry [46,52].

To further understand this new type of structure, it is very important to calculate the effective parameters of such structures, as this will explain how the structure is polarized by the external fields. Obtaining the material parameters of metamaterial structures is a well established procedure for isotropic, achiral media [71]. The approach has been extended for the cases of chiral, bi-anisotropic and inhomogeneous media [40,103–105]. An alternative approach based on the state-transition matrices has also been proposed for isotropic chiral media [106], however none of these methods can be employed for metamaterials with C_4 symmetry. The parameters for the structures with C_4 symmetry were retrieved in Ref. [42] under the assumption that the two bi-anisotropic parameters are related by a frequency-independent constant. This assumption is not valid for general structures, including the "mixed pair". This lower-symmetry results in the reflection being dependent on the propagation direction, and is due to the structure being physically different when seen from opposite directions.

There are, however, some well known limitations in effective medium models and the resulting retrieved parameters. The resulting parameters are also dependent on the thickness d, the definition of which can be ambiguous due to the effect of the near-field extending past the physical sample. While the physical thickness of the sample is the most popular choice, other cases have been made. This also means that the retrieval methods are less useful as the number of layers is increased [107]. The parameters can also become non-physical at resonance, resulting in forbidden conversion between circular polarizations at resonance, violating symmetry, as well as sign changes in the imaginary part of the permeability, violating passivity [71]. Despite these limitations, the resulting parameters can still be useful for gaining insight into the studied system.

In this Chapter I develop a retrieval procedure to determine the effective material parameters for meta-structures with C_4 symmetry. In Section 5.1 I retrieve the refractive indices and impedances for such structures in a unit cell configuration, based on the eigenvalues of the scattering-transfer matrix. The resulting effective parameters are then calculated. I verify this approach in Section 5.2, by recalculating the scattering matrix through the substitution of the retrieved material parameters. This is done by first calculating the admittance tensors. Section 5.3 then concludes the chapter.

5.1 Parameter Retrieval

To calculate the material parameters I use a unit cell model periodic in the x and y directions for simplification, as the waveguide mode is not uniform in the transverse direction, making it equivalent to a non-normal angle of incidence. The period of the unit cell is 59.7 mm. The cross and its complement are modeled having arms 28 mm in length and 1.5 mm in width, and are separated by 1.5 mm thick Rogers circuit board with a dielectric constant of 3.48, and a loss tangent of 0.0031 at 2.5 GHz. The metal is modeled as PEC. The elements are twisted through 20° and the complementary cross and the boards are now square in shape to fill up the unit cell, shown in Fig. 5.1. The system is excited using a plane wave at normal incidence, described using the time convention $\exp(i\omega t)$. Simulations are made using CST Microwave Studio, with the wave propagating along the z-axis. The two lowest order linearly polarized modes are excited. The first mode has the electric field directed along the y-axis, and the second directed along the x-axis.

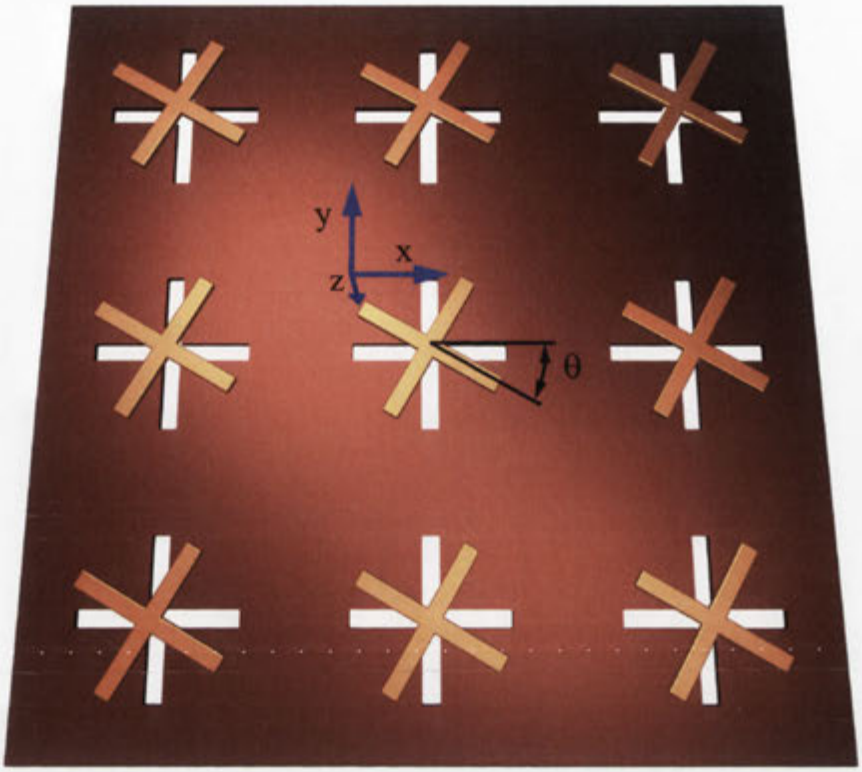

Figure 5.1: Schematic of the structure array. The cross is rotated relative to its complement through an angle θ, making up one unit cell. The arrows show the direction of the fields.

The most general case for this structure, including all possible internal rotation angles, has C_4 symmetry. At normal incidence there is no z component of the macroscopic fields, allowing the transverse components to be modeled using the reduced tensors

$$\bar{\bar{\epsilon}} = \begin{pmatrix} \epsilon & 0 \\ 0 & \epsilon \end{pmatrix}, \qquad \bar{\bar{\mu}} = \begin{pmatrix} \mu & 0 \\ 0 & \mu \end{pmatrix}, \qquad \bar{\bar{\kappa}} = \begin{pmatrix} \kappa & \xi \\ -\xi & \kappa \end{pmatrix}, \tag{5.1}$$

where ϵ is the effective permittivity, μ the effective permeability, κ the chirality, and ξ is a bi-anisotropic parameter which is not present in isotropic chiral media, and is introduced by the lower order of symmetry in this system. The off-diagonal components of $\bar{\bar{\epsilon}}$ and $\bar{\bar{\mu}}$ are 0 due to time reversal symmetry [35]. The resulting constitutive relations at normal incidence are

$$\begin{pmatrix} \mathbf{D} \\ \mathbf{B} \end{pmatrix} = \begin{pmatrix} \epsilon \bar{\bar{I}} & -i/c\left(\kappa \bar{\bar{I}} - \xi \bar{\bar{J}}\right) \\ i/c\left(\kappa \bar{\bar{I}} + \xi \bar{\bar{J}}\right) & \mu \bar{\bar{I}} \end{pmatrix} \cdot \begin{pmatrix} \mathbf{E} \\ \mathbf{H} \end{pmatrix}, \tag{5.2}$$

where $\bar{\bar{J}} = \mathbf{z}_0 \times \bar{\bar{I}}$ is the 90° rotator in the $x-y$ plane. The following parameters then need to be calculated: ϵ, μ, κ and ξ. The currently established approaches do not cover gen-

eral structures with this particular symmetry [40,42,105], so a new approach needs to be developed. There is the added complication that due to the meshing in the CST model not preserving 90° rotational symmetry the eigenstates are not perfectly circularly polarized in the numerical model. To account for this a much more robust method will be developed, where the scalar parameters of the eigenmodes of the scattering-transfer matrix will be found and used to assign effective parameters for a medium with circular eigenstates.

5.1.1 Eigenmode analysis

I start by solving the eigenvalues of the scattering-transfer matrix which are then used to find the refractive index n and the impedance Z. The impedance is a tensor, but due to symmetry there are only a few unique values which will be found. When dealing with the tensors, I will denote $\overset{\Rightarrow}{Z}$ as the impedance for waves traveling in the $+z$ direction, and $\overset{\Leftarrow}{Z}$ in the $-z$ direction. To calculate n and Z from the scattering parameters, the scattering-transfer matrix [108] is used, which can be found from the scattering matrix

$$\mathbf{T}_S = \begin{bmatrix} \mathbf{S_{21}}^{-1} & -\mathbf{S_{21}}^{-1}\mathbf{S_{22}} \\ \mathbf{S_{11}}\mathbf{S_{21}}^{-1} & \mathbf{S_{12}} - \mathbf{S_{11}}\mathbf{S_{21}}^{-1}\mathbf{S_{22}} \end{bmatrix}. \tag{5.3}$$

$\mathbf{S_{11}}$, $\mathbf{S_{12}}$, $\mathbf{S_{21}}$ and $\mathbf{S_{22}}$ are 2×2 arrays including both linear polarizations at each port. The eigenvalues λ_m of $\mathbf{T}_S$ represent solutions which are then found using the relation

$$\mathbf{F}(z+d) = \mathbf{T}_S\mathbf{F}(z) = e^{i\alpha d}\mathbf{F}(z) = \lambda\mathbf{F}(z), \tag{5.4}$$

where α is the phase advance across the unit cell of thickness d, and $\mathbf{F}$ is defined as

$$\mathbf{F}(z) = \begin{pmatrix} b_1 \\ b_2 \\ a_1 \\ a_2 \end{pmatrix}. \tag{5.5}$$

a_m and b_m are the amplitudes of the waves propagating towards and away from the structure at the interface $z = d$, and can be defined as

$$b_m = (\sqrt{z_0}E_m + H_m/\sqrt{z_0})/2, \tag{5.6}$$

$$a_m = (\sqrt{z_0}E_m - H_m/\sqrt{z_0})/2. \tag{5.7}$$

The value of m refers to the linear mode being considered and z_0 is the impedance of free space.

Reference [105] uses the relation in Eq. (5.4) with the transmission matrix, however this still holds when using scattering-transfer parameters as well. The four eigenvalues correspond to the forwards and backwards modes of the two polarizations. The refractive indices can then be found as

$$n = \frac{\ln(\lambda)}{k_0 d}, \tag{5.8}$$

where d is the thickness of the sample (the substrate thickness plus the thickness of both metal resonators), and k_0 is the wavenumber in free space. While the appropriate choice for d is ambiguous, as discussed in the introduction to this chapter, this needs to be the same thickness that the scattering parameters are calculated over, from Eq. 5.4. The physical sample thickness has been chosen as this is the easiest to measure the fields over. The main effect of using a larger value of d would be the diluting the parameters due to the free space included. The resulting indices of the two polarizations for both directions are plotted in Fig. 5.2 (a) and (b). The real part of the index is seen to be clearly dependent on the polarization, and not on the direction of propagation. This is consistent with Lorentz reciprocity, which means that for each polarization the refractive index is identical for forwards and backwards propagation.

By finding the eigenvectors $\mathbf{F}(z)$ corresponding to these eigenvalues, the fields in the structure can be studied. From symmetry considerations, the eigenstates of this structure are expected to be circularly polarized, where

$$\mathbf{E}_{\pm} = \mathbf{E}_x \pm i\mathbf{E}_y, \tag{5.9}$$

and this can be verified by inspecting the relative amplitude and phase of the compo-

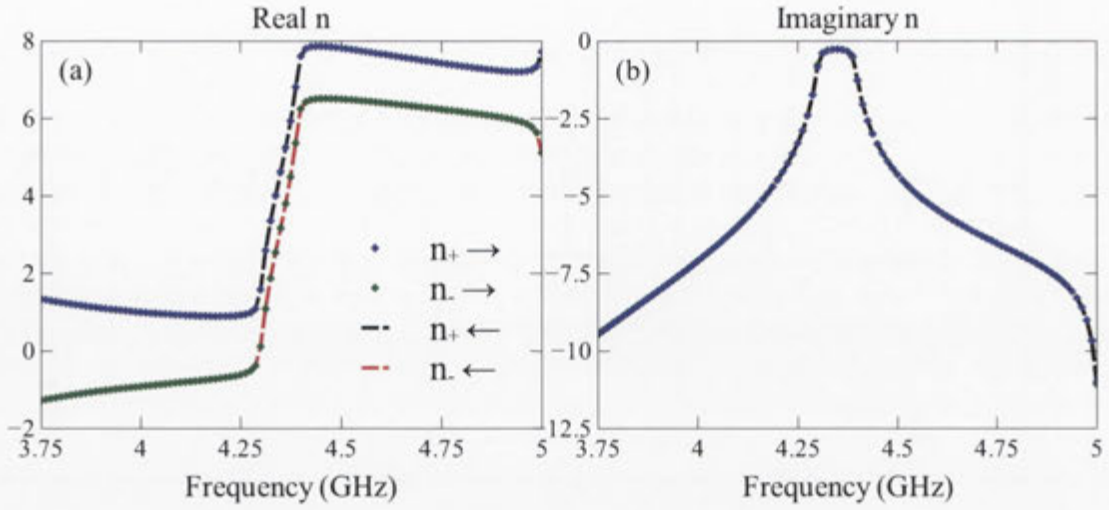

Figure 5.2: (a) Real and (b) imaginary parts of the retrieved refractive indices for both polarizations and directions. The forwards direction is denoted by $\rightarrow$ (markers), and the backwards by $\leftarrow$ (lines).

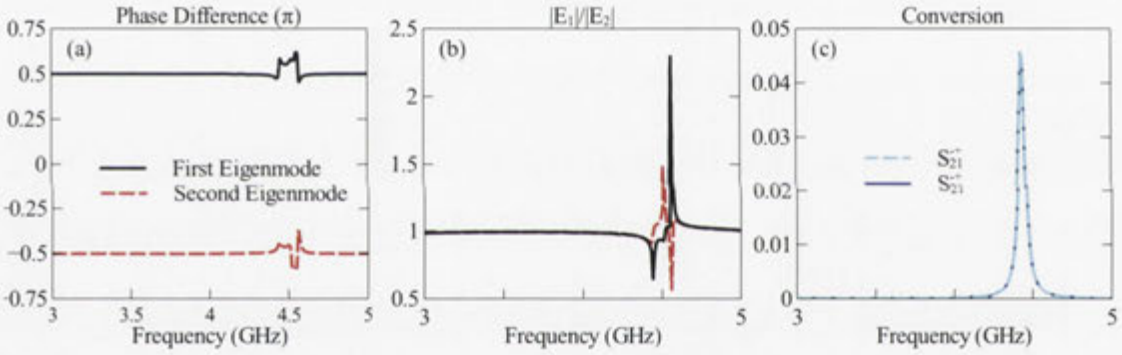

Figure 5.3: (a) Phase difference between the two electric components E_1 and E_2 of the propagating waves, for both eigenstates, in factors of π. (b) Ratio of magnitudes for the two components E_1 and E_2. (c) Conversion between the right and left handed polarizations.

nents of the eigenvectors. In Fig. 5.3 (a) the phase difference between the two electric components for both eigenstates is plotted. Fig. 5.3 (b) shows $|E_1|/|E_2|$ as a function of frequency. For a circular polarization the two electric components will be out of phase by $\pi/2$, and will have equal magnitude. From Fig. 5.3 it can be seen that this is the case, apart from at resonance, where the polarizations deviate slightly from a circular polarization. At this point there is conversion between the right and left handed polarizations, shown in Fig. 5.3(c), despite this being prohibited by the symmetry of the structure. This deviation is due to the mesh not having C_4 symmetry, so I am physically justified in treating the eigenstates as circularly polarized for the purpose of calculating the impedances and material parameters.

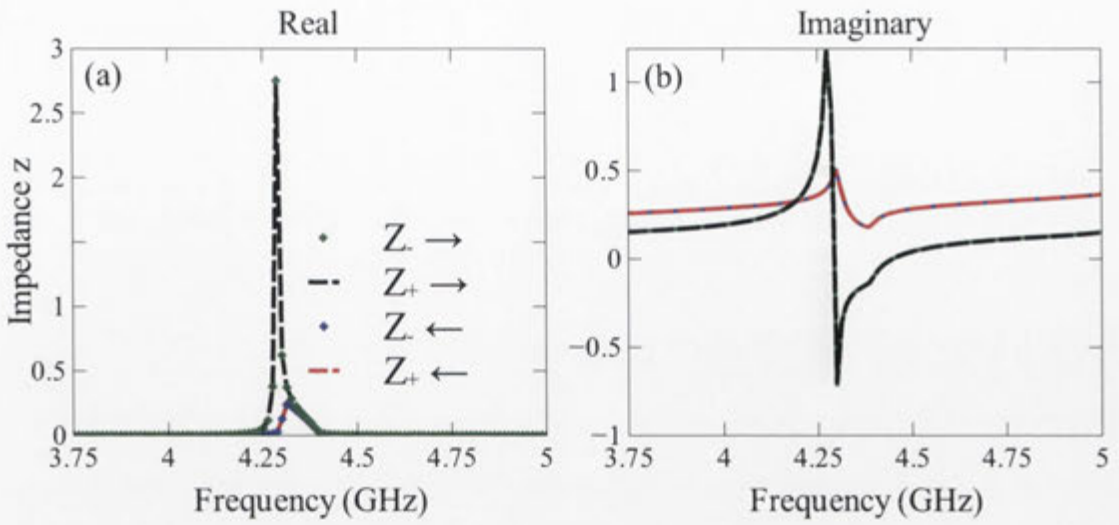

Figure 5.4: (a) Real and (b) imaginary impedances for both polarizations, for both forward and backward directions. The forwards direction is denoted by $\rightarrow$, and the backwards by $\leftarrow$. Z_+ is denoted using dashed lines, and Z_- using markers.

Equations (5.5) - (5.7) can be rearranged to find the ratio of E/H in order to calculate the scalar impedances. For circularly polarized waves, $E_x = E_1$ and $E_y = E_2$ and the resulting impedances are found as

$$Z^{\pm} = \frac{E_{\pm}}{H_{\pm}} = z_0 \left[\frac{b_2 + a_2 \pm i\,(b_1 + a_1)}{b_2 - a_2 \pm i\,(b_1 - a_1)} \right]. \tag{5.10}$$

As there exists an eigenvector $\mathbf{F}(z)$ corresponding to each eigenvalue, the values of b_1, b_2, a_1 and a_2 in the above equation will change depending on which eigenstate is being considered.

The resulting impedances are plotted in Fig. 5.4 (a) and (b), for a twist angle of 20°. It can be seen that the impedances are only dependent on the propagation direction and not the polarization. This is expected, as in more symmetric chiral materials, the two circular polarizations have the same impedance [40].

5.1.2 Determining the material tensors

Now that I have the scalar index of refraction and impedance for each eigenmode, I can calculate the effective medium parameters. By considering the material relations in Eq. (5.2), the equations for the refractive index and impedances from the effective parameters can be found by using Maxwell's equations and taking a plane wave expansion of the fields. The full derivation of these equations can be found in Ref. [35],

sections 8.1.1 and 8.2.2. In this section, subscripts $1,2$ will be used to denote polarizations, except when the polarizations are circular, in which case $\pm$ will be used.

The refractive indices for the two polarizations $n_{1,2}$ can be found using

$$n_{1,2}^2 = \epsilon\mu + \kappa^2 - \xi^2 + \left(\kappa\kappa_z - \frac{1}{2}(\epsilon\mu_z + \epsilon_z\mu)\right)\frac{k_t^2}{ak_0^2} \pm \sqrt{D}, \tag{5.11}$$

where $Re\sqrt{D} > 0$ and

$$D = \frac{k_t^4}{4a^2k_0^4}(\epsilon\mu_z - \epsilon_z\mu)^2 + \kappa^2\epsilon_z\mu_z\frac{k_t^4}{a^2k_0^4} - \kappa\frac{k_t^2}{ak_0^2}\left(2\kappa + \kappa_z\frac{k_t^2}{ak_0^2}\right)(\epsilon\mu_z + \epsilon_z\mu) - 4\xi^2\kappa\left(\kappa + \kappa_z\frac{k_t^2}{ak_0^2}\right) + \epsilon\mu\left(2\kappa + \kappa_z\frac{k_t^2}{ak_0^2}\right)^2. \tag{5.12}$$

κ_z, ϵ_z and μ_z are the components of the material tensors in the z direction (wave propagation direction). k_t is the transverse component of the wave vector, k_0 is the free space wave number and $a = \epsilon_z\mu_z - \kappa_z^2$. As this structure is excited at normal incidence, I take the limit of these equations as $k_t \to 0$, which means that the polarizations will be circular, and the resulting indices will be

$$n_\pm = \sqrt{\epsilon\mu - \xi^2} \pm \kappa. \tag{5.13}$$

In this limit it can be seen that the parameters κ_z, ϵ_z and μ_z do not contribute to the refractive index. In the limit of $\xi = 0$, as is the case for an isotropic chiral structure, this simplifies to

$$n_\pm = \sqrt{\epsilon\mu} \pm \kappa, \tag{5.14}$$

which is the well known refractive index of a chiral material [40].

The impedance tensors can then be found using [35]

$$\bar{\bar{Z}}_{1,2} = \frac{\eta_0}{\epsilon}\left\{(n_{1,2} \pm i\xi)\left[\frac{\mathbf{k}_t\mathbf{k}_t}{k_t^2} + \frac{\epsilon ak_0^2}{\epsilon ak_0^2 - \epsilon_z k_t^2}\frac{\mathbf{k}_t \times \mathbf{z}_0\mathbf{k}_t \times \mathbf{z}_0}{k_t^2}\right] \pm i\left[\left(\frac{\epsilon\left(\kappa ak_0^2 + \kappa_z k_t^2\right)}{\epsilon ak_0^2 - \epsilon_z k_t^2}\right)\frac{\mathbf{z}_0 \times \mathbf{k}_t\mathbf{k}_t}{k_t^2} + \kappa\frac{\mathbf{k}_t\mathbf{k}_t \times \mathbf{z}_0}{k_t^2}\right]\right\}. \tag{5.15}$$

where the positive sign is chosen for direction $-z$, and the negative sign for direction

$+z$. Taking the limit as $k_t \to 0$, the equations become

$$\overrightarrow{\overrightarrow{Z}}_{\pm} = \frac{\eta_0}{\epsilon}\left[(n_{\pm} + i\xi)\,\overline{\overline{I}} + i\kappa\overline{\overline{J}}\right], \tag{5.16}$$

$$\overleftarrow{\overleftarrow{Z}}_{\pm} = \frac{\eta_0}{\epsilon}\left[(n_{\pm} - i\xi)\,\overline{\overline{I}} - i\kappa\overline{\overline{J}}\right]. \tag{5.17}$$

The eigenvalues Z for the different polarizations and propagation directions can then be found, giving the impedances for the eigenstates in the medium. Each of the four eigenstates will have two potential eigenvalues, the correct one being determined by the corresponding eigenvector. For $\overrightarrow{\overrightarrow{Z}}_{\pm}$ the scalar impedances are degenerate and are

$$Z_1 = \frac{\eta_0}{\epsilon}(n + i\xi), \tag{5.18}$$

and for $\overleftarrow{\overleftarrow{Z}}_{\pm}$ the scalar impedances are again degenerate, and are

$$Z_2 = \frac{\eta_0}{\epsilon}(n - i\xi), \tag{5.19}$$

where

$$n = \frac{n_+ + n_-}{2}. \tag{5.20}$$

There are then two unique eigenvalues, which supports the earlier argument that the impedance is only dependent on the direction, as shown in Fig. 5.4(a-b).

Eq. (5.13) can then be rearranged along with these eigenvalues to find equations for the retrieval of the parameters μ, ϵ, κ and ξ:

$$\epsilon = \frac{2\eta_0 n}{Z_1 + Z_2}; \qquad \xi = \frac{i\epsilon(Z_2 - Z_1)}{2\eta_0}; \tag{5.21}$$

$$\mu = \frac{n^2 + \xi^2}{\epsilon}; \qquad \kappa = \frac{n_+ - n_-}{2}.$$

Both the real and imaginary parts of the retrieved parameters are plotted in Fig. 5.5. In Fig. 5.5 (a) it can be seen that the imaginary part of μ becomes positive, violating passivity, which is a known problem with assigning local parameters to metamaterials [71],as discussed at the beginning of this chapter. The effective parameters can still yield useful insights. In Fig. 5.5 (c) κ is plotted, the real part of which is directly related

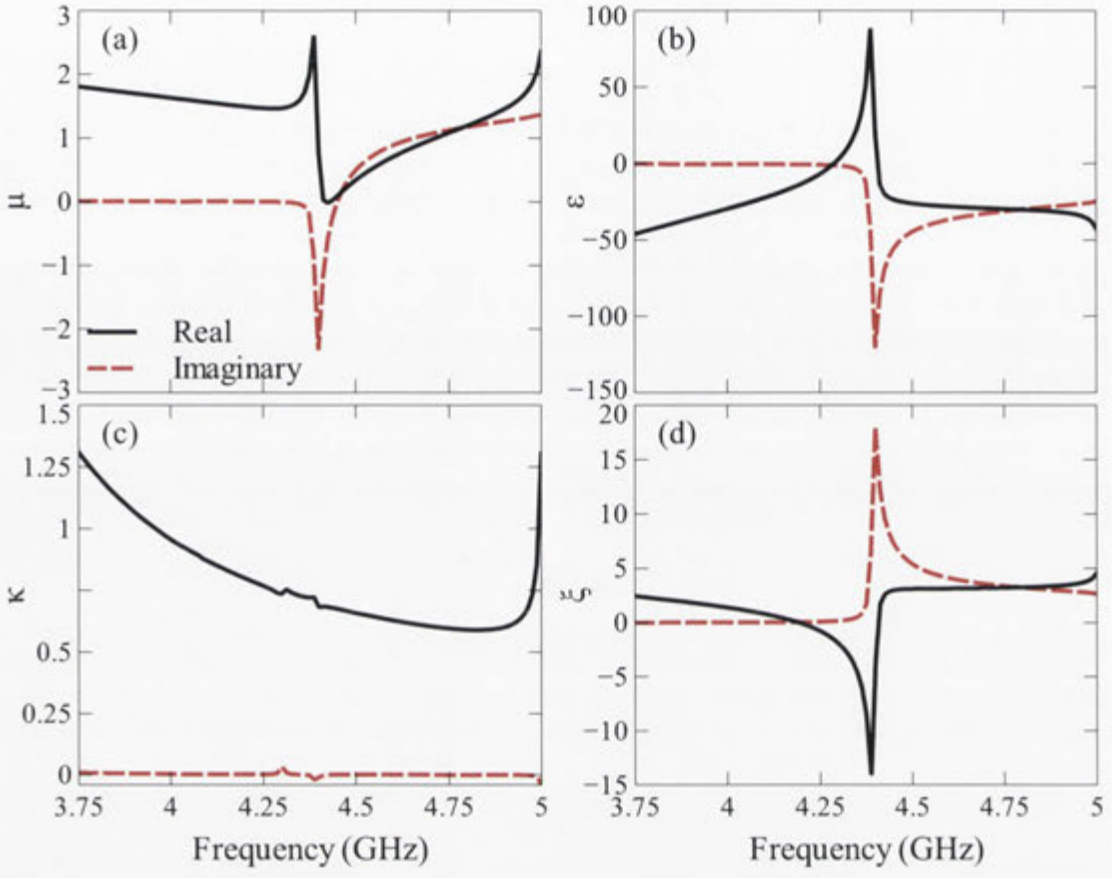

Figure 5.5: Real (solid black) and imaginary (red dashed) parts of the retrieved parameters: (a) magnetic permeability μ, (b) electric permittivity ϵ, (c) chirality κ and (d) bi-anisotropy ξ.

to the optical activity, and the imaginary part defines the ellipticity. The real part is relatively flat, consistent with my previous findings in Chapter 4. It can also be seen that the imaginary part is very low, corresponding to the very low ellipticity predicted in section 4.1 and measured in section 4.3.2.

The real and imaginary parts of ξ are plotted in Fig. 5.5 (d). This determines the asymmetry of the structure as shown in the reflection coefficients. It is worth reiterating here that these parameters are strongly dependent on the earlier choice of d. These parameters are also only valid for this particular system, and would look very different if further layers were added. This can be seen in the optical activity and ellipticity shown in Figs. 4.5 (b,c).

5.2 Checking the retrieved parameters

There are a number of checks that these parameters need to satisfy in order to be valid. The first checks apply this retrieval approach to the "corner" cases of $\kappa = \xi = 0$, $\kappa = 0$ and $\xi = 0$, and compares the results to those obtained using well established retrieval methods [40, 71, 105]. This was found to be the case (not shown). The final check is a consistency check, using the retrieved parameters for the general case to reproduce the scattering parameters theoretically. I will recalculate the scattering parameters ($\mathbf{S}_{11}$ and $\mathbf{S}_{21}$) by re-substitution, calculating the scattering parameters based on the admittance tensors for a reciprocal bi-anisotropic medium. The scattering parameters can be calculated using

$$\mathbf{S}_{11} = \left[\left(\bar{\bar{Y}}_d + \overleftarrow{\bar{Y}} \right) \cdot e^{i \overleftarrow{\bar{\beta}} d} \cdot \left(\overrightarrow{\bar{Y}} + \overleftarrow{\bar{Y}} \right)^{-1} \cdot \left(\bar{\bar{Y}}_0 + \overrightarrow{\bar{Y}} \right) - \left(\bar{\bar{Y}}_d - \overrightarrow{\bar{Y}} \right) \cdot e^{-i \overrightarrow{\bar{\beta}} d} \cdot \left(\overrightarrow{\bar{Y}} + \overleftarrow{\bar{Y}} \right)^{-1} \cdot \left(\bar{\bar{Y}}_0 - \overleftarrow{\bar{Y}} \right) \right]^{-} \cdot \left[\left(\bar{\bar{Y}}_d + \overleftarrow{\bar{Y}} \right) \cdot e^{i \overleftarrow{\bar{\beta}} d} \cdot \left(\overrightarrow{\bar{Y}} + \overleftarrow{\bar{Y}} \right)^{-1} \cdot \left(\bar{\bar{Y}}_0 - \overrightarrow{\bar{Y}} \right) - \left(\bar{\bar{Y}}_d - \overrightarrow{\bar{Y}} \right) \cdot e^{-i \overrightarrow{\bar{\beta}} d} \cdot \left(\overrightarrow{\bar{Y}} + \overleftarrow{\bar{Y}} \right)^{-1} \cdot \left(\bar{\bar{Y}}_0 + \overleftarrow{\bar{Y}} \right) \right], \tag{5.22}$$

and

$$\mathbf{S}_{21} = 2 \left[\left(\bar{\bar{Y}}_0 + \overrightarrow{\bar{Y}} \right) \cdot \left(e^{-i \overrightarrow{\bar{\beta}} d} \right)^{-1} \cdot \left(\overrightarrow{\bar{Y}} + \overleftarrow{\bar{Y}} \right)^{-1} \cdot \left(\bar{\bar{Y}}_d + \overleftarrow{\bar{Y}} \right) - \left(\bar{\bar{Y}}_0 - \overleftarrow{\bar{Y}} \right) \cdot \left(e^{i \overleftarrow{\bar{\beta}} d} \right)^{-1} \cdot \left(\overrightarrow{\bar{Y}} + \overleftarrow{\bar{Y}} \right)^{-1} \cdot \left(\bar{\bar{Y}}_d - \overrightarrow{\bar{Y}} \right) \right]^{-1} \cdot \bar{\bar{Y}}_0, \tag{5.23}$$

where $\bar{\bar{Y}}$ is the admittance tensor, and $\bar{\bar{Y}}_{0,d}$ are the admittances at the structure boundaries. These equations are found by requiring the transverse fields to be continuous over the interfaces between the sample and its surroundings, the full derivation of which can again be found in Ref. [35].

It can be seen that the scattering equations are dependent on the admittance tensors $\bar{\bar{Y}}$ and the propagation tensors for the polarized waves $e^{\pm i \bar{\bar{\beta}} d}$.

5.2.1 Developing the analytical solutions

To develop the analytical solutions for the propagation tensors, a reciprocal basis $\mathbf{E}_1'$ and $\mathbf{E}_2'$ is introduced [35], based on the two-dimensional basis $\mathbf{E}_1$ and $\mathbf{E}_2$, which are

the field vectors calculated using the eigenvectors in Section 5.1.1. The reciprocal basis vectors are found using

$$\mathbf{E}'_{1,2} = \frac{\mathbf{z}_0 \times \mathbf{E}_{2,1}}{\mathbf{E}_{1,2} \cdot (\mathbf{z}_0 \times \mathbf{E}_{2,1})}, \tag{5.24}$$

and will satisfy

$$\mathbf{E}'_{1,2} \cdot \mathbf{E}_{2,1} = 0, \qquad \mathbf{E}'_{1,2} \cdot \mathbf{E}_{1,2} = 1. \tag{5.25}$$

For this structure the eigenstates are circularly polarized, so $\mathbf{E}_1$ and $\mathbf{E}_2$ are left- and right-handed circularly polarized waves of equal magnitude. This requires that $E_{1x} = E_{1y} = E_{2x} = E_{2y}$ and $\mathbf{E}_{1,2} = \mathbf{E}_{\pm}$. From Eq. (5.9) the vectors are then

$$\vec{\mathbf{E}}_+ = E \begin{pmatrix} 1 \\ i \end{pmatrix}; \qquad \vec{\mathbf{E}}_- = E \begin{pmatrix} 1 \\ -i \end{pmatrix}, \tag{5.26}$$

with resulting reciprocal basis vectors of

$$\vec{\mathbf{E}}'_+ = \frac{1}{2E} \begin{pmatrix} 1 \\ -i \end{pmatrix}; \qquad \vec{\mathbf{E}}'_- = \frac{1}{2E} \begin{pmatrix} 1 \\ i \end{pmatrix}. \tag{5.27}$$

Then

$$\vec{\mathbf{E}}_+ \vec{\mathbf{E}}'_+ = \frac{1}{2} \begin{bmatrix} 1 & -i \\ i & 1 \end{bmatrix}; \qquad \vec{\mathbf{E}}_- \vec{\mathbf{E}}'_- = \frac{1}{2} \begin{bmatrix} 1 & i \\ -i & 1 \end{bmatrix}. \tag{5.28}$$

For the backwards propagation direction $\overleftarrow{\mathbf{E}}_+ = \vec{\mathbf{E}}_-$ and vice versa.

The propagation factors $e^{i\overleftarrow{\beta}d}$ and $e^{-i\vec{\beta}d}$ are then found using [35]

$$\begin{aligned} e^{i\overleftarrow{\beta}d} &= e^{in_- k_0 d} \overleftarrow{\mathbf{E}}_+ \overleftarrow{\mathbf{E}}'_+ + e^{in_+ k_0 d} \overleftarrow{\mathbf{E}}_- \overleftarrow{\mathbf{E}}'_-, \\ e^{-i\vec{\beta}d} &= e^{-in_+ k_0 d} \vec{\mathbf{E}}_+ \vec{\mathbf{E}}'_+ + e^{-in_- k_0 d} \vec{\mathbf{E}}_- \vec{\mathbf{E}}'_-, \end{aligned} \tag{5.29}$$

resulting in

$$\begin{aligned} e^{i\overleftarrow{\beta}d} &= \frac{1}{2} \left\{ e^{in_+ k_0 d} \left(\bar{\bar{I}}_t + i\bar{\bar{J}} \right) + e^{in_- k_0 d} \left(\bar{\bar{I}}_t - i\bar{\bar{J}} \right) \right\}; \\ e^{-i\vec{\beta}d} &= \frac{1}{2} \left\{ e^{-in_- k_0 d} \left(\bar{\bar{I}}_t + i\bar{\bar{J}} \right) + e^{-in_+ k_0 d} \left(\bar{\bar{I}}_t - i\bar{\bar{J}} \right) \right\}. \end{aligned} \tag{5.30}$$

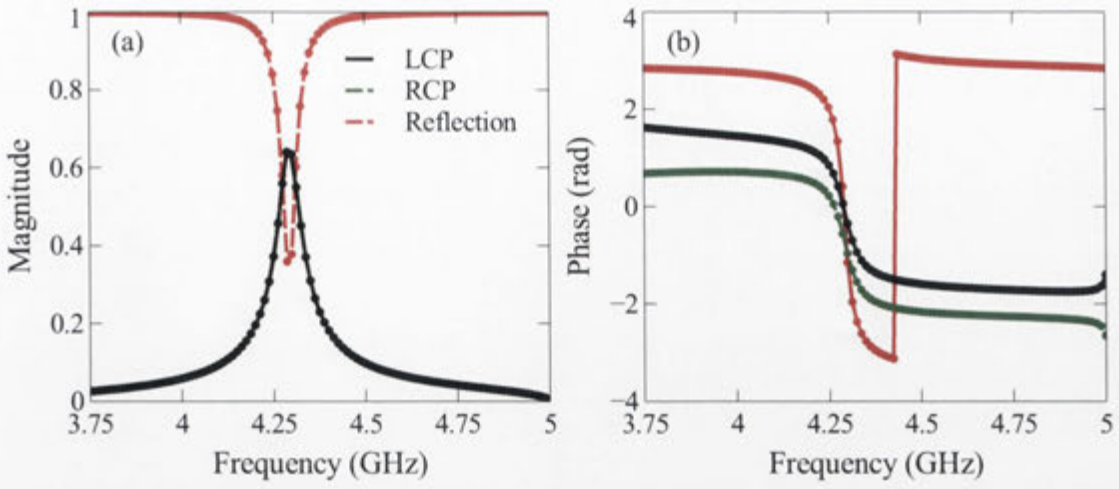

Figure 5.6: (a) Magnitude and (b) phase of the scattering parameters calculated by re-substituting the retrieved parameters. The lines are from CST, the markers from the theory. The reflection is in red, RCP transmission in green, and LCP transmission in black.

5.2.2 Calculating the admittance tensors

As $\bar{\bar{Y}} = \bar{\bar{Z}}^{-1}$, the eigenvalues for the admittance tensors can be found by inverting Eqs. (5.18-5.19), and substituting in μ from Eq. 5.21. Taking the eigenvalues as diagonal components of the tensors results in

$$\begin{aligned} \overrightarrow{\bar{\bar{Y}}} &= \frac{(n - i\xi)}{\mu\eta_0}\bar{\bar{I}}; \\ \overleftarrow{\bar{\bar{Y}}} &= \frac{(n + i\xi)}{\mu\eta_0}\bar{\bar{I}}. \end{aligned} \tag{5.31}$$

If the system is considered as a slab of thickness d, then $\bar{\bar{Y}}_0$ is the admittance tensor for the region $z < 0$, found as a special case of Eq. (5.31). $\bar{\bar{Y}}_d$ is the tensor for the region $z > d$. For this system these regions are both free space, so

$$\bar{\bar{Y}}_0 = \bar{\bar{Y}}_d = \frac{1}{\eta_0}\bar{\bar{I}}. \tag{5.32}$$

5.2.3 Calculating the scattering Parameters

The scattering parameters $\mathbf{S}_{11}$ and $\mathbf{S}_{21}$ can now be evaluated by substituting Eqs. (5.32, 5.31) and (5.30) into Eqs. (5.22) and (5.23). The results for both polarizations are plotted in Fig. 5.6, and show near perfect agreement between our original simulations and the recalculations. It can also be seen that the nearly constant difference between the transmission phases in Fig. 5.6 (b) is consistent with the flat optical activity.

The reflection plotted is that for the forward incidence - to recalculate the opposite direction, the sign of ξ needs to be changed. The reflection was found to be equal for both polarizations within numerical error, as is expected [40]. These calculated scattering parameters confirm the consistency of this new retrieval approach, and also justify the treatment of the polarizations of the eigenmodes as circular, as this is the assumption made in calculating and inverting the parameters.

5.3 Conclusion

In this Chapter I have continued to study the "mixed pair" proposed in Chapter 4. It is important to be able to retrieve the effective parameters for a structure, as it gives a good explanation of how the structure is polarized by the external fields. However no such method existed for a general structure with C_4 symmetry. To remedy this I have developed a novel retrieval method for calculating the effective material parameters which is applicable to single-layer structures with C_4 symmetry at normal incidence, and verified the accuracy of this new approach.

A method of calculating the refractive indices and impedances was developed based on the eigenvalues of the scattering-transfer matrix. Equations were then derived to calculate the effective parameters from the indices and impedances.

I have verified the consistency of this approach by calculating the scattering parameters theoretically and comparing them with results obtained from the numerical simulations. The scattering parameters were calculated from the admittance tensors for this structure, and agreed almost perfectly with the numerical results.

This is the first time to my knowledge that a parameter retrieval approach has been developed for general structures with this particular symmetry. This is a robust method for retrieving the effective parameters.

Chapter 6

Conclusion

Metamaterials are important for engineering materials with unique properties. A large amount of effort has gone into designing better ways to create them for a range of applications. The response of a bulk metamaterial is determined both by the properties of the individual resonators, and the coupling between them. The near-field interaction is vital for understanding the response of a metamaterial and is best studied using pairs of resonators, as the effect is strongest between neighboring meta-atoms. Accordingly, I have used resonator pairs to further the study of the near-field interaction, and investigated the effect it has on other properties such as the nonlinear response and the chirality. This work is an important step in increasing the understanding of how the coupling between neighboring resonant elements affects a metamaterial system, which should result in further efforts towards utilizing strongly coupled meta-atoms.

By changing the relative rotation between a pair of split-ring resonators, I experimentally and numerically investigated the near-field interaction. Changing the rotation angle modifies the electric and magnetic interaction between the rings, tuning the hybridized resonances. Using both numerical simulations and an analytical model that takes into account both electric and magnetic interactions between the rings, I found that there is a crossing where the two resonances coexist, at an angle where the electric and magnetic coupling are equal. The waveguide walls and experimental errors can cause the crossing of the dispersion curve to be avoided, and by using the theory of Morse critical points, it was found that the losses can cause the crossing to be restored. This analysis gives further understanding of the near field response between resonators. It also suggests the possibility of achieving a specific set of parameters where both the frequency and the decay constants of the resonances are degenerate, causing the coupling to be suppressed. This would have important implications for mitigating spatial

dispersion.

The influence of the near-field interaction on the nonlinear properties of a structure was demonstrated, using a pair of coupled SRRs with varactors attached. I found that by shifting the two rings relative to each other, the nonlinear properties of both the symmetric and antisymmetric resonant modes in the system can be controlled. I then explained the tuning of the nonlinear response by studying the linear properties of the system, including the voltages generated across the diodes. This research should stimulate further work in controlling and designing the nonlinear properties of metamaterials. In particular, the system could be scaled down, making appropriate changes in the design process, for use at higher frequencies.

The interaction between twisted planar elements was then used to study chiral properties. I proposed a "mixed pair" structure, which is a combination of a meta-atom with its complement. Such a combination couples equivalent electric and magnetic dipoles, according to Babinet's principle, and has C_4 symmetry, which is a lower order symmetry than a pair of twisted crosses or complementary crosses. This "mixed pair" overcomes issues with other twisted structures, where highly dispersive optical activity is often accompanied by ellipticity in the polarization of the transmitted wave. In contrast to other rotated structures, I found that the "mixed pair" can possess large, flat optical activity over the transmission resonance, accompanied by very low ellipticity. I have also shown how these effects can be optimized, including through changing the internal twist angle θ, and increasing the number of complementary pairs. The optical activity and ellipticity for the structure, along with the effect of changing the rotation, were confirmed experimentally. The effect of changing the spacing between the elements was also investigated, and the excitation mechanism of the structure determined. This was done by studying the excitation of a strip combined with a slot, and showed that the excitation of this structure is predominantly determined by the currents around the "arms" of the complementary cross.

The effects of the material's symmetry on the bi-anisotropic properties was also investigated. I developed a new retrieval method applicable for metamaterials with C_4 symmetry at normal incidence, based on the eigenvalues of the scattering transfer matrix, and then calculated the resulting material parameters for a unit cell array, including

the extra bi-anisotropic parameter ξ. I verified the accuracy of this approach by calculating the scattering parameters theoretically. This is the first general retrieval approach developed for this set of parameters to my knowledge. This approach could be easily extended for use in more general media, including structures inside a waveguide or excited at non normal incidence.

This research has shown the importance of near-field coupling in the design of metamaterials, and that this near-field coupling can be used to manipulate nonlinear and chiral properties. It also highlights the need for continued research in the field. In particular, my results from the "mixed pair" should stimulate further research on understanding coupling properties and resonant modes of similar structures, as well as potential applications for linear polarization control. Whether these effects will hold for "mixed pairs" consisting of other resonators, or for increasing numbers of complementary pairs in longitudinal arrays, would be particularly of interest. In order to more thoroughly optimize and understand this system, a dipole model could be developed.

Bibliography

[1] A.L. Yerokhin, X. Nie, A. Leyland, A. Matthews, and S.J. Dowey. Plasma electrolysis for surface engineering. *Surf. and Coatings Technol.*, 122(2-3):73, 1999.

[2] S. Andryieuski. Biophotonics: Photonic crystals aid fish's night vision. *Nat. Photon.*, 6(9):575, 2012.

[3] B. Bahadur. *Liquid Crystals: Applications and Uses*. Number v. 1. World Scientific Publishing, 1990.

[4] J.B. Pendry, A.J. Holden, D.J. Robbins, and W.J. Stewart. Magnetism from Conductors and Enhanced Nonlinear Phenomena. *IEEE Trans. Microw. Theory Techn.*, 47(11):2075, 1999.

[5] D.R. Smith, W.J. Padilla, D.C. Vier, S.C. Nemat-Nasser, and S. Schultz. Composite medium with simultaneously negative permeability and permittivity. *Phys. Rev. Lett.*, 84(18):4184, 2000.

[6] M. Lapine, M. Gorkunov, and K.H. Ringhofer. Nonlinearity of a metamaterial arising from diode insertions into resonant conductive elements. *Phys. Rev. E*, 67(6):065601, 2003.

[7] T.Q. Li, H. Liu, T. Li, S.M. Wang, R.X. Wu, P. Chen, S.N. Zhu, and S. Schultz. Magnetic resonance hybridization and optical activity of microwaves in a chiral metamaterial. *Appl. Phys. Lett.*, 92(13):131111, 2008.

[8] D. Schurig, J. Mock, B. Justice, S.A. Cummer, J.B. Pendry, A.F. Starr, and D.R. Smith. Metamaterial electromagnetic cloaking at microwave frequencies. *Science*, 314(5801):977, 2006.

[9] T. Yen, W. Padilla, N. Fang, D.C. Vier, D.R. Smith, J.B. Pendry, D.N. Basov, and X. Zhang. Terahertz magnetic response from artificial materials. *Science*, 303(5663):1494, 2004.

[10] S. Linden, C. Enkrich, M. Wegener, J. Zhou, Th. Koschny, and C.M. Soukoulis. Magnetic response of metamaterials at 100 terahertz. *Science*, 306(5700):1351, 2004.

[11] Y. Yang, R. Huang, L. Cong, Z. Zhu, J. Gu, Z. Tian, R. Singh, S. Zhang, J. Han, and W. Zhang. Modulating the fundamental inductive-capacitive resonance in asymmetric double-split ring terahertz metamaterials. *Appl. Phys. Lett.*, 98(12):121114, 2011.

[12] J. Zhou, Th. Koschny, M. Kafesaki, E.N. Economou, J.B. Pendry, and C.M. Soukoulis. Saturation of the magnetic response of split-ring resonators at optical frequencies. *Phys. Rev. Lett.*, 95(22):223902, 2005.

[13] S. Tretyakov. On geometrical scaling of split-ring and double-bar resonators at optical frequencies. *Metamaterials*, 1(1):40, 2007.

[14] S. Zhang, W. Fan, B.K. Minhas, A. Frauenglass, K.J. Malloy, and S.R.J. Brueck. Midinfrared resonant magnetic nanostructures exhibiting a negative permeability. *Phys. Rev. Lett.*, 94(3):037402, 2005.

[15] S. Zhang, W. Fan, N.C. Panoiu, K.J. Malloy, R.M. Osgood, and S.R.J. Brueck. Experimental demonstration of near-infrared negative-index metamaterials. *Phys. Rev. Lett.*, 95(3):137404, 2005.

[16] G. Dolling, M. Wegener, C.M. Soukoulis, and S. Linden. Negative-index metamaterial at 780 nm wavelength. *Opt. Lett.*, 32(1):53, 2007.

[17] M. Kafesaki, I. Tsiapa, N. Katsarakis, Th. Koschny, C.M. Soukoulis, and E.N. Economou. Left-handed metamaterials: The fishnet structure and its variations. *Phys. Rev. B*, 75(23):235114, 2007.

[18] N.A. Mirin, T.A. Ali, P. Nordlander, and N.J. Halas. Perforated semishells: Far-field directional control and optical frequency magnetic response. *ACS Nano*, 4(5):2701, 2010.

[19] A. Garcia-Etxarri, R. Gomez-Medina, L.S. Froufe-Perez, C. Lopez, L. Chantada, F. Scheffold, J. Aizpurua, M. Nieto-Vesperinas, and J.J. Saenz. Strong magnetic response of submicron silicon particles in the infrared. *Opt. Express*, 19(6):4815, 2011.

[20] K. Eason, B. Luk'yanchuk, Y. Zhou, A.E. Miroshnichenko, and Y.S. Kivshar. Magnetic microscopy/metrology potential of metamaterials using nanosized spherical particle arrays. In *Proc. SPIE*, volume 8204, page 82042V, 2011.

[21] A.E. Miroshnichenko, B. Luk'yanchuk, S.A. Maier, and Y.S. Kivshar. Optically induced interaction of magnetic moments in hybrid metamaterials. *ACS Nano*, 6(1):837, 2012.

[22] Q. Zhao, L. Kang, B. Du, H. Zhao, Q. Xie, X. Huang, B. Li, J. Zhou, and L. Li. Experimental demonstration of isotropic negative permeability in a three-dimensional dielectric composite. *Phys. Rev. Lett.*, 101(2):027402, 2008.

[23] V. Veselago. Electrodynamics of substances with simultaneously negative electrical and magnetic permeabilities. *Sov. Phys. Usp.*, 10(4):509, 1968.

[24] J.B. Pendry. Negative refraction makes a perfect lens. *Phys. Rev. Lett.*, 85(18):3966, 2000.

[25] J.B. Pendry, A.J. Holden, W.J. Stewart, and I. Youngs. Extremely Low Frequency Plasmons in Metallic Mesostructures. *Phys. Rev. Lett.*, 76(25):4773, 1996.

[26] J.B. Pendry, A.J. Holden, D.J. Robbins, and W.J. Stewart. Low frequency plasmons in thin-wire structures. *J. Phys.: Condens. Matter*, 10(22):4785, 1998.

[27] D.R. Smith and N. Kroll. Negative refractive index in left-handed materials. *Phys. Rev. Lett.*, 85(14):2933, 2000.

[28] R.A. Shelby, D.R. Smith, and S. Schultz. Experimental verification of a negative index of refraction. *Science*, 292(5514):77, 2001.

[29] R. Marqués, F. Martín, and M. Sorolla. *Metamaterials with Negative Parameters*. John Wiley & Sons, 2008.

[30] J.D. Baena, R. Marques, J. Martel, and F. Medina. Experimental results on metamaterial simulation using SRR-loaded waveguides. In *Antennas and Propag. Soc. Int. Symp. (APSURSI), 2003 IEEE*, volume 1, page 106, 2003.

[31] R.A. Shelby, D.R. Smith, S.C. Nemat-Nasser, and S. Schultz. Microwave transmission through a two-dimensional, isotropic, left-handed metamaterial. *Appl. Phys. Lett.*, 78(4):489, 2001.

[32] Th. Koschny, L. Zhang, and C.M. Soukoulis. Isotropic three-dimensional left-handed metamaterials. *Phys. Rev. B*, 71(12):121103, 2005.

[33] U.K. Chettiar, A.V. Kildishev, H-K. Yuan, W. Cai, S. Xiao, V.P. Drachev, and V.M. Shalaev. Dual-band negative index metamaterial: double negative at 813nm and single negative at 772nm. *Opt. Lett.*, 32(12):1671, 2007.

[34] E. Cubukcu, K. Aydin, E. Ozbay, S. Foteinopoulou, and C.M Soukoulis. Negative refraction by photonic crystals. *Nature*, 423(June):604, 2003.

[35] A. Serdyukov, I. Semchenko, S. Tretyakov, and A. Sihvola. *Electromagnetics of Bi-anisotropic Materials: Theory and Applications*. Gordon and Breach Science Publishers, 2001.

[36] N. Katsarakis, T. Koschny, M. Kafesaki, E.N. Economou, and C.M. Soukoulis. Electric coupling to the magnetic resonance of split ring resonators. *Appl. Phys. Lett.*, 84(15):2943, 2004.

[37] A.V. Rogacheva, V.A. Fedotov, A.S. Schwanecke, and N.I. Zheludev. Giant gyrotropy due to electromagnetic-field coupling in a bilayered chiral structure. *Phys. Rev. Lett.*, 97(17):177401, 2006.

[38] J. Gansel, M. Thiel, M. Rill, M. Decker, K. Bade, V. Saile, G. von Freymann, S. Linden, and M. Wegener. Gold helix photonic metamaterial as broadband circular polarizer. *Science*, 325(5947):1513, 2009.

[39] J.B. Pendry. A chiral route to negative refraction. *Science*, 306(5700):1353, 2004.

[40] R. Zhao, Th. Koschny, and C.M. Soukoulis. Chiral metamaterials: retrieval of the effective parameters with and without substrate. *Opt. Express*, 18(14):14553, 2010.

[41] Q. Cheng and T.J. Cui. Negative refractions in uniaxially anisotropic chiral media. *Phys. Rev. B*, 73(11):113104, 2006.

[42] S. Zhang, Y. Park, J. Li, X. Lu, W. Zhang, and X. Zhang. Negative refractive index in chiral metamaterials. *Phys. Rev. Lett.*, 102(2):023901, 2009.

[43] M. He, J. Han, Z. Tian, J. Gu, and Q. Xing. Negative refractive index in chiral spiral metamaterials at terahertz frequencies. *Opt - Int J Light Electron Opt.*, 122(18):1676, 2011.

[44] E. Saenz, I. Semchenko, S. Khakhomov, K. Guven, R. Gonzalo, E. Ozbay, and S. Tretyakov. Modeling of spirals with equal dielectric, magnetic, and chiral susceptibilities. *Electromagnetics*, 28(7):476, 2008.

[45] J. Gansel, M. Latzel, A. Frolich, J. Kaschke, M. Thiel, and M. Wegener. Tapered gold-helix metamaterials as improved circular polarizers. *Appl. Phys. Lett.*, 100(10):101109, 2012.

[46] M. Decker, M. Ruther, C.E. Kriegler, J. Zhou, C.M. Soukoulis, S. Linden, and M. Wegener. Strong optical activity from twisted-cross photonic metamaterials. *Opt. Lett.*, 34(16):2501, 2009.

[47] M. Decker, R. Zhao, C.M. Soukoulis, S. Linden, and M. Wegener. Twisted split-ring-resonator photonic metamaterial with huge optical activity. *Opt. Lett.*, 35(10):1593, 2010.

[48] Z. Wei, Y. Cao, Y. Fan, X. Yu, and H. Li. Broadband polarization transformation via anhanced asymmetric transmission through arrays of twisted complementary split-ring resonators. *Appl. Phys. Lett.*, 99(22):221907, 2011.

[49] Y. Zhao, M.A. Belkin, and A. Alu. Twisted optical metamaterials for planarized ultrathin broadband circular polarizers. *Nat. Commun.*, 3(May):870, 2012.

[50] N. Engheta and P.G. Zablocky. A step towards determining transient response of chiral materials: Kramers-Kronig relations for chiral parameters. *Electron Lett.*, 26(25):2132, 1990.

[51] E. Hendry, R.V. Mikhaylovskiy, L.D. Barron, M. Kafesaki, M. Kadodwala, and T.J. Davis. Chiral electromagnetic fields generated by arrays of nanoslits. *Nano Lett.*, 12(7):3640, 2012.

[52] Z. Li, K.B. Alici, E. Colak, and E. Ozbay. Complementery chiral metamaterials with giant optical activity and negative refractive index. *Appl. Phys. Lett.*, 98(16):161907, 2011.

[53] A. Andryieuski, C. Menzel, C. Rockstuhl, R. Malureanu, F. Lederer, and A. Lavrinenko. Homogenization of resonant chiral metamaterials. *Phys. Rev. B*, 82(23):235107, 2010.

[54] Z. Li, H. Caglayan, E. Colak, J. Zhou, C.M. Soukoulis, and E. Ozbay. Coupling effect between two adjacent chiral structure layers. *Opt. Express*, 18(6):5375, 2010.

[55] Y. Ding, G. Zhang, and Y. Cheng. Giant optical activity and negative refractive index in the terahertz region using complementary chiral metamaterials. *Phys. Scr.*, 85(6):065405, 2012.

[56] Z. Li, K.B. Alici, H. Caglayan, M. Kafesaki, C.M. Soukoulis, and E. Ozbay. Composite chiral metamaterials with negative refractive index and high values of the figure of merit. *Opt. Express*, 20(6):6146, 2012.

[57] I.V. Shadrivov, S.K. Morrison, and Y.S. Kivshar. Tunable split-ring resonators for nonlinear negative-index metamaterials. *Opt. Express*, 14(20):9344, 2006.

[58] K.D. Singer, J.E. Sohn, and S.J. Lalama. Second harmonic generation in poled polymer films. *Appl. Phys. Lett.*, 49(5):248, 1986.

[59] J. Squier, M. Muller, G. Brakenhoff, and K.R. Wilson. Third harmonic generation microscopy. *Opt. Express*, 3(9):315, 1998.

[60] Z. Wang and Y. Luo and L. Peng and J. Huangfu and T. Jiang and D. Wang and H. Chen, and L. Ran. Second-harmonic generation and spectrum modulation by an active nonlinear metamaterial. *Appl. Phys. Lett.*, 94(13):134102.

[61] A. Rose, D. Huang, and D.R. Smith. Controlling the Second Harmonic in a Phase-Matched Negative-Index Metamaterial. *Phys. Rev. Lett.*, 107(6):063902, 2011.

[62] F. Hache D., Ricard, C. Flytzanis, and U. Kreibig. The optical kerr effect in small metal particles and metal colloids: The case of gold. *Appl. Phys. A*, 47(4):347, 1988.

[63] A. Degiron, J.J. Mock, and D.R. Smith. Modulating and tuning the response of metamaterials at the unit cell level. *Opt. Express*, 15(3):1115, 2007.

[64] I. Gil, J. Garcia-Garcia, J. Bonache, F. Martin, M. Sorolla, and R. Marques. Varactor-loaded split ring resonators for tunable notch filters at microwave frequencies. *Electron. lett.*, 40(21):1347, 2004.

[65] D.A. Powell, I.V. Shadrivov, Y.S. Kivshar, and M.V. Gorkunov. Self-tuning mechanisms of nonlinear split-ring resonators. *Appl. Phys. Lett.*, 91(14):144107, 2007.

[66] S. Larouche and D.R. Smith. A retrieval method for nonlinear metamaterials. *Opt. Comm.*, 283(8):1621, 2010.

[67] D. Huang, E. Poutrina, and D.R. Smith. Analysis of the power dependent tuning of a varactor-loaded metamaterial at microwave frequencies. *Appl. Phys. Lett.*, 96(10):104104, 2010.

[68] D. Huang, A. Rose, E. Poutrina, S. Larouche, and D.R. Smith. Wave mixing in nonlinear magnetic metacrystal. *Appl. Phys. Lett.*, 98(20):204102, 2011.

[69] M. Lapine and M. Gorkunov. Three-wave coupling of microwaves in metamaterial with nonlinear resonant conductive elements. *Phys. Rev. E*, 70(6):066601, 2004.

[70] D.A. Powell, A. Alù, B. Edwards, A. Vakil, Y.S. Kivshar, and N. Engheta. Nonlinear control of tunneling through an epsilon-near-zero channel. *Phys. Rev. B*, 79(24):245135, 2009.

[71] D.R. Smith, S. Schultz, P. Markoš, and C.M. Soukoulis. Determination of effective permittivity and permeability of metamaterials from reflection and transmission coefficients. *Phys. Rev. B*, 65(19):195104, 2002.

[72] U. Kreibig and P. Zacharias. Surface plasma resonances in small spherical silver and gold particles. *Z. Phys.*, 231(2):128, 1970.

[73] M. Gorkunov, M. Lapine, E. Shamonina, and K.H. Ringhofer. Effective magnetic properties of a composite material with circular conductive elements. *Eur. Phys. J. B*, 28(3):263, 2002.

[74] R. Marques, L. Jelinek, M.J. Freire, J.D. Baena, and M.I. Lapine. Bulk Metamaterials Made of Resonant Rings. *Proc. IEEE*, 99(10):1660, 2011.

[75] M. Lapine, D. Powell, M. Gorkunov, I. Shadrivov, R. Marques, and Y. Kivshar. Structural tunability in metamaterials. *Appl. Phys. Lett.*, 95(08):084105, 2009.

[76] D.A. Powell, M. Lapine, M.V. Gorkunov, I.V. Shadrivov, and Y.S. Kivshar. Metamaterial tuning by manipulation of near-field interaction. *Phys. Rev. B*, 82(15):155128, 2010.

[77] I.V. Shadrivov, D.A. Powell, S.K. Morrison, Y.S. Kivshar, and G.N. Milford. Scattering of electromagnetic waves in metamaterial superlattices. *Appl. Phys. Lett.*, 90(20):201919, 2007.

[78] G.R. Keiser, K. Fan, X. Zhang, and R.D. Averitt. Towards Dynamic, Tunable, and Nonlinear Metamaterials via Near Field Interactions: A Review. *J. .Infrared, Millimeter, Terahertz Waves*, 34(11):709, 2013.

[79] H. Liu, D.A. Genov, D.M. Wu, Y.M. Liu, Z.W. Liu, C. Sun, S.N. Zhu, and X. Zhang. Magnetic plasmon hybridization and optical activity at optical frequencies in metallic nanostructures. *Phys. Rev. B*, 76(7):073101, 2007.

[80] H.A. Haus and W. Huang. Coupled-mode theory. *Proc. IEEE*, 79(10):1505, 1991.

[81] R. Marques, F. Mesa, J. Martel, and F. Medina. Comparative analysis of edge- and broadside-coupled split ring resonators for metamaterial design - Theory and experiments. *IEEE Trans. Antennas Propag.*, 51(10):2572, 2003.

[82] N. Liu and H. Giessen. Coupling effects in optical metamaterials. *Angew. Chemie Int. Ed.*, 49(51):9838, 2010.

[83] Z. Li, K. Aydin, T. Li, and E. Ozbay. Determination of the effective constitutive parameters of bianisotropic metamaterials from reflection and transmission coefficients. *Phys. Rev. E*, 79(2):026610, 2009.

[84] N. Liu, H. Liu, S. Zhu, and H. Giessen. Stereometamaterials. *Nat. Photonics*, 3(19):157, 2009.

[85] H. Liu, J.X. Cao, S.N. Zhu, N. Liu, R. Ameling, and H. Giessen. Lagrange model for the chiral optical properties of stereomematerials. *Phys. Rev. B*, 81(24):241403, 2010.

[86] H. Husu, R. Siikanen, J. Mäkitalo, J. Lehtolahti, J. Laukkanen, M. Kuittinen, and M. Kauranen. Metamaterials with tailored nonlinear optical response. *Nano Lett.*, 12(2):673, 2012.

[87] Y. Zeng, C. Dineen, and J.V. Moloney. Magnetic dipole moments in single and coupled split-ring resonators. *Phys. Rev. B*, 81(7):075116, 2010.

[88] A.E. Miroshnichenko, S. Flach, and Y.S. Kivshar. Fano resonances in nanoscale structures. *Rev. Mod. Phys.*, 82(3):2257, 2010.

[89] A.B. Yakovlev and G.W.Hanson. Mode-transformation and mode-continuation regimes on waveguiding structures. *IEEE Trans. Microw. Theory .Techn.*, 48(1):67, 2000.

[90] V.P. Shestopalov. *Spectral theory and excitation of open structures*. Naukova Dumka, Kiev, 1987.

[91] V.P. Shestopalov. Morse Critical Points of Dispersion Equations of Open Resonators. *Electromagnetics*, 13(3):239, 1993.

[92] A.B. Yakovlev and G.W.Hanson. On the nature of critical points in leakage regimes of a conductor-backed coplanar strip line. *IEEE Trans. Microw. Theory Techn.*, 45(1):87, 1997.

[93] SMV1405SMV1419: Hyperabrupt Junction Tuning Varactors, 2004. www.datasheetcatalog.com.

[94] Varactor SPICE Models for RF VCO Applications, 2005. SMV APN1004 datasheet.

[95] S.A. Mousavi, E. Plum, J. Shi, and N.I. Zheludev. Coherent control of birefringence and optical activity. *Appl. Phys. Lett.*, 105(1):011906, 2014.

[96] J.D. Jackson. *Classical Electrodynamics Third Edition*. John Wiley & Sons, 1999.

[97] F. Falcone, T. Lopetegi, M.A.G. Laso, J.D. Baena, J. Bonache, M. Beruete, R. Marques, F. Martin, and M. Sorolla. Babinet principle applied to the design of metasurfaces and metamaterials. *Phys. Rev. Lett.*, 93(19):197401, 2004.

[98] A. Bitzer, A. Ortner, H. Merbold, T. Feurer, and M. Walther. Terahertz near-field microscopy of complementary planar metamaterials: Babinet's principle. *Opt. Express*, 19(3):2537, 2011.

[99] M. Navarro-Cia, M. Aznebet, M. Beruete, F. Falcone, O. El Mrabet, M. Sorolla, and M. Essaaidi. Stacked complementary metasurfaces for ultraslow microwave metametarials. *Appl. Phys. Lett.*, 96(16):164103, 2010.

[100] Y. Chiang, C. Yang, Y. Yang, C. Pan, and T. Yen. An ultrabroad terahertz bandpass filter based on multiple-resonance excitation of a composite metamaterial. *Appl. Phys. Lett.*, 99(19):191909, 2011.

[101] M. Liu, D.A. Powell, I.V. Shadrivov, and Y.S. Kivshar. Optical activity and coupling in twisted dimer meta-atoms. *Appl. Phys. Lett.*, 100(11):111114, 2012.

[102] Z. Wei, Y. Cao, Y. Fan, X. Yu, and H. Li. Broadband transparency achieved with the stacked metallic multi-layers perforated with coaxial annular apertures. *Opt. Express*, 19(22):21425, 2011.

[103] T.Q. Li, H. Liu, T. Li, S.M. Wang, J.X. Cao, Z.H. Zhu, Z.G. Dong, S.N. Zhu, and X. Zhang. Suppression of radiation loss by hybridization effect in two coupled split-ring resonators. *Phys. Rev. B*, 80(11):115113, 2009.

[104] A.V. Kildishev, J.D. Borneman, X. Ni, V.M. Shalaev, and V.P. Drachev. Bianisotropic effective parameters of optical metamagnetics and negative-index materials. *Proc. of the IEEE*, 99(10):1691, 2011.

[105] D.R. Smith, D.C. Vier, Th. Koschny, and C.M. Soukoulis. Electromagnetic parameter retrieval from inhomogenous metamaterials. *Phys. Rev. E*, 71(3):036617, 2005.

[106] D. Zarifi, M. Soleimani, and A. Abdolali. Parameter retrieval of chiral metamaterials based on the state-space approach. *Phys. Rev. E*, 88(2):023204, 2013.

[107] C. Rockstuhland T. Paul, F. Lederer, T. Pertsch, T. Zentgraf, T. Meyrath, and H. Giessen. Transition from thin-film to bulk properties of metamaterials. *Phys. Rev. B*, 77(3):035126, 2008.

[108] R. Mavaddat. *Network Scattering Parameters*. World Scientific Publishing, 1996.